BIOANALYTICAL TECHNIQUES FOR THE ANALYSIS OF MITOCHONDRIAL HETEROGENEITY

A THESIS
SUBMITTED TO THE FACULTY OF
UNIVERSITY OF MINNESOTA
BY

GREGORY GENE WOLKEN

IN PARTIAL FULFILLMENT OF THE REQUIREMENTS
FOR THE DEGREE OF
DOCTOR OF PHILOSOPHY

EDGAR A. ARRIAGA, ADVISOR

OCTOBER 2013

Acknowledgements

Thank you to all the Arriaga group members I had the privilege of working with. I couldn't ask for a better group of people to share this experience with.

Thank you to everyone who taught me or challenged me along my way. My experience at the University of Minnesota was always interesting and thought-provoking.

Thank you to Edgar for his guidance, dedication, and never ending positivity.

Thank you to my wife Cheryl, who always gave me her loving support.

Thank you to my mom and dad, for teaching me most of what I know.

Dedication

This thesis is dedicated to my daughter, Norah Sophia Wolken.

Abstract

In this thesis, techniques are described for the measurement of individual mitochondrial isoelectric point (p*I*) using capillary isoelectric focusing (cIEF) with laser-induced fluorescence detection, simulation of the contribution of mitochondrial surface compositions to p*I*, and determination of individual mitochondrial membrane potential and electrophoretic mobility using capillary electrophoresis with laser-induced fluorescence detection (CE-LIF). These techniques provide insight into mitochondrial heterogeneity, which could increase fundamental understanding of the role played by mitochondria in aging.

A method was developed to determine the p*I*s of individual mitochondria by cIEF. This method provides reproducible distributions and accurate determination of individual mitochondrial p*I* by the use of internal standards, and was able to detect changes in mitochondrial p*I* distributions caused by changes to the mitochondrial surface by treatment with trypsin. Application of this method demonstrated the heterogeneity of mitochondrial p*I*, which reflects the heterogeneity of mitochondrial surface compositions.

To model the effect of surface composition on mitochondrial p*I* heterogeneity, a method was developed to predict mitochondrial p*I* values using simulated surface compositions consisting of different percentages of amino acids and phospholipids found in the mitochondrial outer membrane. This method was validated by predicting the p*I* values of known mitochondrial outer membrane proteins then extended to isolated mitochondria and used to model a p*I* distribution determined experimentally by cIEF. Significant changes in the percentages of some amino acids and phospholipids were

predicted for observed p*I* differences between individual mitochondria. This model provides insight into the heterogeneity of mitochondrial p*I* and contribution of surface compositions.

Distributions of individual mitochondrial membrane potential and electrophoretic mobility were measured using CE-LIF. Mitochondria from cultured cells and mouse muscle and liver tissue were labeled with JC-1, a ratiometric dye which indicates membrane potential. Analysis of specific regions of interest defined by performing CE-LIF of depolarized samples makes this method capable of analyzing mitochondrial membrane potential even in preparations where depolarized mitochondria may be present due to biological variation or experimental factors that result in damage to mitochondria or may be insufficient to keep all mitochondria polarized. This analysis revealed additional differences between samples and an effect of membrane potential on electrophoretic mobility. This method allows for the characterization of mitochondrial heterogeneity in membrane potential and surface properties.

In the future, these methods can be applied to biological models of aging to elucidate the role that mitochondrial heterogeneity plays in age-related dysfunction and disease.

Table of Contents

List of Tables

List of Figures

Chapter 2

Chapter 3

Chapter 4

Chapter 5

Chapter 7

Appendix A

Appendix B

Appendix C

List of Abbreviations

5-TAMRA	5-carboxytetramethylrhodamine
ATG7	autophagy-related gene/protein 7
ATP	adenosine triphosphate
BCA	bicinchoninic acid
CCCP	carbonyl cyanide 3-chlorophenylhydrazone
CE	capillary electrophoresis
cIEF	capillary isoelectric focusing
DMEM	Dulbecco's modified Eagle medium
DMSO	dimethyl sulfoxide
EOF	electroosmotic flow
FBS	fetal bovine serum
FCCP	carbonyl cyanide 4-(trifluoromethoxy)phenylhydrazone
FFE	free-flow electrophoresis
FFF	field-flow fractionation
FFIEF	free-flow isoelectric focusing
HEPES	4-(2-hydroxyethyl)piperazine-1-ethanesulfonic acid
HPC	hydroxypropyl cellulose
JC-1	5,5′,6,6′-Tetrachloro-1,1′,3,3′-tetraethyl-imidacarbocyanine iodide
KOH	potassium hydroxide
LED	light-emitting diode
LIF	laser induced fluorescence
MFN1,MFN2	mitofusin 1, mitofusin2
MOPS	3-(N-morpholino)propanesulfonic acid
PBS	phosphate-buffered saline
p*I*	isoelectric point
PINK1	PTEN-induced putative kinase 1
PVA	polyvinyl alcohol
ROI	region of interest
ROS	reactive oxygen species
siRNA	silencing RNA
TEM	transmission electron microscopy
TPP^+	triphenylphosphonium

Chapter 1.

Introduction

The World Health Organization reports that the global population of aging individuals is increasing dramatically: worldwide, the number of people 65 years of age and older is projected to increase from 524 million in 2010 to 1.5 billion in 2050.[1] This is an increase not only in number but also in percentage, from 8% in 2010 to 16% of the world's projected population in 2050. Clearly, the study of aging and age-related diseases such as cancer, diabetes, Alzheimer's, and heart disease is vital to ensuring the health and prosperity of our aging population.

Mitochondria, the energy-producing organelles of eukaryotic cells, represent a widely studied topic in the field of aging research. A central theory of aging states that damage to cellular components by reactive oxygen species (ROS) produced as a by-product of mitochondrial respiration accumulates with age, and that this cellular damage is the origin of the physiological changes in aging.[2,3] Although there is debate about whether ROS production by mitochondria is actually the cause of aging,[4] it is clear that mitochondria and the quality control mechanisms responsible for maintaining their normal function play a pivotal role in aging and age-related diseases.[5-7] Further study of mitochondria is necessary to increase our understanding of this role, which could ultimately lead to treatments for age-related disorders and diseases.

A major challenge in the characterization of mitochondria in any biological system is the highly heterogeneous nature of these organelles. Mitochondrial properties that are heterogeneous include morphology (size and shape), energy production (oxidative phosphorylation), ROS generation, membrane potential, phospholipid

composition, and protein expression.[8] This heterogeneity reflects differences in function of mitochondria depending on energy demand (e.g. morphological changes[9]) or subcellular locations (e.g. intermyofibrillar vs. subsarcolemmal mitochondria[10]), and could also reflect the presence of damaged or dysfunctional subpopulations of mitochondria.[11]

In aging, one potential source of heterogeneity is mitochondrial regulation and turnover. Mitochondrial function is regulated by the fusion/fission process and dysfunctional mitochondria are eliminated through turnover by mitophagy.[12] As organisms age, mitochondrial removal by mitophagy becomes less effective and mitochondrial dysfunction increases.[13] In aging tissue, giant mitochondria have been observed,[14-16] which may represent a heterogeneous dysfunctional subpopulation that contributes to cellular damage in aging.[17,18] A manifestation of heterogeneity in giant mitochondria is their reduced mitochondrial membrane potential. Mitochondrial membrane potential is highly heterogeneous, depending on subcellular location,[19,20] functional status and morphology,[18,20,21] and damage to mitochondria,[22] and plays an important role in mitochondrial maintenance by the fusion/fission process[23] and turnover by mitophagy.

Targeting of mitochondria for elimination by mitophagy results in modifications to the surface of mitochondria and may represent another source of mitochondrial heterogeneity in surface properties. Upon loss of membrane potential, the protein PINK1 accumulates on the surface of mitochondria and recruits Parkin, which modifies

mitochondrial proteins by ubiquitination.[24] This results in extraction and degradation of some mitochondrial proteins (e.g. MFN1 and MFN2), although this is not required for mitophagy and the complete mechanism for mitophagy targeting is not understood.[25]

Better methods for the characterization of individual mitochondrial membrane potential, mitochondrial surface properties, and separations of mitochondrial subpopulations would allow for further elucidation of the role of mitochondrial heterogeneity in the aging process. This thesis describes the development of new analytical techniques for the separation and analysis of individual mitochondria, which are applicable to the characterization of mitochondrial heterogeneity.

Chapter 2 covers background related to mitochondrial analysis and introduces the techniques used in this work. One mitochondrial surface property that is heterogeneous is isoelectric point (p*I*), which reflects differences in the protein and phospholipid composition of the mitochondrial outer membrane.

Chapter 3 describes development of a method for determination of individual mitochondrial p*I*s by capillary isoelectric focusing (cIEF). This method was used to demonstrate that mitochondria from cultured cells exhibit distributions of p*I*, which were calculated accurately by the inclusion of p*I* markers as internal standards. The method could detect changes in the mitochondrial p*I* distribution upon modification of the mitochondrial surface with trypsin, suggesting that other mitochondrial surface modifications relevant to mitochondrial heterogeneity and aging could be detected using this technique.

Chapter 4 describes predictions of mitochondrial p*I* by simulations of surface compositions. This method describes the contribution of amino acids and phospholipids in the mitochondrial outer membrane to the p*I* heterogeneity observed in cIEF. This method can be used to make predictions about changes to mitochondrial p*I* which might result from modifications to the mitochondrial surface relevant to mitochondrial targeting for mitophagy.

Chapter 5 describes a method to measure individual mitochondrial membrane potential by capillary electrophoresis with laser induced fluorescence detection (CE-LIF). This method was used to determine distributions of mitochondrial membrane potential and electrophoretic mobility, and is applicable to mitochondria isolated from cultured cells and mouse muscle and liver tissue even in samples where depolarized mitochondria are present. The ability to determine individual mitochondrial isoelectric points and electrophoretic mobility is an important tool in characterization of mitochondrial heterogeneity.

Chapter 6 summarizes the conclusions and significance of this work: in short, we have developed tools to characterize mitochondrial heterogeneity including a method to measure distributions of mitochondrial p*I*, a model that describes the contribution of the outer membrane composition to p*I*, and a method to measure distributions of individual mitochondrial membrane potential and electrophoretic mobility. These tools could be valuable in understanding mitochondrial heterogeneity in aging.

Chapter 7 describes possible future improvements to the cIEF method described in Chapter 3 to improve its analytical capabilities of accurately measuring the p*I*s of individual organelles. The model of mitochondrial p*I* from Chapter 4 could be used to predict changes in mitochondrial p*I* arising from modifications to the mitochondrial surface involved in targeting for mitophagy or from changes in membrane potential; these applications are discussed in Chapter 7. This chapter also describes future experiments to develop a new method for individual mitochondrial isolation by cytoskeletal disruption and electroporation, which is needed for characterization of giant mitochondria in aging models using the methods described in Chapters 3 and 5.

Overall, the work described in this thesis represents a contribution of new methods to study mitochondrial heterogeneity, which could increase our fundamental understanding of these organelles. Elucidation of the role of mitochondrial dysfunction and heterogeneity in aging could eventually lead to new treatments for age-related disorders and disease.

Chapter 2.

Background

2.1. Mitochondrial Properties and Heterogeneity in Aging

Mitochondria are double membrane-bound organelles involved in energy production, metabolism, and many important cellular processes such as apoptosis.[26] See Figure 2-1 for a basic description of mitochondrial structure. Mitochondria are heterogeneous, with variations in properties among different tissue types, subcellular locations, functional statuses, and diseases.[8] These properties include morphology (size and shape), energy production (oxidative phosphorylation), reactive oxygen species (ROS) generation, membrane potential, phospholipid composition, and protein expression. Differences in these properties affect their maintenance and regulation in the cell by the fusion/fission process[12] and turnover by mitophagy, the mitochondrial-specific form of autophagy.[11,12] These processes work together to eliminate damaged mitochondria and regulate cellular energy production.[9,27]

Mitochondrial dysfunction and disruption in their normal regulation and turnover in the cell is a major factor in aging.[7] Mitochondria in aging tissue are less efficient at producing ATP.[28] As cells age, increased damage from ROS accumulates and some dysfunctional mitochondria are excluded from the fusion and fission process, in which mitochondria fuse and divide to regulate their function and distribute damage. Moreover, mitophagy, the process responsible for elimination of dysfunctional mitochondria, becomes less effective at removing them from the cell.[13] One mitochondrial property that becomes more heterogeneous with age is size; so-called giant mitochondria are thought to represent a dysfunctional subpopulation that is not effectively eliminated from the cell.

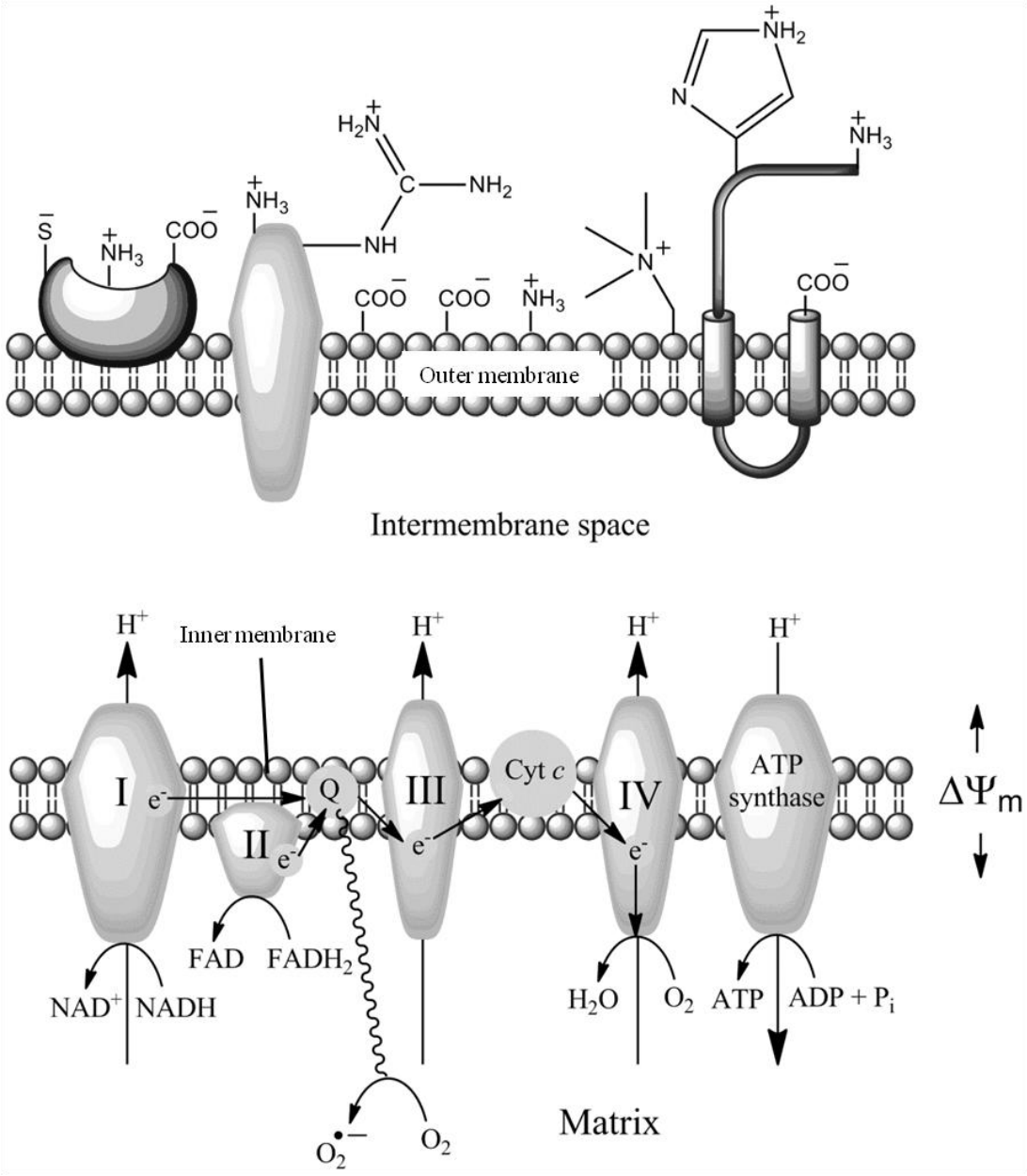

Figure 2-1. Mitochondrial structure. Mitochondria generate ATP via oxidative phosphorylation. This process is driven by the mitochondrial membrane potential ($\Delta\Psi_m$) established across the inner mitochondrial membrane by the enzymes of the electron transport chain, which pump protons from the matrix to the intermembrane space. Free radical intermediates of coenzyme Q reduce oxygen to superoxide, a major form of ROS in the cell. The mitochondrial outer membrane contains proteins and phospholipids which give rise to its electrophoretic properties. Figure adapted from Brownlee.[29]

Enlarged mitochondria have been observed in aging tissue[14-16,30] and senescent cells.[17] In a cell model of aging with impaired autophagy, heterogeneity in mitochondrial size including giant mitochondria over 1 μm in diameter, decreases in membrane potential, and expression of proteins involved in fusion and fission was observed.[18] Targeting for elimination of these organelles by mitophagy may be compromised. In this process, loss of mitochondrial membrane potential causes accumulation of the protein PINK1 on the surface of mitochondria. This protein recruits Parkin, which ubiquitinates mitochondrial proteins.[24,31] This modification causes some proteins to be extracted and degraded,[32] and targets mitochondria to autophagosomes for degradation by mitophagy.[25] These modifications to the mitochondrial surface are manifestations of mitochondrial heterogeneity which is expected to increase in aging. The methods described in Chapters 3 and 5 of this work could be used to characterize these changes in mitochondrial surface properties, which may lead to separations of subpopulations of mitochondria which are important in the aging process.

Mitochondrial membrane potential is involved in energy production, signaling of mitochondrial regulation by the fusion/fission process, and turnover by mitophagy,[23,33-35] and apoptosis.[36] Mitochondrial membrane potential is an electrochemical gradient used to drive ATP production. It is established by transport of protons across the mitochondrial inner membrane by the enzymes of the electron transport chain (see Figure 2-1 above), which creates a pH gradient and an electrical potential. Mitochondria are considered polarized when this potential difference is present; depolarization occurs when the

potential is dissipated. While some ROS is normally produced in mitochondrial respiration, increases in membrane potential result in increased levels of ROS which cause damage to the cell and are a factor in many mitochondrial related diseases including cancer, diabetes, and Alzheimer's.[37] Mitochondrial membrane potential is heterogeneous, depending on energy demand, subcellular location, morphology, and functional status. Membrane potential is influenced by changes in local calcium concentration, and may be controlled by cellular mechanisms to limit production of ROS in certain regions (e.g. near the nucleus).[19] Chapter 5 of this work describes a method to measure distributions of individual mitochondrial membrane potential, which may become an important tool for characterization of mitochondrial heterogeneity in aging.

Mitochondrial morphology is another property that becomes more heterogeneous with age. Depending on cellular energy demand or damage to mitochondria, they may be in a fragmented, spherical morphology, more tubular, or part of a reticulated network of interconnected organelles.[38] Morphology is regulated by the fusion/fission process and by mitochondrial attachments to the cytoskeletal network in the cell.[39] This interaction helps regulate mitochondrial function and provides a mechanism for movement of mitochondria around the cell. When mitochondria are isolated from the cell for analysis, they retain cytoskeleton on their surface which has an effect on their electrophoretic properties.[40] This represents an issue for analysis of mitochondrial surface properties by the methods described in Chapters 3 and 5. The future work described in Chapter 7

discusses a method for the isolation of mitochondria from the cell by disruption of cytoskeleton which could improve analysis of their surface properties.

Although much is understood about mitochondrial properties and their role in aging and disease, new methods are needed to further unravel the complexity of mitochondrial heterogeneity. The connections between mitochondrial size, turnover, and dysfunction are not fully understood, and techniques to study these properties will advance understanding of their role in aging and disease. The methods described in this work could be applied to help elucidate the role of mitochondrial heterogeneity in aging.

2.2. Techniques for Mitochondrial Analysis

2.2.1. Imaging

Characterization of heterogeneity in mitochondrial morphology that may be important in aging can be accomplished using imaging techniques. Fluorescence microscopy is widely used to observe mitochondrial morphology and measure their properties. Depending on the choice of labeling strategy, specific proteins, DNA, properties such as membrane potential, specific ROS, redox state, or dynamic processes such as fusion and fission may be observed.[41] This technique is versatile; it enables the observation of mitochondria in fixed or living cells or isolated and adsorbed to slides.[42] A recent publication described monitoring the NADH levels in individual mitochondria arrayed in a device containing nanoscale wells.[43] Mitochondria may be labeled with small-molecule probes which are sequestered in the mitochondria. These probes may be taken up in response to mitochondrial membrane potential (JC-1), may be fixable

(MitoTracker probes[44]), may label a mitochondrial-specific phospholipid, cardiolipin (10-N nonyl-acridine orange[45]), or may be designed to respond to levels of reactive oxygen species (e.g. MitoSOX Red[46]). Immunolabeling is a widely used strategy for specifically labeling mitochondrial proteins. Cells grown in culture can be transfected to produce stable fluorescent proteins which can be targeted to mitochondria.[47] See the recent review by Satori et al. for an extensive list of mitochondrial probes.[48]

New advances in super-resolution fluorescence microscopy promise to reveal new detail in mitochondrial heterogeneity.[49] This family of techniques uses specialized optics for excitation or novel photoswitchable fluorophores that overcome the diffraction limit of ~250 nm and allow for visualization of features with resolution in the 20 – 50 nm range. One limitation of imaging as a tool to characterize mitochondrial heterogeneity is its throughput – characterizing large numbers of mitochondria is labor intensive. In this work, imaging is used as a complementary technique to the method developed in Chapter 5, and will be important to observe the mitochondria isolated from cells by the new method proposed as future work in Chapter 7.

2.2.2. Membrane Potential

Mitochondrial membrane potential may be measured quantitatively by using a triphenylphosphonium (TPP^+) ion-selective electrode.[50] In this technique, uptake of TPP^+ into the mitochondrial matrix from a solution with known concentration is measured with the electrode. Distribution of this cation into the matrix is described by the Nernst equation, and mitochondrial membrane potential may be calculated directly if the

mitochondrial matrix volume is known (this is estimated by measuring the total protein content of the isolated mitochondria). A disadvantage of this technique is that it requires a relatively large amount of mitochondria (~0.5 mg), which can prevent its use with samples which are cost-prohibitive to prepare in large amounts (for example, mitochondria from cell culture in which expensive reagents are used for transfections). Recent advances in integrating a TPP^+ microelectrode into microfluidic device provide improvements to the sensitivity of this technique and make it amenable to smaller amounts of sample.[51,52]

Measurement of mitochondrial membrane potential in imaging, bulk fluorescence techniques, and flow cytometry may be accomplished by the use of fluorescent probes.[53] These probes are cationic, which drives uptake into the mitochondrial matrix in a membrane potential dependent manner according to the Nernst equation.[54] Quantitation of membrane potential using probes such as rhodamine 123 or tetramethylrosamine involves measuring their fluorescence intensity inside mitochondria and comparing to the fluorescence intensity of a depolarized control sample. Protonophores such as carbonyl cyanide 3-chlorophenylhydrazone (CCCP) or carbonyl cyanide 4-(trifluoromethoxy)phenylhydrazone (FCCP) or ionophores such as valinomycin are used to depolarize mitochondria, as they facilitate free transport of ions across the mitochondrial inner membrane (see Figure 2-1), which dissipates the membrane potential. The disadvantage of using probes such as rhodamine 123 or tetramethylrosamine is that their observed fluorescence intensity is influenced by

mitochondrial size as well as membrane potential, so membrane potential is overestimated in larger mitochondria.[55] While this is not an issue in microscopy because the fluorescence intensity can be normalized by the size of the organelle, this would be an issue in a technique where size is not measured, such as capillary electrophoresis (as in the method described in Chapter 5 of this work). To prevent this issue, a ratiometric dye can be used.

2.2.3. JC-1

Ratiometric dyes undergo a spectral shift or transformation upon their uptake into mitochondria which can be measured and used to normalize their response across different dye concentrations or mitochondrial sizes.[55] One such dye is JC-1, which is commonly used to measure mitochondrial membrane potential.[53,56] At low concentrations (less than approximately 100 nM), JC-1 exists as a monomer and exhibits green fluorescence (the broad peak centered at 540 nm in the spectrum shown in Figure 2-2). [38] At higher concentrations, this dye forms J-aggregates which causes a red-shift of the fluorescence emission (narrow peak centered at 590 nm). Since JC-1 is cationic (structure shown below in Figure 2-2**),** mitochondrial membrane potential drives its uptake into the matrix. Polarized mitochondria with higher (more negative) membrane potential will accumulate JC-1 at a higher concentration than depolarized mitochondria. If a proper labeling concentration is chosen (i.e. low enough that minimal aggregation occurs outside mitochondria), polarized mitochondria will exhibit more red fluorescence from the JC-1 aggregates as well as green fluorescence from the monomer form of the dye, whereas

depolarized mitochondria will exhibit primarily green fluorescence. Measurement of red/green fluorescence is then used as an indicator of membrane potential. JC-1 is widely used as an indicator of mitochondrial membrane potential in fluorescence microscopy[19,41] and flow cytometry.[57,58] Applications have also been reported demonstrating its use in a microfluidic free-flow isoelectric focusing separation of isolated mitochondria[59] and in a device for immobilization of individual mitochondria in nanochannels.[42] In Chapter 5, a method is described for characterization of individual mitochondrial membrane potential using JC-1 as a probe in capillary electrophoresis with laser-induced fluorescence detection (CE-LIF).

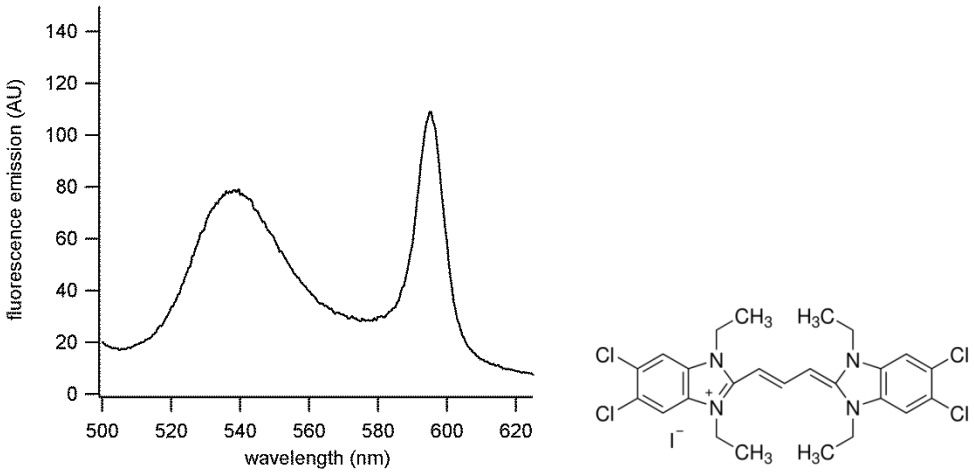

Figure 2-2. Fluorescence emission spectrum and structure of JC-1. Fluorescence from monomer (broad peak at ~540 nm) and J-aggregate (narrow peak at 590 nm) forms of the dye. Excitation: 488 nm. This dye is used as an indicator of mitochondrial membrane potential in the method described in Chapter 5 of this work.

2.3. Analytical Separations of Biological Particles

2.3.1. Methods for Mitochondrial Isolation

Analysis of mitochondria by analytical techniques usually includes some method for isolation of the mitochondria from cells or tissue. Mitochondria are typically isolated by mechanical homogenization and differential centrifugation.[60] In this technique, shearing forces that tear apart the cell membrane are created by driving a tight-fitting pestle up and down through a suspension of cells or tissue pieces in a glass cylinder. The pestle may be rotated by a motor during this process, and is typically driven up and down by hand. Differential centrifugation is then used to prepare a fraction enriched in mitochondria and other organelles of similar size and density: nuclei and intact cells are first pelleted at low speeds (e.g. 600 *g*), then mitochondria in the supernatant are pelleted at higher speeds (e.g. 10000 *g*). The supernatant, containing soluble proteins, smaller organelles, and fragments of organelles, is removed and mitochondria are resuspended in a buffer. Nitrogen cavitation (combined with centrifugation) is another technique capable of producing fractions of isolated mitochondria. This technique relies on pressurization of cells to around 1500 PSI, followed by rapid decompression, to create bubbles which disrupt the cell membrane.[61] While these techniques are capable of producing isolated fractions of mitochondria suitable for analysis, the choice of technique and how it is applied (e.g. the number or force of strokes in mechanical homogenization or the number of rounds of cavitation) has an effect on the electrophoretic properties of the mitochondria.[62] Additionally, mechanical homogenization disrupts mitochondrial

structure and has an effect on mitochondrial function; this technique caused changes in respiration, hydrogen peroxide generation, and the sensitivity of the permeability pore transition to calcium (a measure of apoptosis) when compared to mitochondria which were studied in permeabilized muscle fibers (i.e. not subjected to an isolation technique).[63,64] Since these conventional techniques may damage delicate subpopulations of mitochondria or change their electrophoretic properties, alternative methods for mitochondrial isolation are needed for better characterization of mitochondrial heterogeneity. Future experiments to develop an alternative method for mitochondrial isolation are discussed in Chapter 7 of this thesis.

2.3.2. Continuous and Flow-based Techniques

To evaluate mitochondrial heterogeneity in samples of isolated mitochondria, it is necessary to characterize a large number of organelles, which is not a strength of imaging techniques. Techniques including flow cytometry, field-flow fractionation, and free-flow electrophoresis are based on continuous flow of the particles in suspension through the instrument, which makes these methods capable of measuring large numbers of organelles. Flow cytometry is not a separation technique, but allows for the fast and high-throughput analysis of cells or organelles. A sheath-flow cuvette-based fluorescence detector is used to achieve high sensitivity, and scattering data is often collected for information on particle size or internal complexity[65]. Flow cytometry has been used to characterize mitochondrial subpopulations with differences in mitochondrial membrane potential, resistance to depolarization by FCCP, cardiolipin levels, and response to

calcium-induced swelling.[66] Fluorescence-activated cell sorting (FACS) instruments are capable of sorting biological particles, commonly used for sorting cells which express a desired fluorescent protein.[67] This technique is applicable to organelles using commercially available instruments. A recent report detailed a new device for sorting organelle subpopulations that achieved single-molecule sensitivity and demonstrated sorting of synaptic vesicles isolated from rat brains.[68]

Field-flow fractionation (FFF) is a specialized family of techniques for separation of particles. This technique separates analytes based on differences in their size and density[69] and has been used to fractionate different sizes of mitochondria[70,71] and to sort populations of whole cells.[72] In FFF, a buffer stream flows through a separation chamber. A field is applied perpendicular to the flow of buffer which deflects analytes into different lamina of the buffer stream, which possess different flow rates through the separation chamber. The separation is not achieved by the type of field applied or the interactions of analytes with that field, but rather by the distribution of analytes into the flow lamina of the buffer stream and their migration time through the separation chamber. The applied field may therefore be any type of field that causes deflection of the analytes: a thermal gradient, an electric field, or a crossflow of buffer.

Free-flow electrophoresis (FFE) is a method in which buffer flows continuously in a thin stream between two plates and an electric field is applied to the separation chamber perpendicular to buffer flow.[73] Analytes are introduced into the separation chamber and deflected in the electric field according to their electrophoretic mobility. An

advantage of FFE is that fractions containing separated components can be continuously collected. Free-flow isoelectric focusing (FFIEF) is a mode of free-flow electrophoresis. In FFIEF, a pH gradient is established across the separation chamber and analytes are deflected in the electric field, focus at their p*I*, and can be collected in separate fractions at the end of the separation chamber.[74] FFE techniques have been used to analyze mitochondria. For example, two populations of intact yeast mitochondria exhibiting different surface and structural characteristics were separated by FFE.[75] This technique has also been used to separate intact mitochondria from mitochondrial inner membrane fragments.[76] This technique has been adapted to the microfluidic format, which improves sensitivity, speed, and decreases consumption of reagents.[77] Micro-FFE has been used to analyze isolated mitochondria in both FFE mode[78] and FFIEF mode.[59] In the future, the methods described in this work could be used as a basis for designing preparative separations of subpopulations of organelles using FFE or FFIEF.

2.3.3. Capillary Electrophoresis and Capillary Isoelectric Focusing

Capillary electrophoresis (CE) is a separation technique in which analytes migrate through a fused-silica capillary in the presence of an electric field. Analytes are separated based on differences in their electrophoretic mobility, a property which depends on their surface charge density. In organelles, electrophoretic mobility depends on the deformability and relaxation of the organelle in the electric field, a capacitive effect on the phospholipid bilayer of the membrane, a redistribution of charged lipid molecules by the imposed electric field, multipole moments, and the ion polarization effect.[79-82]

Advantages of this technique include fast analysis times, minimal sample consumption, and high resolution. Capillary isoelectric focusing (cIEF) is a related technique in which analytes are separated based on their isoelectric point (p*I*). In cIEF, a pH gradient is established inside the capillary.[83] Analytes acquire charge based on the identity of their acidic and basic functional groups and migrate in the applied electric field. As they move through the pH gradient, their acidic or basic functional groups are protonated or deprotonated. They eventually migrate to the point in the pH gradient at which their net charge is zero and the pH is equal to their p*I*. Advantages of cIEF include the ability to achieve high resolution and fast analysis times using minimal amounts of sample compared to other isoelectric focusing methods. CE and cIEF have been used to analyze cells, viruses, and organelles.[84,85] These techniques are capable of achieving high-resolution separations of these analytes based on their surface properties.

Many methods for characterization of mitochondrial heterogeneity by CE have been reported. Mitochondrial electrophoretic mobility distributions have been measured by CE.[86] The existence of distributions demonstrates the heterogeneity of the surfaces of these organelles. The cardiolipin content of individual mitochondria has been determined by labeling with 10-N nonyl-acridine orange.[87] Mitochondria have been isolated from single cells and separated using CE.[88] These organelles can be sampled directly from tissue cross sections and analyzed using this technique.[89] Their DNA content has been quantified.[90] Binding of individual mitochondria to cytoskeleton has been quantified.[40] The contents of a single mitochondrion have been analyzed by microchip-CE.[91] New

applications for measuring mitochondrial p*I* by cIEF and membrane potential by CE are discussed in Chapters 3 and 5 of this work. The method described in Chapter 3 is capable of reproducibly measuring distributions of individual mitochondrial p*I* and detecting changes to the mitochondrial surface. The method described in Chapter 5 reproducibly measured distributions of individual mitochondrial membrane potential and electrophoretic mobility.

2.4. Analytical Aspects of CE and cIEF

2.4.1. Instrumentation

Basic instrumentation for performing CE consists of a fused-silica capillary, high voltage power supply, and detector. Capillaries used are typically 30 to 50 cm in length with inner diameters on the order of tens of micrometers, but extremely short or long capillaries have been used for specialized applications, ranging from a few centimeters[92] to 10 meters.[93] Analysis times are typically around 5 to 15 minutes, although separations lasting tens of microseconds[94] to tens of hours[95] have been reported. The narrow inner diameter of capillaries allows for efficient heat dissipation, which prevents zone broadening from Joule heating caused by the high electric field strengths used (typically hundreds of volts per centimeter).

Although injections can be performed electrokinetically with no additional instrumentation, most capillary electrophoresis instruments have some mechanism for performing hydrodynamic injections, either by application of pressure or vacuum to the capillary inlet or outlet (see Figure 2-3 below for a schematic of the instrument used in

this work). This injection method does not discriminate based on the electrophoretic mobility of the analyte, a problem suffered by electrokinetic injection which uses electroosmotic flow (EOF) to introduce sample to the capillary. Commercial CE instruments typically offer automation and the ability to perform fraction collection. Multi-capillary instruments can increase sample throughput by running multiple separations in parallel.[96] If higher throughput is desired in future applications (e.g. for analysis of larger sample sizes to examine differences between two biological groups), the methods described in Chapters 3 and 5 could be adapted to a multi-capillary format.

Many detection methods have been adapted to CE instruments. Detection may be performed on-column or post-column, depending on the technique. A specialized mode of on-column detection is whole-column imaging, which allows for the separation to be monitored as it progresses.[97] UV/visible absorbance detectors are commonly used because they do not require sample derivatization, but their sensitivity is limited. Electrochemical detectors excel in some applications (e.g. amperometric detectors are highly selective and sensitive if analytes are electroactive, conductivity detectors are universal but have limited sensitivity).[98] Fluorescence detectors offer excellent sensitivity; yoctomole detection levels have been achieved with laser-induced fluorescence systems utilizing a sheath-flow cuvette.[99] However, the tradeoff is that fluorescence detection requires samples to be labeled, which increases sample preparation time. Mass spectrometry as a detection method for CE offers the advantage of analyte identification and has recently been applied to analytes ranging from small

molecules to whole cells.[100] For detection of organelles, fluorescence detection is used due to its excellent sensitivity and the wide availability of organelle-specific probes (see the recent review by Satori et al. for an extensive list).[48]

A lab-built CE instrument (shown schematically in Figure 2-3 below) was used for the experiments described in Chapters 3 and 5. This instrument has been described previously and features dual channel laser-induced fluorescence detection.[101] For the cIEF experiments described in Chapter 3, the instrument was adapted to perform isoelectric focusing with on-column detection. A sample carousel used to switch between catholyte and chemical mobilization solutions for cIEF was added beneath the sheath-flow cuvette (not shown). The capillary was extended down through the sheath flow cuvette into an outlet vial held by the sample carousel, and an electrode was added that also extended down into the vial. Post-column detection with a sheath-flow cuvette was used for the CE experiments described in Chapter 5, and an additional laser (HeNe, 543.5 nm) was added for dual-laser excitation and dual-channel fluorescence detection of JC-1.

2.4.2. Capillary Coatings

Capillary coatings are commonly used in CE and cIEF to prevent analyte interactions with the capillary surface or to suppress or change the direction of EOF. Capillary coatings are particularly important in cIEF because suppression of EOF is required to maintain a stable pH gradient. Coatings which are covalently bonded to the fused silica surface can be used, which are advantageous because they are stable over many runs.

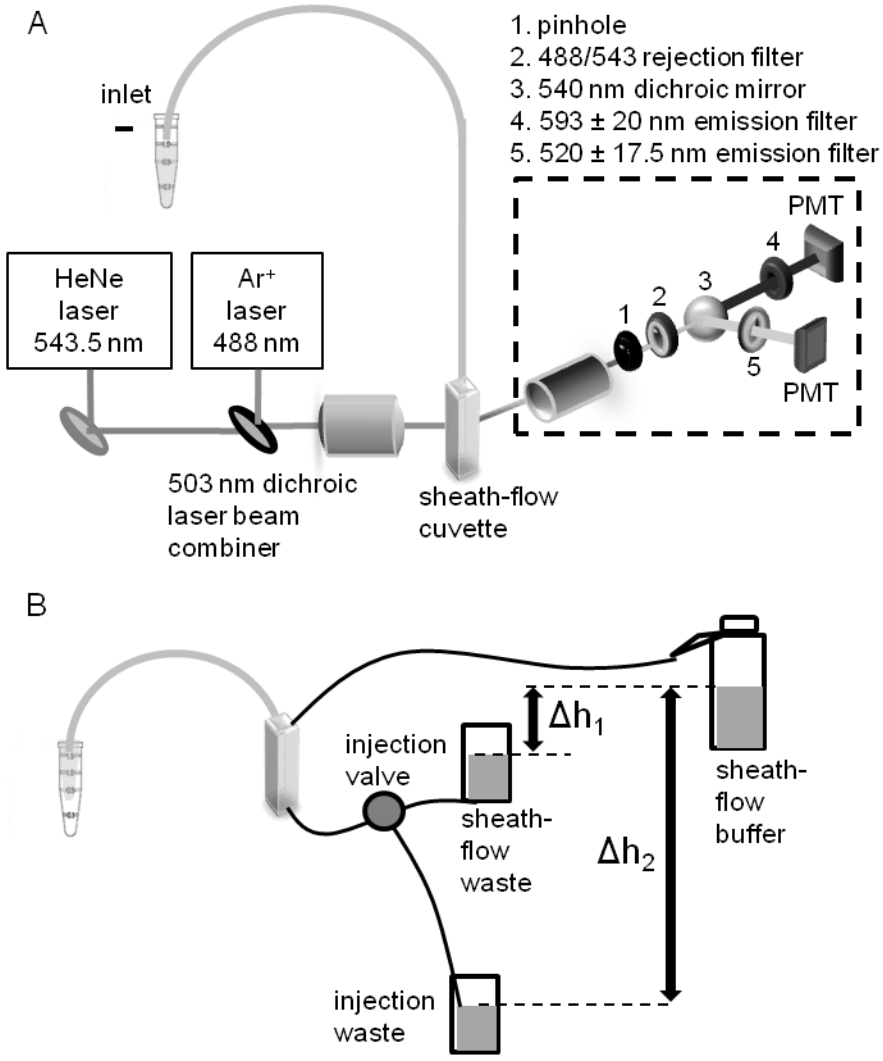

Figure 2-3. Lab-built instrument for CE-LIF and cIEF. (A) Instrument setup used in the method described in Chapter 5. This instrument features dual-laser excitation (HeNe, 543.5 and Ar^+, 488 nm), dual-channel fluorescence detection using photomultiplier tubes (PMT), and post-column detection using a sheath-flow cuvette. (B) Detail of sheath-flow system. During separation, buffer flows through the cuvette due to a small height difference between the sheath-flow buffer reservoir and the sheath-flow waste ($\Delta h_1 \approx 5$ cm). For hydrodynamic injections, a larger height difference ($\Delta h_2 = 110$ cm) is created by opening the electronically-controlled injection valve. See Chapters 3 and 5 for a complete description of this instrument.

One such coating that has been used in mitochondrial CE separations is the polymer poly(acryloylaminopropanol), which is applied by attaching a bi-functional reagent to the surface of the capillary via a Grignard reaction.[102] However, covalent coatings can be time consuming and difficult to apply, and may not stand up to harsh rinses required to remove buildup of biological materials over time. An alternative to covalent coatings are dynamic coatings, in which a buffer additive is used to coat the capillary surface.[103] This additive may be a cationic molecule which associates with the capillary surface through electrostatic interactions, a neutral polymer which adsorbs to the surface through van der Waals interactions, or a surfactant which forms monolayers on the surface. A dynamic poly(vinyl alcohol) (PVA) coating has been successfully used to reduce sample adsorption in mitochondrial CE separations.[104] Some disadvantages of dynamic coatings are that the capillary must be equilibrated with the buffer containing the additive before use and after rinsing steps, and that the solution viscosity is increased, which changes the apparent electrophoretic mobility of analytes. A middle ground between covalent coatings and dynamic coatings are permanently adsorbed non-covalent coatings, which are applied by "baking" a neutral hydrophilic polymer to the capillary surface.[105] Application of these coatings is straightforward and no buffer additive is needed. The CE experiments described in Chapter 5 utilized a permanently adsorbed PVA coating. The cIEF experiments described in Chapter 3 in this work were performed using a permanently adsorbed hydroxypropyl cellulose (HPC) coating, which was more effective at reducing the EOF than the PVA coating.

2.4.3. Buffers and Focusing Solutions

Selection of the separation buffer is important in CE, and the appropriate buffer depends on the separation mode and analyte. Several buffer characteristics are considered for performing mitochondrial CE. The buffer must be at physiological pH (7.4) to prevent the organelles from being degraded under basic or acidic conditions and the solution must be osmotically balanced (e.g. around 300 mosM) to prevent swelling or shrinking of the organelles. Salts (e.g. sodium chloride) are typically used to adjust osmolarity in buffers for cells organelles, but the high ionic strength makes them incompatible with CE, which requires a non-ionic additive to the buffer. In the CE experiments described in Chapter 5 in this work, sucrose is used to adjust the osmolarity of the solution and a HEPES buffer is used to control the pH.

Different solutions are required to perform cIEF. Before focusing, the capillary is filled with a solution containing the analytes and a mixture of zwitterionic compounds (called carrier ampholytes), with an acid at the anode (called the anolyte) and a base at the cathode (called the catholyte). When the electric field is applied (see Figure 2-4 below), a pH gradient forms as carrier ampholytes migrate to their p*I* and buffer the local pH. The gradient is stabilized by an influx of hydronium ions from the anolyte and hydroxide ions from the catholyte. Carrier ampholytes are generally a mixture of oligoamines with varying degrees of substitution by acidic functionalities, this mixture of compounds has a range of p*I*s depending on the pK_as of the functional groups in each carrier ampholyte compound.[106] Carrier ampholytes are available commercially in narrow

or wide pH ranges. Mixing carrier ampholytes from different suppliers or mixing a narrow pH range solution with a wide pH range solution can improve resolution in cIEF.[106] More carrier ampholytes possessing distinct p*I*s will provide increased separation between analytes with similar p*I*s.

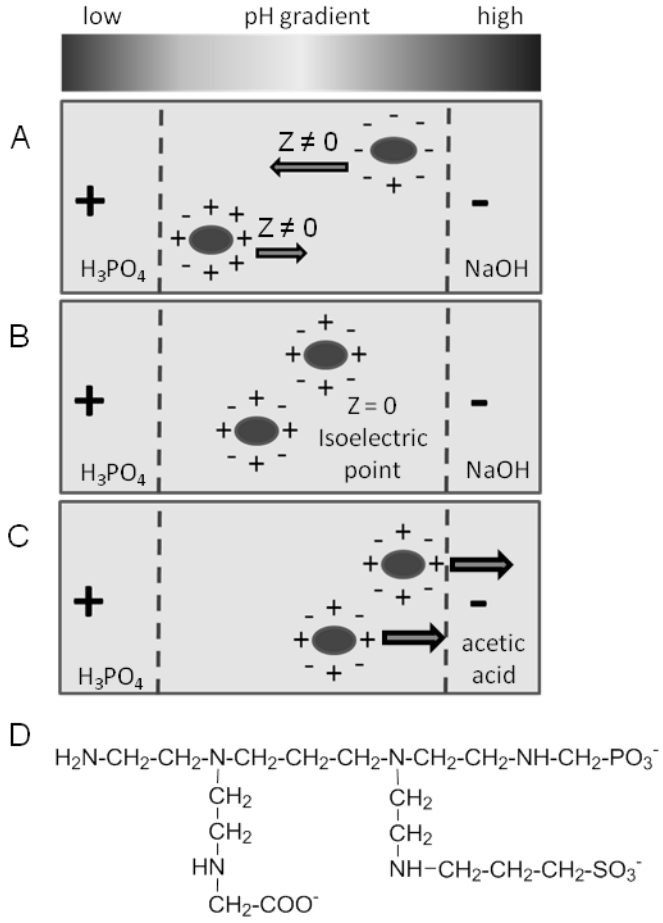

Figure 2-4. Isoelectric focusing. (A) Focusing step. The electric field is applied, the pH gradient forms, and analytes migrate toward their p*I*. Anolyte: H_3PO_4. Catholyte: NaOH. (B) Focusing complete. Analytes are focused at their p*I*. (C) Mobilization step. Catholyte is replaced with chemical mobilizer, acetic acid, and the pH gradient containing focused analytes migrates out of the capillary. (D) Possible structure of a compound found in a preparation of carrier ampholytes.

After focusing is complete in cIEF, the pH gradient must be mobilized past the detector (in instruments with a single-point detector; whole-column imaging instruments[97] do not require this step). Two main strategies for mobilization exist; hydrodynamic mobilization and chemical mobilization.[83] A third strategy called one-step cIEF, in which EOF drives the pH gradient toward the detector as focusing occurs, requires a dynamically coated capillary to achieve partial reduction of EOF and cannot achieve the resolution of the other methods.[107] In hydrodynamic mobilization, the pH gradient is forced out of the capillary by application of pressure to the inlet or vacuum to the outlet or by siphoning. Hydrodynamic mobilization can result in band broadening under conditions of laminar or turbulent flow. In chemical mobilization, the catholyte is replaced with an acid, the anolyte is replaced with a base, or a salt is added to either solution, and the electric field is reapplied.[83] Migration of ions into the capillary displaces the ampholytes and focused analytes toward the mobilization solution in an isotachophoretic process.[108]

In the cIEF experiments described in Chapter 3 of this work, a wide pH-range solution of carrier ampholytes was mixed with a narrow pH-range solution to achieve higher resolution in the pH range where mitochondria are focused. Sucrose was used to adjust the osmolarity of the solution to make it compatible with analysis of intact mitochondria. Chemical mobilization was used to avoid the possible loss of resolution caused by hydrodynamic mobilization. This method enabled the reproducible detection of distributions of individual mitochondrial isoelectric point. Changes to the mitochondrial

surface upon treatment with trypsin were also detected, demonstrating the ability to detect changes in mitochondrial surface composition.

2.4.4. Internal Standards

In CE experiments, internal standards are often used as EOF markers and to measure the limit of detection of the technique (by measuring the peak height or area). Monitoring the migration of a neutral marker (e.g. acetone, benzene, mesityl oxide)[109] is a straightforward way to measure the mobility of the EOF, but is more prone to error under conditions of reduced EOF or if the marker interacts with the capillary surface. A charged marker allows for measurement of EOF as long as the mobility of the marker is known in advance. In this work, fluorescein is used as an internal standard to measure the EOF, correct apparent mobilities of mitochondrial events, and monitor the detector alignment.[40]

In cIEF experiments, inclusion of several p*I* marker internal standards is crucial for monitoring the pH gradient, assigning p*I*s to analytes, and measuring the resolving power of the method. Baseline peak widths in time units of internal standards are used to determine the resolving power (Δp*I*) using Equation 2-1 below.

$$\Delta \mathrm{p}I = 3\sigma = 3\left(\frac{\left(w_{b,1} + w_{b,2}\right)/2}{4}\right)\left(\frac{|p\mathrm{I}_1 - p\mathrm{I}_2|}{|t_1 - t_2|}\right)$$

(Equation 2-1)

Better resolving power (smaller Δp*I*) results in better separation between analytes with similar p*I*; cIEF methods are capable of achieving resolving power better than 0.01 pH units.[110]

Multiple markers must be used because the pH gradient is nonlinear.[111] There are several causes of pH gradient nonlinearity. First, commercial preparations of carrier ampholytes do not contain compounds with a uniform distribution of p*I*s across the claimed pH range, generally containing more acidic ampholytes than basic ampholytes.[106] Mixing narrow pH range solutions of carrier ampholytes with broad range solutions also causes nonlinearity. Since EOF increases with increasing pH, compression of the pH gradient occurs in the basic region. Therefore, the most reliable determination of p*I* in a certain region should be made only with a linear fit between the two p*I* markers flanking that region.

In cIEF with UV-visible absorbance detection, proteins with known p*I* are commonly used as internal standards.[112] For instruments with fluorescence detection, the proteins must be derivatized, which may change their p*I*. For example, labeling of a protein's primary amines with fluorescein isothiocyanate replaces a positive charge with a negative charge.[113] Incomplete labeling of a protein may also produce products with a range of p*I*s. Dyes which preserve the native charge state such as Chromeo P540 have been designed to address this problem.[114] Besides the need to label them for fluorescence detection, other limitations of using proteins as internal standards include the fact that different isoforms may possess different p*I*s and that conformational changes such as denaturing can expose internal residues which affect p*I*. Synthetic peptides have also been used as pI markers, although these also require a labeling step for fluorescence detection.[111] Small molecule p*I* markers based on derivatization of fluorescein with

mono-*N* alkylated piperazines have been synthesized and used in cIEF.[115] These markers do not have the limitations associated with using proteins or peptides as p*I* markers and are stable and water-soluble. A set of four of these p*I* markers are used as internal standards in the cIEF experiments described in Chapter 3 in this work to accurately determine mitochondrial isoelectric points.

2.5. Modeling Isoelectric Point

2.5.1. Proteins and Particles

Measurement of the p*I* of proteins, synthetic nanoparticles, and biological particles is useful in their characterization for predicting separation conditions, confirming the identity of an unknown, evaluating the synthesis of a batch of nanoparticles, or detecting different species of bacteria or strains of viruses.[84,116,117] Prediction methods have been devised to understand better the relationship between structure and p*I*. Prediction of protein p*I* from primary amino acid sequences is a well-established and widely used technique which aids in identification of unknown proteins.[118,119] Briefly, the pK_as of all acidic or basic functional groups in the protein determine the net charge at a given pH. The p*I* of a given protein can be found by numerically solving an expression that relates the net charge at a given pH to the number and identity of all acidic and basic functional groups. This is represented in general form by Equation 2-2 below, where n_x is the number of each functional group x of a given pK_a in the composition of interest and α_x(pH) represents the respective electrical net charge

taking into account pH-dependent dissociation of the functional group. This process is described in detail in Chapter 4 and Appendix B of this work.

$$Z(\mathrm{pH}) = \sum n_x \alpha_x(\mathrm{pH})$$

(Equation 2-2)

Prediction of the p*I* of nanoparticles coated with mixtures of two different proteins has been reported using this strategy.[120] Chapter 4 of this work describes prediction of p*I*s of a more complex system, the mitochondrial outer membrane. This method represents a valuable new tool to model the heterogeneity of mitochondrial p*I* and can be used to predict changes in p*I* upon changes to surface composition.

2.5.2. Origin of Mitochondrial Isoelectric Point

Mitochondrial p*I* depends on the chemical composition of the mitochondrial outer membrane. The number and identity of ionizable functional groups of the cytosolic domains of phospholipids and proteins in the outer membrane influences the surface charge at a given pH. Mitochondrial outer membrane phospholipids have been determined experimentally.[121-125] Many mitochondrial outer membrane proteins have been identified (available in the UniProt[126] and Mitominer[127] databases), but quantitation of the complete outer mitochondrial membrane proteome has not yet been achieved.

Damage to proteins and phospholipids and post-translational modifications to proteins in the mitochondrial outer membrane will also influence mitochondrial p*I*. For example, phosphorylation of serine or threonine is a common post-translational modification that would add negative charge to the outer mitochondrial surface; this

modification would change the p*I*. Ubiquitination of outer membrane proteins is a critical signaling step in the elimination of mitochondria by the mitophagy pathway,[128] addition of ubiquitin to lysine residues would modify mitochondrial p*I*. Damage to mitochondrial proteins, such as carbonylation of lysine, arginine, and histidine residues,[129] would also result in changes to p*I*.

Mitochondrial p*I* has been determined previously in different models. Mitochondria from rat kidney and liver had average p*I*s of 3.9 and 4.4; this was determined by observing their migration across a microscope slide in buffers of varying pH.[130] Another similar study reported p*I*s of 4.65 to 4.75 for mitochondria isolated from rat liver.[131] A method known as cross-partitioning was used to determine average p*I*s of mitochondria from rat liver (5.2-5.4),[132] bovine heart (5.6),[133] and rat brain (4.5).[134] These methods all report an average value of mitochondrial p*I*. In the work described in Chapter 3, distributions of individual mitochondrial p*I* are determined, and Chapter 4 describes efforts to model the relationship between mitochondrial p*I* and surface composition. These methods provide valuable tools to measure mitochondrial heterogeneity in surface composition, and to understand and predict the modifications to the mitochondrial surface that may cause this heterogeneity. Increased insight into these mitochondrial properties could help to elucidate their role in the aging process and in age-related disease.

Chapter 3.

Capillary Isoelectric Focusing of Individual Mitochondria

Reprinted (adapted) with permission from Wolken, G. G., Kostal, V., Arriaga, E.A., "Capillary Isoelectric Focusing of Individual Mitochondria." *Anal. Chem.* **2011**, *83*, 612-618.

All data collection and analysis was performed by G. Wolken. Dr. V. Kostal advised on experimental design and method development. We thank Karel Slais (Institute of Analytical Chemistry of the ASCR, Brno, Czech Republic) for the kind gift of the p*I* markers.

Mitochondria are highly heterogeneous organelles that likely have unique isoelectric points (p*I*), which are related to their surface compositions and could be exploited in their purification and isolation. Previous methods to determine p*I* of mitochondria report an average p*I*. This article is the first report of the determination of the isoelectric points of individual mitochondria by capillary isoelectric focusing (cIEF). In this method, individual mitochondria enriched by differential centrifugation from cultured rat myoblast cells are labeled with the mitochondrial-specific probe 10-*N*-nonyl acridine orange (NAO). The mitochondria are then injected into a fused-silica capillary in a solution of carrier ampholytes at physiological pH and osmolarity, where they are focused then chemically mobilized and detected by laser-induced fluorescence (LIF). Fluorescein-derived p*I* markers are used as internal standards to assign a p*I* value to each individually detected mitochondrial event, and a mitochondrial p*I* distribution is determined. This method provides reproducible distributions of individual mitochondrial p*I*, accurate determination of the p*I* of individual mitochondria by the use of internal standards, and resolution of 0.03 pH units between individual mitochondria. This method could also be applied to investigate or design separations of organelle subtypes (e.g. subsarcolemmal and intermyofibrillar skeletal muscle mitochondria) and to determine the p*I*s of other biological or non-biological particles.

3.1. Introduction

Mitochondria are heterogeneous organelles responsible for energy production and for cellular signaling pathways such as apoptosis.[26] Mitochondrial dysfunction is

associated with diseases such as cancer and Parkinson's, and these organelles are thought to be involved in the aging process.[135] It is still unclear how important functional differences may arise from mitochondrial heterogeneity.[8] Due to this fact, methods that can distinguish between individual mitochondria are desirable. In particular, methods that underscore heterogeneity at the surface of mitochondria are desirable because it is the surface of these organelles that ultimately may regulate their participation in biological processes; for example, proteins such as the mitofusins are involved in regulating mitochondrial fusion and fission.[136]

Capillary electrophoresis (CE) is a technique useful for characterization of mitochondrial heterogeneity.[86] This technique has been used to analyze individual organelles and other biological particles.[85] In this method, organelles or particles are separated in an electric field based on differences in electrophoretic mobility. Individual mitochondria possess different electrophoretic mobilities due to differences in their morphology and outer membrane composition. However, some mitochondria may not exhibit differences in electrophoretic mobility but may still exhibit important functional differences stemming from variation in abundance of outer membrane proteins. Alternatively, isoelectric point (p*I*) is a property that may allow for characterization and separation of these mitochondria. There are no reports of determination of the p*I* of individual organelles.

Previous reports of mitochondrial p*I* vary depending on the source and method used to determine p*I*. Mitochondria from rat kidney and liver were found to have p*I*s of

3.9 and 4.4 by observing their migration time across a microscope slide in buffers of different pH.[130] Cross-partitioning revealed that rat liver,[132] bovine heart[133] and rat brain[134] mitochondria have p*I*s of 5.2 - 5.4, 5.6 and 4.5, respectively. The resolving power of this method is not well defined and the isoelectric point determination depends on the partitioning of the sample between phases of different electrostatic potential, requires multiple measurements at different pH, and consumes mL sample volumes. Microfluidic devices designed for free-flow isoelectric focusing have been used to determine that the p*I* of mitochondria from several cell lines lies between p*I* 4 and 5.[59] The resolving power of these devices is typically on the order of 0.2 pH units or higher, and they use sample amounts larger than those used for cIEF.[137] Clearly, while methods such as free-flow isoelectric focusing are ideal for sample enrichment on a preparative scale, they have inherent limitations in resolving power and detection sensitivity that make them unsuitable for investigation of small differences in mitochondrial p*I* and detection of individual mitochondria.

Capillary isoelectric focusing (cIEF) has been widely applied to the separation of proteins and is suitable for the analysis of biological particles such as microorganisms, viruses, and cells.[138, 139] This technique has exceptional resolving power (e.g., $\Delta pI \sim 0.01$ pH units) and requires only μL-scale volumes of sample. In the method described here, mitochondria are isolated from the cell and labeled with the cardiolipin-specific probe 10-*N*-nonyl acridine orange (NAO). The mitochondria are then suspended in a solution containing carrier ampholytes, p*I* marker internal standards,[115] and sucrose to maintain

physiological osmolarity. The carrier ampholytes are photobleached using a light-emitting diode to decrease their characteristic fluorescent background.[114] A fused-silica capillary coated with the neutral polymer hydroxypropyl cellulose[105] (HPC) to suppress electroosmotic flow is then filled with the mitochondrial suspension. The inlet and outlet are placed in anolyte and catholyte, respectively, and the mitochondria are then focused in the pH gradient formed by application of an electric field, and mobilized past an on-column detection point by replacing the catholyte with an acid.[83] Mitochondria are detected as narrow spikes, and p*I* markers are detected as broad peaks. To demonstrate the sensitivity of this technique to changes in the composition of the mitochondrial surface, the mitochondria are treated with the protease trypsin. This treatment cleaves cytosolic domains of mitochondrial membrane proteins and other proteins associated with the outer surface of mitochondria, altering the p*I*. Changes in p*I* as low as 0.03 pH units are clearly detected by the proposed methodology.

3.2. Experimental Section

3.2.1. Reagents and Materials

House deionized water was further purified with a Synergy purification system (Millipore, Billerica, MA) and was used in preparation of all buffers and solutions. Sodium hydroxide (NaOH), potassium hydroxide (KOH), phosphoric acid (H_3PO_4), 4-(2-Hydroxyethyl)piperazine-1-ethanesulfonic acid (HEPES), hydroxypropyl cellulose (HPC, average M_w = 100,000), tris(hydroxymethyl)aminomethane (tris), methanol, DMSO, and gentamicin were from Sigma-Aldrich (St. Louis, MO). Ethylene glycol-bis(2-

aminoethylether)-*N,N,N′,N′*-tetraacetic acid (EGTA) was from Amresco (Solon, OH). Acetic acid was from BDH Aristar (VWR, West Chester, PA). Sucrose was from Roche (Indianapolis, IN). D-mannitol was from Riedel de-Haën (Seelze, Germany). Fluorescein and 10-*N*-nonyl acridine orange (NAO) were from Molecular Probes (Invitrogen, Carlsbad, CA). Biolyte 3-10 and 4-6 carrier ampholytes (40% solutions) and phosphate buffered saline (PBS, 10×) were from Bio-Rad (Hercules, CA). Dulbecco's modified Eagle medium (DMEM), fetal bovine serum (FBS), and 0.5% trypsin (10×, 5 g/L trypsin, 2 g/L EDTA·4Na, 8.5 g/L NaCl) were from Gibco (Invitrogen, Carlsbad, CA). Trypan blue stain (0.4%) was from Bio-Whittaker (Walkersville, MD). The Pierce BCA protein assay kit was used for protein quantitation (Thermo, Rockford, IL). Sequencing grade modified trypsin was from Promega (Madison, WI), and was reconstituted according to the manufacturer's instructions. Fused-silica capillary tubing (50 µm I.D., 150 µm O.D., 12 µm polyimide coating) was from Polymicro (Phoenix, AZ). Fluorescent p*I* markers were a kind gift from Karel Slais, Academy of Sciences of the Czech Republic.

3.2.2. Buffers and Solutions

Mitochondrial isolation buffer contained 210 mM mannitol, 70 mM sucrose, 10 mM HEPES, and 5.0 mM EDTA, adjusted to pH 7.4 with 1 M KOH. The HEPES buffer contained 10 mM HEPES, adjusted to pH 7.4 with KOH. Digestion buffer contained 10 mM tris-HCl, 250 mM sucrose, and 0.1 mM EGTA, adjusted to pH 7.4 with KOH. All buffers were filtered to 0.2 µm before use. A stock solution of 5.2 mM NAO was prepared in DMSO and diluted with mitochondrial isolation buffer before use. A stock

solution of 2.25 mM fluorescein was prepared in methanol and diluted with HEPES buffer before use. Focusing solution contained 230 mM sucrose, 1% (w/v) Biolyte 3-10 carrier ampholytes, 1% (w/v) Biolyte 4-6 carrier ampholytes, and the four internal standard fluorescent p*I* markers at a concentration of 0.02 ng/mL each. The carrier ampholytes were first photobleached overnight with a 120 mW LED with λ_{max} at 472 nm.[114] Anolyte, catholyte, and chemical mobilizer solutions for cIEF were, respectively, 100 mM H_3PO_4, 20 mM NaOH, and 350 mM acetic acid.

3.2.3. Cell Culture

Adherent L6 rat myoblast cells (ATCC, Manassas, VA) were cultured in vented 75 cm^2 flasks at 37° C and 5% CO_2 in DMEM supplemented with 10% FBS and 0.01 mg/mL gentamicin. Cells were split every 2-4 days after reaching 90% confluence by rinsing with 1× PBS, releasing with 0.5% trypsin in PBS, and seeding back into the flask with fresh DMEM at a 1:40 splitting ratio.

3.2.4. Mitochondrial Preparation

Mitochondria were prepared using mechanical homogenization and differential centrifugation procedures.[78] Cells were harvested with 0.5% trypsin in PBS and the cell suspension was added to an equal volume of DMEM. All subsequent procedures were performed on ice or at 4° C unless otherwise noted. Cells were washed three times with mitochondrial isolation buffer and resuspended at an approximate concentration of 5.6 × 10^6 cells/mL. The cells were disrupted using a glass Potter-Elvehjem homogenizer (Kontes, Vineland NJ) using a 0.06 mm clearance pestle. To measure cell density and

homogenization efficiency, aliquots of cells were stained with trypan blue dye before and after homogenization and counted with a Fuchs-Rosenthal counting chamber (Hausser Scientific, Horsham, PA). Cell breakage above 90% was achieved by applying a sufficient number of strokes with the homogenizer and counting the remaining undisrupted cells. After homogenization, intact cells, nuclei, and cellular debris were eliminated from the preparation by centrifuging at 600 g for 10 minutes. Mitochondria in the supernatant were pelleted by centrifuging at 10,000 g for 10 minutes and resuspended in mitochondrial isolation buffer. Mitochondria were labeled by incubating with 5 µM NAO for 10 minutes in the dark. The mitochondria were then pelleted by centrifuging at 10,000 g for 10 minutes and resuspended in mitochondrial isolation buffer. This step was performed two additional times to wash the mitochondria. Mitochondria were then kept on ice until analysis by cIEF. Immediately prior to analysis, aliquots of this mitochondrial suspension were diluted 1:5 with mitochondrial isolation buffer.

3.2.5. Trypsin Treatment

The procedure for trypsin treatment of mitochondria was reported by Forner *et al*.[140] The above preparation procedure was followed until the step before NAO labeling. At this point, mitochondria were instead resuspended in digestion buffer and split into two aliquots. Total protein in the mitochondrial suspensions was determined by the BCA assay. Sequencing grade modified trypsin was reconstituted in the provided solution (1 M acetic acid), heated at 30° C for 30 minutes, and then added to one mitochondrial sample in a 50:1 protein: trypsin ratio. Mitochondrial suspensions were then gently mixed

overnight on a rotational gel shaker at 4° C. After this overnight digestion, mitochondria were labeled by NAO and washed with mitochondrial isolation buffer according to the above procedure, then analyzed by cIEF according to the procedure below.

3.2.6. Instrument Description

A homebuilt capillary electrophoresis instrument which has been described previously[141] has been adapted to cIEF for this work. A sample carousel was added to the outlet of the capillary for delivery of catholyte and chemical mobilizer. The 488 nm light from a 15 mW Ar^+ laser (Melles-Griot, Carlsbad CA) was focused onto the detection window of the capillary. Light was collected at 90° to the laser by a 40×, 0.55 NA objective (New Focus, San Jose, CA). Scattered laser light was eliminated with a 488RU scattering filter (Semrock, Rochester, NY), and fluorescence was passed through a pinhole and a 535 ±17.5 nm band-pass filter (Omega Optical, Brattleboro, VT) onto a photomultiplier tube (R1477, Hamamatsu, Bridgewater, NJ) biased at 1000 V.

3.2.7. Capillary Preparation

Fused-silica capillaries were coated with HPC by a method adapted from Shen *et al.*[105] Briefly, three capillaries were rinsed with methanol, 1.0 M NaOH, 0.1 M NaOH, and H_2O for 10 minutes each by flushing under 10 psi nitrogen pressure. The capillaries were purged and flushed with a 5% (w/v) HPC solution for 1 hour. The solution was then purged from the capillaries. After purging, the capillaries were heated between two resistant plates with temperature controlled by a variable-voltage power source from 60 to 140 °C in ~15 minutes, and then holding at 140 °C for 30 minutes. The HPC flush, N_2

purge, and heating steps were repeated once for a more robust coating. Capillaries were stored dry until use. Before use, the inlet and outlet were trimmed and the polyimide coating was burned off at the detection window to produce capillaries with total length 38.9 cm and effective length 35.7 cm.

The HPC-coated capillary was first installed in the instrument and aligned by flushing a 1×10^{-9} M solution of fluorescein in HEPES buffer by application of pressure to the inlet. The limit of detection and electroosmotic flow were then determined by measuring the peak height and electrophoretic mobility of an electrokinetically-injected sample of 1×10^{-10} M fluorescein in HEPES buffer. The limit of detection was determined to be 29 ± 4 zeptomoles (average ± std. dev.; n = 3). The electroosmotic flow was calculated as the difference between fluorescein's apparent electrophoretic mobility and net electrophoretic mobility of $-3.0 \pm 0.1 \times 10^{-4}$ $cm^2 \cdot V^{-1} \cdot s^{-1}$ at pH 7.4.[78] The EOF was determined to be $4.26 \pm 0.07 \times 10^{-5}$ $cm^2 \cdot V^{-1} \cdot s^{-1}$ (n = 3). This reduction from the value of $5.1 \pm 0.1 \times 10^{-4}$ $cm^2 \cdot V^{-1} \cdot s^{-1}$ (n = 15) for uncoated fused silica indicated an effective suppression of EOF by the capillary coating.

3.2.8. cIEF Procedure

To perform the cIEF procedure, the capillary was rinsed first with methanol for 15 minutes, water for 5 minutes, then a solution mixture of 230 mM sucrose, 1% Biolyte 3-10, and 1% Biolyte 4-6 for 10 minutes. A mitochondrial suspension to be analyzed by cIEF was first mixed gently with a pipettor, and then a 2 µL aliquot of this suspension was added to 50 µL of focusing solution and mixed. The sample was introduced to the

capillary by application of 20 kPa to the inlet end. The PMT signal was monitored during injection to ensure complete filling of the capillary (a total volume of 760 nL). After injection, the outlet of the capillary was rinsed once in a 0.5 mL vial of catholyte, and then switched to the running vial of catholyte. The inlet was rinsed once in a vial of anolyte, and then switched to the running vial of anolyte. An electric field of 400 V/cm was applied, and the PMT and current signals were monitored during focusing. After the current decreased and reached a plateau indicating completion of focusing (for the experiment shown in Figure 3-1, the current changed from -44 μA to -7 μA in 931 seconds), the outlet of the capillary was switched to a chemical mobilization solution of 350 mM acetic acid and the electric field was re-applied. Focused zones were then mobilized past the detector (cathodic mobilization). Between runs, the capillary was rinsed with methanol, water, and the sucrose-Biolyte solution. After the analysis, the capillary was flushed with methanol and water, then purged with air and stored dry.

3.2.9. Data Analysis

Data from the PMT was acquired at 100 Hz, digitized by an I/O data acquisition card (PCIMIO-16E-50) operated by Labview 5.1 software (National Instruments, Austin, TX), and stored as a binary file. Data was analyzed in Igor Pro software (Wavemetrics, Lake Oswego, OR) by a procedure written in-house which has been described previously, PeakPicks.[101] Briefly, electropherograms were median filtered to separate narrow spikes (peaks with baseline widths smaller than 50 data points, or 0.50 s) from broad peaks (p*I* markers and fluorescent species in the carrier ampholytes), as shown in Figure 3-2.

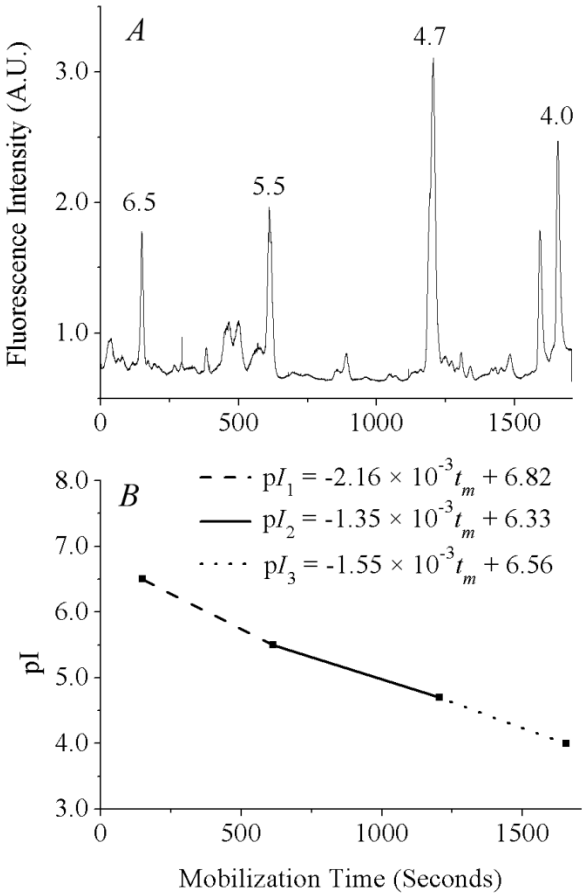

Figure 3-1. pH gradient determination using internal standards. (A) Signal from fluorescent p*I* markers after median filtering to remove narrow spikes. Separation conditions: 1% Biolyte 3-10, 1% Biolyte 4-6, 230 mM sucrose, 0.02 ng/mL of each fluorescent p*I* marker. The anolyte, catholyte, and chemical mobilizer were 100 mM H_3PO_4, 20 mM NaOH, and 350 mM acetic acid. The electric field applied during focusing and mobilization was 400 V/cm. Detection was at 535 ± 17.5 nm, data acquisition was at 100 Hz, 1000 V was applied to the PMT. (B) pH gradient, as determined by mobilization times of the four p*I* markers.

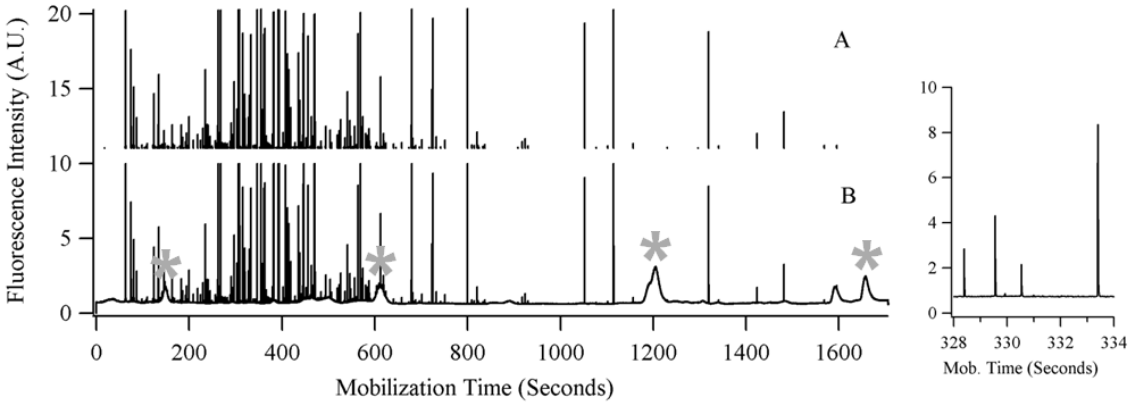

Figure 3-2. Signal processing to select mitochondrial events. (B) Signal during mobilization step of focused mitochondria and p*I* marker internal standards. Narrow spikes represent individual mitochondrial events; broad peaks represent p*I* markers or fluorescent species from the carrier ampholytes. The p*I* markers are indicated with an asterisk (*). (A) Mitochondrial events selected after application of median filter and clipping of the lower signal. There are 360 mitochondrial events detected. The inset at the right is an expanded view of a crowded section of the electropherogram showing the resolution between individual spikes.

For example, the spikes selected in one experiment had baseline widths of 0.05 ± 0.01 seconds (avg. ± std. dev, n = 405) and the p*I* marker peaks had baseline widths of 25 ± 9 seconds (avg. ± std. dev, n = 4). The mobilization times of the p*I* markers were used to define the pH gradient, and the peak widths were used to determine the resolving power of the method. Mitochondrial events were then selected over noise by selecting any spikes with signal intensity above a threshold of five standard deviations over the background signal. A mitochondrial event is defined as an individual, intact mitochondrion, a mitochondrial fragment, an aggregate of multiple mitochondria, or a false positive (another organelle or particle exhibiting green fluorescence or a random deviation of the background above the threshold). The threshold limits the number of false positives detected to less than 5% of the total number of detected mitochondrial

events (determined by analysis of both an unlabeled and NAO-labeled mitochondrial preparation, see Appendix A, Figure A-1 for details). Each mitochondrial event was then assigned an individual p*I* based on its mobilization time.

3.2.10. Peak Overlap

An issue in analysis of particles by capillary electrophoresis is whether peak crowding is a problem; i.e. whether observed peaks represent individual or multiple co-migrating components. Statistical overlap theory has been applied to this problem to determine a threshold for peak saturation, below which the number of observed peaks is a good estimate for the number of actual peaks, and so the effect of peak overlap on the observed distribution is minimal.[142] We have applied this statistical test to each mitochondrial cIEF experiment and have found that peak overlap is not a significant problem (see Appendix A, Section A.2. for details).

3.3. Results and Discussion

3.3.1. Photobleaching of Carrier Ampholytes

Commercial preparations of carrier ampholytes are known to contain fluorescent species.[143] This increases the background in cIEF with laser induced fluorescence detection, so it is necessary to photobleach the carrier ampholytes to reduce this background. Ramsay et al. demonstrated an elegant and simple method for reducing the background from the carrier ampholytes by photobleaching them with light emitting diodes with λ_{max} matching that of the laser used for excitation.[114] We employed this method using a blue LED with λ_{max} at 472 nm to photobleach a 1:1 mixture of 40%

Biolyte 3-10 and 40% Biolyte 4-6 overnight. After photobleaching, the reduction in background fluorescence from the carrier ampholytes was measured by focusing and mobilizing a solution with 2% Biolyte 3-10, 2% Biolyte 4-6, and 220 mM sucrose. The average signal from the untreated carrier ampholytes was 3.6 ± 1.8 V, as compared to 1.1 ± 0.4 V for the photobleached carrier ampholytes (see Appendix A, Figure A-2 for details). This reduction in background signal results in an increase in sensitivity necessary to detect individual mitochondria.

3.3.2. pH Gradient and p*I* Determination

After the signal from the PMT is median-filtered to separate narrow spikes from broader peaks, the mobilization times (t_m) of the four p*I* markers are used to determine equations relating t_m to p*I*. Since the shape of the pH gradient is dependent on the EOF, which is in turn dependent on the integrity of the capillary coating (we observed an increase in the EOF from 4.26 ± 0.07 × 10^{-5} $cm^2 \cdot V^{-1} \cdot s^{-1}$ directly after coating to 5.78 ± 0.04 × 10^{-5} $cm^2 \cdot V^{-1} \cdot s^{-1}$ after five days and 14 cIEF runs), these internal standards are necessary to compare p*I* data from run to run. For example, the equations for the pH gradient for the experiment shown in Figure 3-1 are given below.

$$pI_1 = -2.16 \times 10^{-3} t_m + 6.82 \qquad \text{(Equation 3-1A)}$$

$$pI_2 = -1.35 \times 10^{-3} t_m + 6.33 \qquad \text{(Equation 3-1B)}$$

$$pI_3 = -1.55 \times 10^{-3} t_m + 6.56 \qquad \text{(Equation 3-1C)}$$

Each mitochondrial event is assigned a p*I* using the appropriate equation for its mobilization time. Events which are mobilized past the detection point before the p*I* 5.5

marker are assigned a p*I* using the first equation, events which are detected between the p*I* 5.5 and 4.7 markers are assigned a p*I* using the second equation, and events detected after the 4.7 marker are assigned a p*I* using the third equation. We used this method, rather than using a single fit to describe the pH gradient, for two reasons. First, the pH gradients produced in cIEF with commercial preparations of carrier ampholytes are not linear.[111] The causes of nonlinearity include compression of the pH gradient in the basic region by residual EOF, the presence of fewer basic than acidic carrier ampholytes in commercial preparations, and local effects on the gradient by the analytes themselves.[144] Second, the gradient should not be linear across the entire pH range because we used a mixture of narrow (4-6) and wide-range (3-10) carrier ampholytes. Therefore, the most reliable determination of p*I* in a certain region should be made only with a linear fit between the two p*I* markers flanking that region.

For three replicate analyses of isolated mitochondria, the mean p*I* was determined to be 5.9 ± 0.6 and the median p*I* was 6.0 (see Table 3-1). These values are slightly higher than previous reports of mitochondrial p*I* mentioned in the introduction, which range from 3.9 to 5.6. These differences could be accounted for by: (i) the different mitochondrial sources, (ii) variations in sample preparation and purification, and (iii) technique biases. Mitochondria in previous determinations were obtained from rat liver, kidney, and brain, bovine heart, and several types of cell cultures, including HT-29 cells, HeLa cells, and NR6wt murine fibroblasts.[59,130,132-134] Different disruption procedures could cause variations in their outer surface characteristics such as those resulting from

different levels of cytoskeletal components that were not removed during the isolation procedure.[62] Lastly, some of the previous methods give an indirect measurement of p*I* (i.e. cross partitioning or observation of electrophoretic mobility at different pH), and did not include p*I* standards.

Table 3-1. Mitochondrial p*I* statistics from three consecutive cIEF runs.

	Run number			
	1	2	3	pooled
number of mitochondrial events	451	360	405	1216
median p*I*	6.0	6.0	6.0	6.0
mean p*I*	5.9	5.9	5.9	5.9
standard deviation	0.6	0.5	0.6	0.6
minimum p*I*	3.9	4.1	3.9	3.9
maximum p*I*	6.9	6.8	6.8	6.9

3.3.3. Resolving Power and Accuracy

It is informative to determine the resolving power of the method (the minimum difference in p*I* analytes must possess to be separated). The peak standard deviations σ of two adjacent p*I* markers, measured in time units, can be used to determine the resolving power in p*I* units using the following equation.

$$\Delta pI = 3\sigma = 3\left(\frac{(w_{b,1}+w_{b,2})/2}{4}\right)\left(\frac{|pI_1-pI_2|}{|t_1-t_2|}\right) \qquad \text{(Equation 3-2)}$$

For the experiment shown in Figure 3-1, an average resolving power of 0.03 pH units is calculated. This is comparable to previous reports of resolving power in cIEF.

However, the true resolving power of the method for mitochondria should be better than 0.03. Individual mitochondrial events are detected not as broad peaks consisting of a distribution of an analyte focused at its p*I*, but as narrow spikes with width defined by their migration time through the laser beam.

The accuracy of the p*I* determination is limited by the accuracy to which the true p*I*s of the standards are known. Since p*I* is temperature-dependent and the p*I*s of the standards are reported to one decimal place, we report mitochondrial p*I*s with an accuracy of ±0.1 pH units. A full propagation of error on the formula used to calculate individual p*I* from the internal standards supports this conclusion (see Appendix A, section A.4. for details).

3.3.4. Reproducibility of the Mitochondrial p*I* Distribution

Reproducibility of this technique was assessed by performing three consecutive analyses of the same mitochondrial sample. While the data can be represented statistically as in Table 3-1 or graphically as in Figure 3-3, the quantile-quantile plot (q-q plot) can be used to demonstrate the reproducibility of the distributions more clearly. This plot is produced by graphing the 5^{th} through 95^{th} percentiles of each individual run against the average percentiles of the three runs, and has been used previously to compare mitochondrial migration time distributions in capillary electrophoresis.[145] The mitochondrial p*I* distributions are considered to be qualitatively similar since the majority of the data falls very close to the line. Visual inspection of the q-q plot in Figure 3-4

indicates that the distributions are more reproducible above p*I* 5.5. Additionally, the sum of squares of the residuals (ss_{res}) can be used as a metric for reproducibility:

$$ss_{res} = \sum_i \left(pI_{i,1} - pI_{i,2}\right)^2, i = 5\%, 10\%, \cdots, 95\% \qquad \text{(Equation 3-3)}$$

For the three consecutive runs, the ss_{res} are 0.015, 0.150, and 0.145 respectively for runs 1, 2, and 3. We will therefore consider distributions to be different if their q-q plot produces a sum of squares of residuals larger than 0.150.

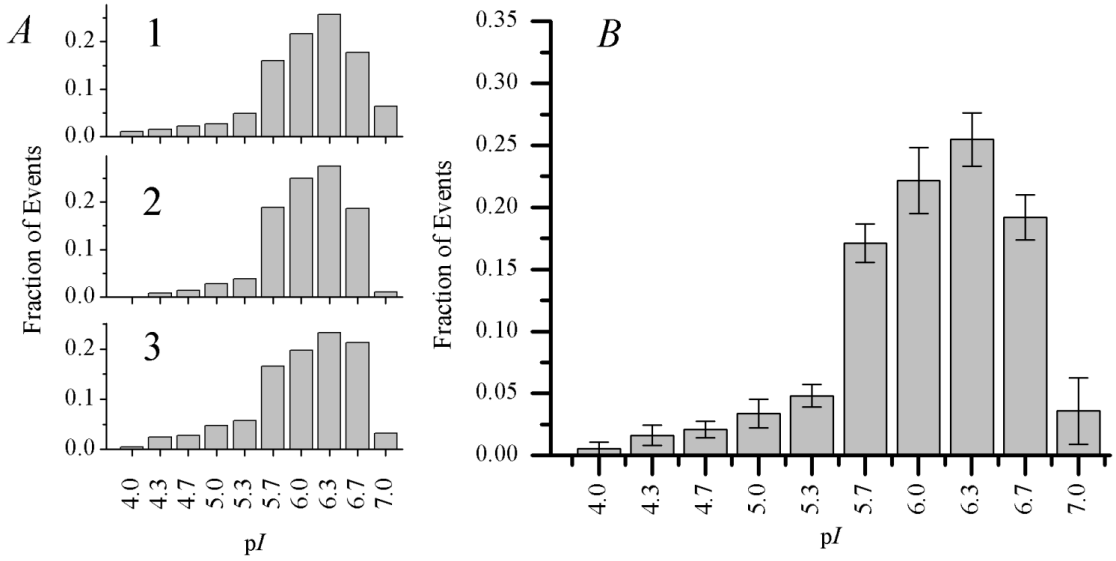

Figure 3-3. Mitochondrial p*I* distributions from three consecutive cIEF runs. (A) Individual distributions from each run. The total number of mitochondrial events detected is 451, 360, and 405 for 1, 2, and 3. Each plot is normalized to the total number of mitochondrial events from that run. (B) Mitochondrial p*I* distribution, pooled from the three consecutive cIEF runs. Error bars for each bin represent plus or minus one standard deviation between the three runs. The total number of mitochondrial events detected is 1216.

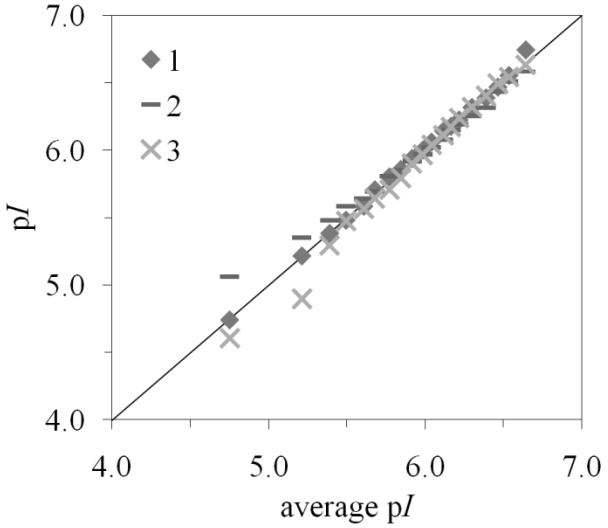

Figure 3-4. Q-Q plot to assess reproducibility of three consecutive cIEF runs. The percentiles from each run (*y*-axis) are plotted against the percentiles of the pooled data (*x*-axis). This plot is a qualitative indication that the distributions are very reproducible above p*I* 5.5. The sums of squares of the residuals are 0.015, 0.150, and 0.145 respectively for runs 1, 2, and 3.

3.3.5. Variation of Mitochondrial p*I*

Biological variation and variations in sample preparation are expected to affect mitochondrial p*I* distributions determined with this technique. First, natural biological variation between cells and individual mitochondria could be responsible for differences in p*I* – mitochondria from cells at different passage numbers (different age), and different stages in the cell cycle may exhibit different surface characteristics. Within the cell, mitochondria are a dynamic network of organelles which undergo morphological changes during fusion and fission and with changes in cellular energy status.[146] Different proteins localized to the surface of mitochondria at different stages of the cell cycle or differences in mitochondrial morphology could affect mitochondrial p*I*. Secondly, differences in sample preparation could cause variation in p*I*. Harsher homogenization of the cells or

variation in pipetting during resuspension of the mitochondrial pellets could affect mitochondrial surface characteristics. It has been previously shown that variations in sample preparation and storage conditions affect mitochondrial electrophoretic mobility.[62] In fact, there is a difference in the p*I* distributions of freshly-isolated mitochondria described in Table 3-1 and untreated mitochondria stored overnight described in Table 3-2. We attribute this difference to variations in sample preparation and the different storage conditions. The experiment described in Table 3-1 was performed with freshly-isolated mitochondria, and the experiment described in Table 3-2 used mitochondria that were stored overnight at 4° C in a different buffer. However, these sources of variation should not affect the utility of the technique to determine mitochondrial p*I* distributions as long as proper controls are used.

Table 3-2. Effect of overnight trypsin treatment.*

	untreated	trypsin-treated
number of mitochondrial events	461	432
median p*I*	5.8	5.7
mean p*I* **	5.7	5.6
standard deviation	0.7	0.6
minimum p*I*	3.9	3.9
maximum p*I*	6.8	6.8

* Data is pooled from two cIEF runs of each sample.

** The difference in the means is statistically significant, $p = 0.0181$.

3.3.6. Effect of Trypsin Treatment

Trypsin is a protease that digests proteins by hydrolytic cleavage of the peptide backbone at the C-terminus of lysine and arginine residues.[147] Treatment of a mitochondrial preparation with trypsin should cleave proteins associated with the mitochondrial outer membrane, the cytosolic domains of mitochondrial outer membrane proteins, and cytoskeletal proteins attached to mitochondria.[39,140] We analyzed untreated and trypsin-treated mitochondria by cIEF (two replicate analyses of each sample) and found the mitochondrial p*I* distribution to be shifted. Examining the q-q plots in Figure 3-5 reveals that there is a greater difference between the p*I* distributions of untreated and trypsin-treated mitochondria than there is between replicate analyses of either sample. When comparing the pooled data from the two cIEF runs of trypsin-treated mitochondria to the pooled data from the untreated mitochondria (Table 3-2), the ss_{res} is 0.335 (Figure 3-5 A). This value is larger than the ss_{res} of 0.143 for the comparison of two replicate runs of trypsin-treated mitochondria (Figure 3-5 B) and 0.081 for the comparison of two replicate runs of untreated mitochondria (Figure 3-5 C). The ss_{res} of 0.143 and 0.081 are also comparable to those calculated for replicate runs of the same sample in the above section. The median p*I* of the trypsin-treated mitochondria (5.7) was 0.1 pH units lower than that of the untreated mitochondria. This p*I* difference could not have been detected with other techniques with resolving power higher than 0.1. The mean p*I* was also lower (see Table 3-2). The means were statistically different, $p = 0.0181$. More information about the p*I* distribution can be gained from examining the q-q plot; the plot in Figure 3-5

A indicates that the trypsin-treated p*I* distribution is shifted to lower p*I* but approximately the same shape as the untreated distribution. From this we can conclude that trypsin treatment decreases the net charge on the surface of mitochondria, by cleavage of mitochondrial and mitochondrial-associated proteins and cytoskeletal components.

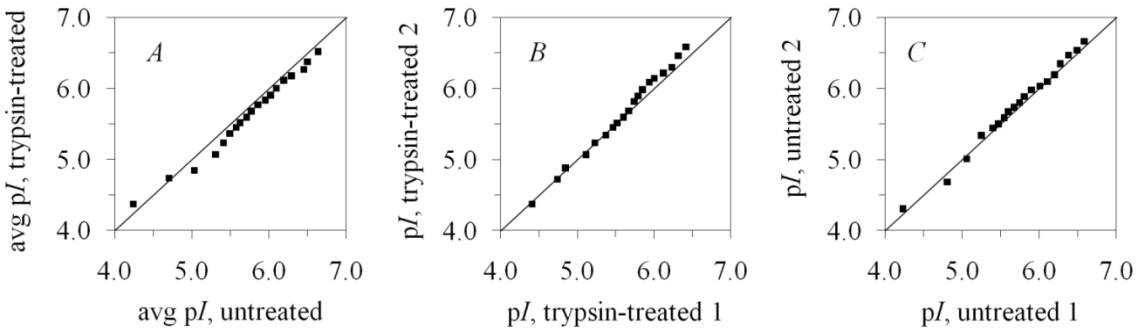

Figure 3-5. Q-Q plots showing the effect of trypsin treatment on the p*I* of mitochondria. The sums of squares of the residuals are 0.335, 0.143, and 0.081 respectively for A, B, and C, indicating that trypsin treatment changes the mitochondrial p*I* distribution. The majority of points in A fall below the line, indicating that the trypsin-treated p*I* distribution is shifted to lower p*I*.

3.4. Conclusions

We have presented a method for the determination of the p*I* of individual mitochondria by cIEF with laser-induced fluorescence detection. The use of fluorescent internal standards provides an accurate determination of mitochondrial p*I*. The ability to determine the p*I*s of individual mitochondria is an important tool for characterizing mitochondrial heterogeneity and detecting changes to the composition of the surface of mitochondria. The fact that mitochondria exhibit a p*I* distribution reveals that they are a heterogeneous population with different surface characteristics; e.g. mitochondria with a lower p*I* may express a higher abundance of a protein with a low p*I*. This method is

sensitive to changes in the mitochondrial p*I* distribution upon treatment with trypsin, which modifies the proteins associated with the surface of the mitochondria. This method could also be used to determine the p*I* of other biological or synthetic particles, provided an appropriate fluorescent labeling strategy exists. One limitation of the method is the definition of the pH gradient above the p*I* 6.5 marker – it has been established that commercial preparations of carrier ampholytes are limited in the basic regions, and EOF distorts the pH gradient more at higher pH. This issue could be improved by using different ranges of carrier ampholytes or an improved capillary coating to better suppress EOF.[148] Additionally, there is a need for fluorescent p*I* standards with higher p*I* for more accurate definition of the pH gradient in the basic regions. The speed and throughput of cIEF is also not ideal. Multicapillary[149] and microfluidic[150] IEF devices are promising in adapting this technique to a preparative format to collect isolated fractions separated by p*I*. Further developments of isoelectric focusing techniques may also have an impact on the characterization and purification of synthetic nanoparticles that exhibit differences in ζ-potential.[116]

Chapter 4.

Predicting Isoelectric Points of Non-functional Mitochondria from Monte Carlo Simulations of Surface Compositions

Code for the simulations was written and executed by B. Fossen and A. Noh. All additional data collection and analysis was performed by G. Wolken. This work was carried out in part using computing resources at the University of Minnesota Supercomputing Institute.

Mitochondria are heterogeneous organelles involved in energy production, metabolism, and cellular signaling that oftentimes are isolated from cells for chemical characterization (e.g. proteomic analysis). The chemical composition of the mitochondrial outer membrane is one of the factors defining mitochondrial isoelectric point (p*I*), which is a property useful for the analysis and characterization of isolated mitochondria. We previously used capillary isoelectric focusing (cIEF) with laser-induced fluorescence detection to determine the experimental p*I* of individual mitochondria after their isolation under depolarizing conditions. This technique revealed that, when kept non-functional, mitochondrial p*I* is heterogeneous as displayed by the observed distributions of p*I*. To model the effect of surface composition on p*I* heterogeneity of these mitochondria, we devised a method to predict mitochondrial p*I*s using simulated surface compositions. The method was initially validated by predicting the p*I*s of known mitochondrial outer membrane proteins and then extended to isolated mitochondria, in which both ionizable amino acids and phospholipids contribute to mitochondrial p*I*. After using a Monte Carlo method to generate a library of over two million possible mitochondrial surface compositions, sufficient compositions to match the frequency of occurrence of experimental mitochondrial p*I*s were randomly selected. This comparison allows for association of a given individual mitochondrial p*I* with thousands of randomly chosen compositions. The method predicts significant changes in the percentages of some amino acids and phospholipids for observed p*I* differences

between individual mitochondria, which is an important advancement toward explaining the observed heterogeneity of mitochondrial p*I*.

4.1. Introduction

The p*I* of a synthetic or biological particle refers to those conditions that lead to a net surface charge of zero under which the particle does not experience an electrical force in the presence of an electric field. For biological particles such as mitochondria, the surface charge depends on the ionizable functional groups of the molecules on the surface and their transmembrane potential, which arises from an electrochemical gradient across the membrane established to drive metabolic processes within the cell. [151,152] Measurement of the p*I* of synthetic nanoparticles[116] or non-functional biological particles[84,117] such as viruses allows for their analytical separation. Calculation of an analyte's p*I* is useful to optimize separation conditions in electrophoresis and to help identify unknowns in isoelectric focusing, a technique in which analytes are separated based on their p*I*. Prediction of protein p*I* from amino acid sequences is a well-established technique,[118] and the p*I* of particles can be predicted based on their surface properties. This has been done with simple particles (e.g. nanoparticles coated with mixtures of two different proteins),[120] but has not been attempted with more complex biological particles with a heterogeneous surface composition. Isoelectric focusing techniques such as gel electrophoresis with immobilized pH gradients and cIEF are powerful separations methods capable of high resolution and excellent peak capacity.[153] While these techniques are typically used to separate proteins, they are adaptable to

biological particles; we introduced the use of cIEF to separate individual non-functional mitochondria by p*I*.[154] We determined that mitochondria from a cultured cell line possess a range of p*I*s, a reflection of the biological heterogeneity of their surface compositions.

Here we report a simulation of the mitochondrial outer membrane to investigate heterogeneity in surface composition and model an experimentally determined p*I* distribution of non-functional mitochondria. Monte Carlo methods are used to generate compositions composed of percentages of phospholipids and amino acids; a p*I* is then calculated for each composition. We used the model to produce a distribution of surface compositions matching an experimentally determined mitochondrial p*I* distribution. This model allowed us to examine differences in possible surface compositions with a given p*I* and to compare compositions with different p*I*s, which are essential to assess variations in individual mitochondrial p*I* measurements and to monitor changes in their surface compositions. Along with future experimental work to measure the p*I*s of functional mitochondria, this model could be used as a basis to describe the dependence of mitochondrial p*I* on transmembrane potential.

4.2. Model and Simulations

4.2.1. Overview of Model

This model is made up of a library of theoretical mitochondrial surface compositions with p*I* from 4 to 9. Each composition can be thought of as a membrane surface made up of different percentages of seven ionizable amino acids and five phospholipids (see Table 4-1). These compositions are generated by randomly selecting

numbers of each amino acid and phospholipid within constraints defined by a set of initial conditions based on literature and theoretical values. The p*I* of each composition is determined by finding the pH at which the net charge of the composition is zero.

4.2.2. Initial Conditions of Model

The initial conditions of the model are defined by different percentages of amino acids and phospholipids contributing to mitochondrial p*I*. The complete proteome of the outer mitochondrial membrane is unknown, so instead of using the relatively limited set of known outer membrane proteins, we determined initial conditions for the amino acid component of the model by defining an "average protein" using information on all known protein sequences contained in the UniProt Knowledgebase protein database (accessed Dec. 18, 2009).[126] It is anticipated that the potential bias is minimal because the composition of the "average protein" is very similar to that of the average composition of the set of known mitochondrial outer membrane proteins (see Table B-2 in Appendix B).

We determined that the "average protein" has 351 amino acids, a molecular weight of 45283 Da, and a ratio of 0.04528 mg protein/nmol protein. Assuming ionizable amino acids that contribute to p*I* are located only in hydrophilic domains of the protein on the inside and outside of the mitochondrial outer membrane, and that the inner and outer domains are of equal size, we calculate that each "average protein" has 53 ionizable amino acids on the outer surface of the membrane.

We have included five phospholipids that contribute to mitochondrial p*I* (see Table 4-1). Our choices were based on previous experimental determinations of

phospholipids in mitochondrial outer membranes.[121-125] Based on these determinations, we calculated a ratio of 52.76 mol phospholipid per mol protein in our model. Combining this ratio with our assumptions about the "average protein," we calculate a ratio of 1.0 mol phospholipid per mol ionizable amino acid for the outer membrane surface. These initial conditions (shown in Table 4-1) are then used by the simulation to generate a library of compositions. See Appendix B for a complete description of how the initial conditions were determined.

4.2.3. Hierarchy of Simulation

In this simulation, two programs work together to generate a library of compositions and a match to experimental data. A flowchart of the general scheme of the simulation is shown in Figure 4-1. The two programs, one to generate the mitochondrial library and one to match the experimental data (boxes with solid red outlines in the flowchart in Figure 4-1), were written in Matlab (MathWorks, Natick MA, USA) and are available upon request. Input and output data (boxes with blue dashed outlines or green background in the flowchart in Figure 4-1) was saved as Microsoft Excel or text files. The first program uses a set of initial conditions (Table 4-1) to generate a library of approximately 2 million possible compositions using a Monte Carlo approach. Each composition had 10000 relevant molecules including both amino acids and phospholipids. Compositions were randomly generated with restrictions that the numbers of each amino acid and phospholipid must represent a composition within 50% and 20%, respectively, of the initial composition (whole number values of amino acids

Table 4-1. Initial conditions.

Amino acids and phospholipids	Ionizable functional group(s)	pK_a	Initial composition (mol %)
aspartic acid (asp)	carboxy	4.05	9.06
glutamic acid (glu)	carboxy	4.45	11.26
cysteine (cys)	sulfhydryl	9.00	2.26
tyrosine (tyr)	phenol	10.00	4.84
histidine (his)	imidazole	5.98	3.78
lysine (lys)	amine	10.00	9.75
arginine (arg)	guanidino	12.00	9.21
phosphatidylcholine (PC)	phosphate, quaternary ammonium cation	0.8, n/a	23.72
phosphatidylethanolamine (PE)	phosphate, amine	0.5, 9.6	18.91
phosphatidylinositol (PI)	phosphate	1.0	2.94
phosphatidylserine (PS)	phosphate, carboxy, amine	2.3, 3.6, 9.8	0.39
cardiolipin (CL)	phosphate, phosphate	2.8, 8.5	3.89
Total			**100%**

pK_as for amino acids were taken according to Bjellqvist et al.[119] pK_{a1} for PC, PE, and PS was determined by Moncelli et al.[155] pK_{a2} for PE and pK_{a2}, pK_{a3} for PS were determined by Tsui et al.[156] pK_as for CL were determined by Kates et al. (the authors determined pK_{a2} for CL to be between 7.5 and 9.5, we use an estimate of 8.5).[157] The pK_a for PI was estimated to be 1.0 based on the pK_as of the other phosphate groups.

and phospholipids were used in the simulation then converted to percentages for further analysis; we present all data as percentages). These restrictions were selected to achieve a balance between generating a wider variety of compositions and running the program in a reasonable amount of time (i.e. several hours instead of several days). Less variation in the phospholipid composition was allowed because these molecules are thought to be less variable and have been experimentally determined in the mitochondrial outer membrane,[121-125] while the amino acid composition of the mitochondrial outer membrane is likely more variable as it depends on heterogeneity of the mitochondrial surface proteome. Next, the p*I* of each randomly-generated composition is found using the expression for p*I* derived below.

4.2.4. Expression for p*I*

To find the p*I* of each composition, we derived an expression similar to the expression derived by Rezwan et al. to calculate net charge as a function of pH.[120] This expression is in the general form

$$Z(\mathrm{pH}) = \sum n_x \alpha_x(\mathrm{pH}) \qquad \text{(Equation 4-1)}$$

where n_x is the number of each amino acid or phospholipid x in the composition of interest and α_x(pH) represents the respective electrical net charge taking into account pH-dependent dissociation of specific functional group of x. The expression and its derivation including relevant amino acids and phospholipids are shown in Appendix B (Equation B-1 through B-6). Equation B-6 is solved numerically by varying the pH between 3 and 11, and accepts a solution if $|Z(\mathrm{pH})| < 0.1$. This value was chosen to

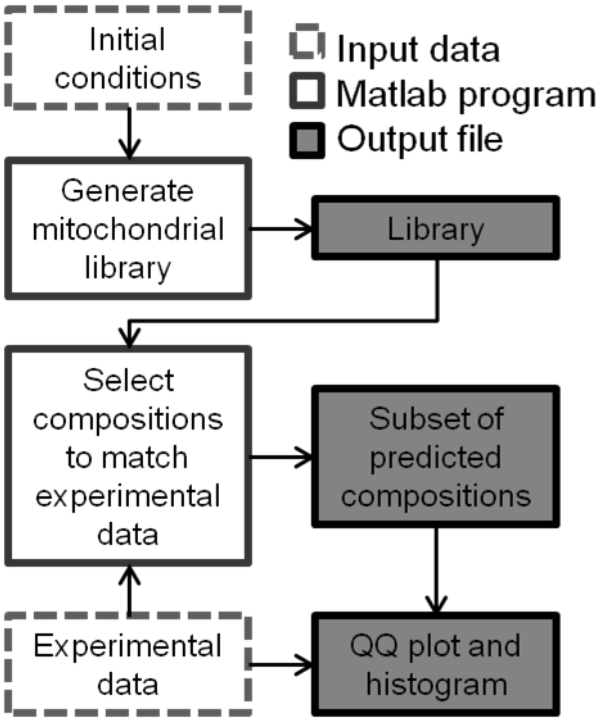

Figure 4-1. Flowchart of programs to generate mitochondrial library and match experimental data.

achieve a balance between accuracy and computation time, and results in calculation of p*I* values < 0.01 pH units of the "true" p*I* value for a given composition. For example, using the initial composition shown in Table 4-1, a $|Z(\text{pH})| < 0.1$ corresponds to pH values ranging between 4.78596 and 4.78617, (i.e., 0.00021 pH units). The program may be run as long as necessary to generate a library of sufficient size; to generate a library of ~2 million p*I*s with their corresponding compositions, the program was run for 1.5 hours on four 3.0 GHz dual-core processors. The library is available upon request.

4.2.5. Comparison to Experimental Data

After the library was generated, a subset of simulated compositions was selected to match an experimentally determined mitochondrial p*I* distribution. This experimental

data was obtained by cIEF as previously described from a mitochondrial sample consisting of intact mitochondria isolated by differential centrifugation from cultured rat myoblast cells.[154] To select compositions matching the experimental data, the experimental p*I*s of individual mitochondria were represented as a histogram distribution. The bins of this distribution guided a Monte Carlo-based selection of ~ 2000 compositions from the library so that the p*I* distribution of selected compositions matched the experimental p*I* distribution. In total, about two thousand compositions were selected from the library with the frequency of selections of compositions in each bin corresponding to the experimental data.

4.3. Results and Discussion

4.3.1. Validation of Simulation

To validate the method, we compared collections of simulated compositions of a given p*I* to the amino acid compositions of known mitochondrial outer membrane proteins with the same p*I*. Comparison of the average composition of the collection of simulated compositions with the true composition of the test protein determined the suitability of the method to predict protein compositions.

We selected 73 known mitochondrial outer membrane proteins from *Rattus norvegicus* as the test proteins. See Appendix B (Table B-4) for the complete list of proteins and their p*I*s. We calculated a p*I* for each protein using the amino acid sequences and Equation B-6 in Appendix B (modified to exclude phospholipids). Then, we modified the program to generate compositions with amino acids only. As the program

generated compositions, only those compositions with p*I* within 0.02 pH units from the calculated p*I*s of the mitochondrial outer membrane proteins were kept (we selected this range to approximate the resolving power of a typical cIEF experiment). This approach differs from the approach used for the generation of the mitochondrial library (i.e. instead of generating a set of compositions with a wide range of p*I*s, only compositions with p*I*s matching the proteins were generated). We used the program to generate more than 5,000 and up to 150,000 compositions for each of 69 mitochondrial outer membrane proteins, the remaining four proteins had p*I*s that were too high (p*I* 9.64 and above) for compositions to be generated. We then compared the average percent of each amino acid in the generated compositions to the actual percent of that amino acid in the known protein (for plots of these comparisons, see Figure B-1 in Appendix B). As expected, the percentages of the acidic (asp, glu) and basic (lys, arg) amino acids depend more strongly on p*I* than the percentages of the other amino acids. This comparison to known sequences is demonstrated in Figure 4-2, in which the average difference in percent composition from the known amino acid composition of each sequence is plotted against the p*I* of the known sequence. In these plots, many of the data points fall within one standard deviation of zero, and the majority of compositions differ by less than 10% for each amino acid. Smaller proteins may lack a certain type of amino acid completely or have p*I*s outside the range which the model can produce (since the initial conditions and restrictions of the model dictate a minimum percentage of the acidic and basic amino acids). For instance, the protein connexin 43 (Q6Q6S2, IPI00231746) was identified as

an outer mitochondrial membrane protein with calculated p*I* of 9.52. This protein has a sequence of only 29 amino acids, six of which are ionizable amino acids. While the simulation could generate compositions with a p*I* of 9.52, these compositions were not a good match for the six ionizable amino acids found in connexin 43. Despite limitations with small proteins, the model is overall adequate to predict amino acid compositions of known mitochondrial proteins with ~ 10% precision.

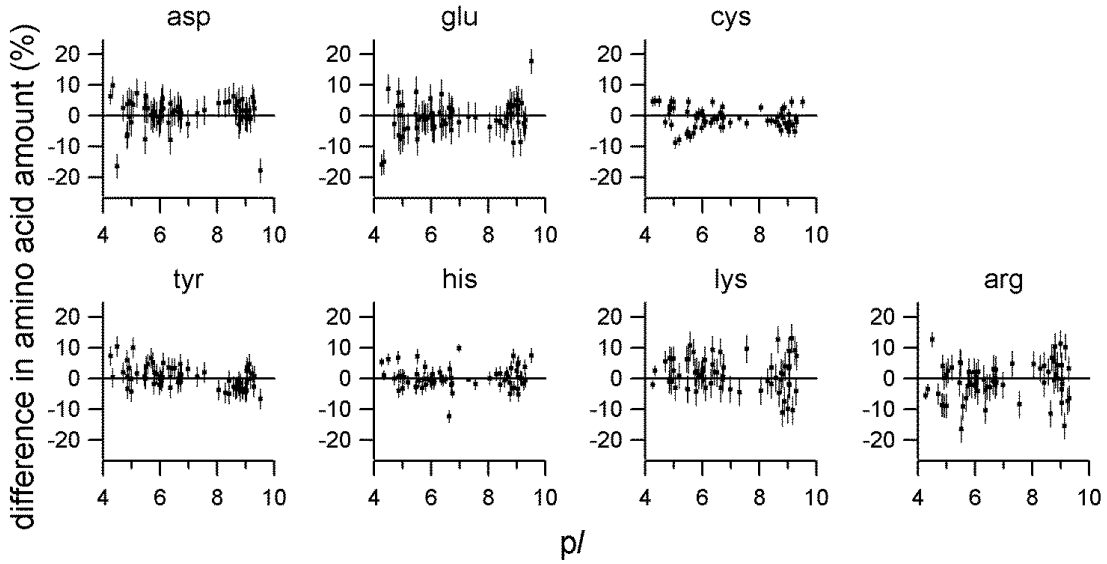

Figure 4-2. Comparison of predicted compositions to known compositions of mitochondrial outer membrane proteins. Deviation in average amino acid percentage in the predicted compositions (with similar p*I* of ± 0.02) from the actual composition of known mitochondrial outer membrane proteins plotted against p*I*. Error bars are plus/minus one standard deviation of the average difference from the known composition.

4.3.2. Distribution of Amino Acids and Phospholipids in the Library of Compositions

The ideal library must include compositions representing the abundance of all ionizable groups at each p*I*. By examining approximately two million randomly

generated compositions of the library through scatterplots of the percent of each amino acid or phospholipid versus p*I*, it became apparent that all the generated compositions had p*I*s between 4 and 9, but were not uniformly distributed (Figure 4-3). Areas which appear darker in the plots contain more data points, representing more individual compositions with similar p*I*s. There were significantly more compositions with p*I* from 4 to 6 than from 6 to 9. This lack of uniformity depends on the initial percentage, pK_a, and restrictions on the allowable range of each amino acid or phospholipid. We arbitrarily restricted the variation in composition of each phospholipid and amino acid to 20% and 50%, respectively, as this reduced the computational time while maintaining compositions that are likely within the expected deviations of the typical compositions dictated by the "average protein" composition. Allowing for more variation would increase the ranges of individual amino acids and phospholipids in the compositions, and slightly increase the range of generated p*I*s, but the general trends would likely remain the same. Predictably, compositions with higher p*I*s tend to have higher percentages of basic amino acids such as lys and arg, and compositions with lower p*I*s tend to have higher percentages of acidic amino acids such as glu and asp. Importantly, the arbitrarily set ranges for phospholipids and amino acids did not exclude less probable compositions (e.g. a composition with p*I* of 9 but a relatively low percentage of one basic amino acid such as lys, these compositions are located in areas of the plots which appear lighter) from the library. Generally, compositions with a low p*I* had a broader range of each amino acid or phospholipid than compositions with a high p*I*.

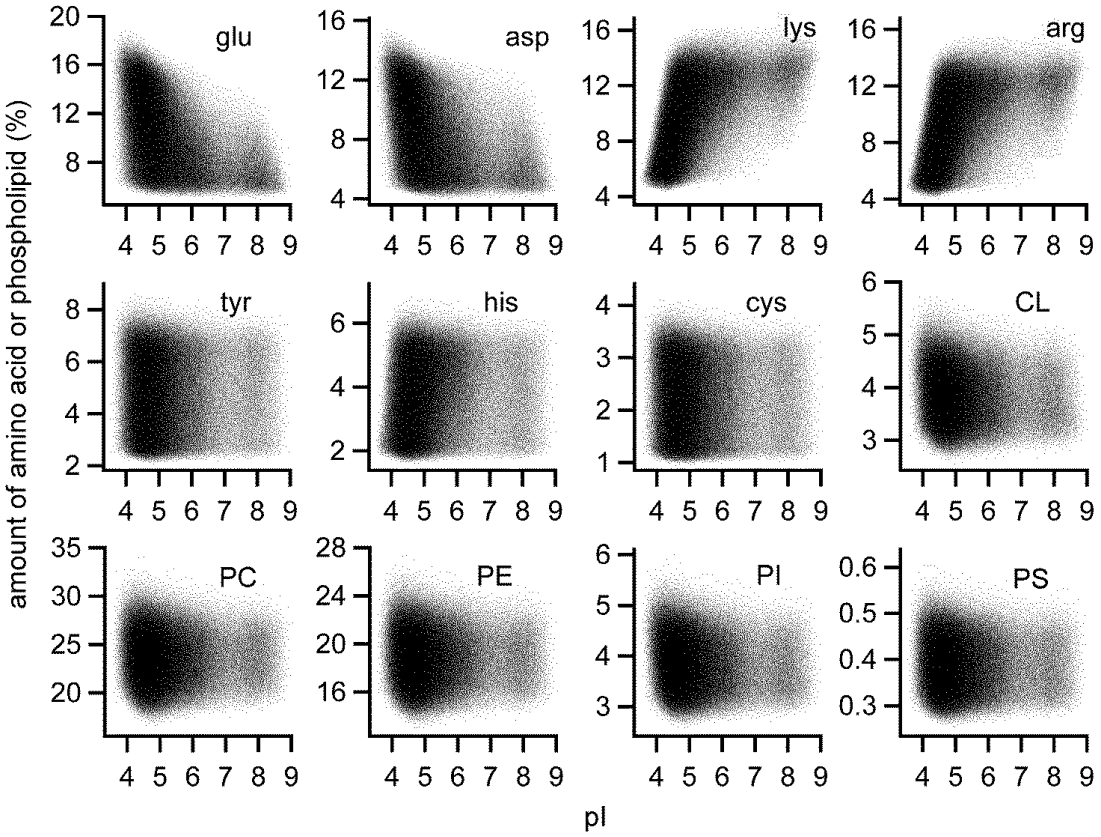

Figure 4-3. Trends in percentages of each amino acid or phospholipid vs. p*I* for all compositions in the library.

4.3.3. Comparison to an Experimental p*I* Distribution

To model an experimental p*I* distribution, we sampled the library to collect compositions associated with experimental p*I*s. We sampled a relatively small number of compositions (~ 2000 out of 2 million) to mirror a cIEF experiment in which a similar number of individual mitochondria are analyzed. Mitochondrial p*I* distributions, like many experimental results obtained from biological sources, are non-normal distributions and are therefore best evaluated by non-parametric statistical methods which preserve the

shape of the distribution. The experimental and predicted mitochondrial p*I* distributions are shown in Figure 4-4. The experimental distribution represents 121 individual mitochondria with p*I* from 4.66 to 6.83, and the predicted distribution represents 1998 compositions. The number of bins used to represent the distributions was selected based on the total number of individual mitochondria in the experimental data using a statistics formula which recommends a minimum bin number for representing nonparametric data.[158] While the experimental distribution in Figure 4-4A appears to be non-normal, we are able to match this distribution by selecting compositions from the library in a bin-by-bin fashion.

A quantile-quantile (Q-Q) plot is a graphical method to compare two non-normal distributions. Percentiles in increments of 5% from the 5^{th} to 95^{th} percentiles of each p*I* distribution were calculated, and then the percentiles from the predicted mitochondrial p*I* distribution were plotted against the percentiles from the experimental mitochondrial p*I* distribution (Figure 4-4B). Points in a Q-Q plot of identical distributions would all fall on a 45° line drawn from the origin; deviations from the line indicate differences in the distributions. We can also compare these distributions by calculating the sum of squares of the residuals (ss_{res}) of the quantiles in the Q-Q plot. For the Q-Q plot shown in Figure 4-4B, ss_{res} = 0.121. We find that our predicted distribution is as similar to the experimental distribution as replicate experimental cIEF measurements of the same mitochondrial sample (ss_{res} = 0.150).[154] Therefore, the collection of simulated

compositions selected to match the experimental data is an appropriate model for comparison.

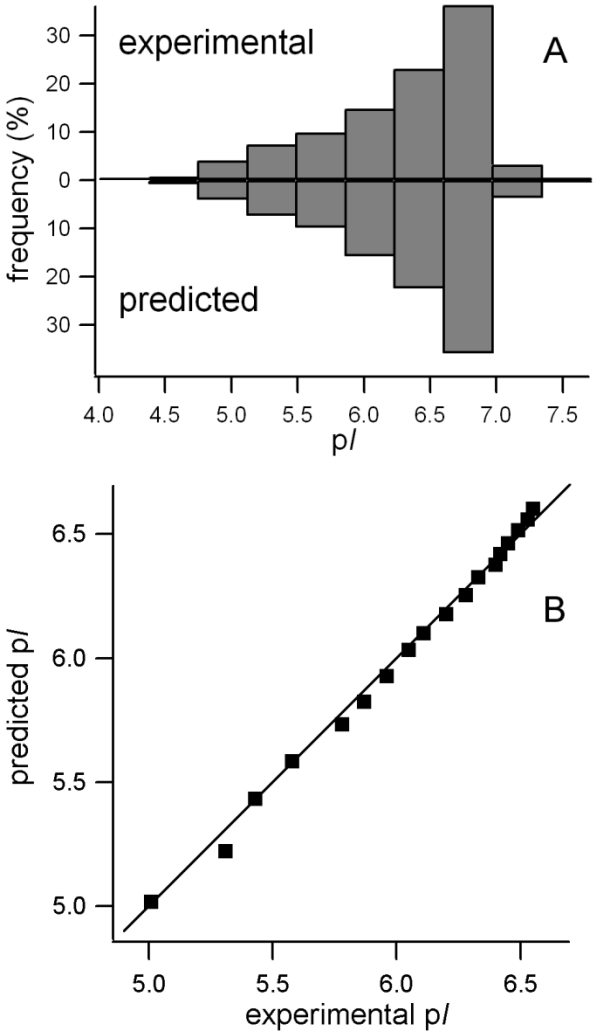

Figure 4-4. (A) Experimental and predicted mitochondrial isoelectric point distributions. (B) Q-Q plot comparison of predicted to experimental mitochondrial p*I* distributions.

4.3.4. Comparison of Compositions with Different p*I*

To demonstrate the utility of our method in describing the differences in sets of compositions for a given p*I*, we selected several p*I*s from different bins of the histogram in Figure 4-4A to compare. As a starting point, we selected a p*I* from the bin with the highest frequency of compositions (6.77), and compared it to a p*I* with the smallest difference typically resolvable by cIEF (6.75), a p*I* from the adjacent bin (6.41), and a p*I* from a distant bin (4.93). The average and standard deviation of the percentage of each amino acid or phospholipid in all compositions from the library within 0.01 pH units of each p*I* were then calculated (see Appendix B, Table B-5). The average difference in each amino acid or phospholipid from the composition with p*I* 6.77 is shown in Figure 4-5 (also see Appendix B, Table B-6). The largest differences in the compositions are in the acidic and basic amino acids between the compositions with the greatest difference in p*I*. However, significant differences are detected in some amino acids and phospholipids even between the two closest p*I*s (e.g. in glu or his). Since some differences are more pronounced than others, we distinguish between differences which are significant at the 95% confidence level ($p < 0.05$) and differences which are significant with greater than 99.9% confidence ($p < 0.001$). This method of comparison could be modified depending on the goal of the analysis; for instance, it might be useful to combine acidic amino acids such as asp and glu and basic amino acids such as lys and arg when comparing collections of compositions with larger differences in p*I* (i.e. 6.77 compared to 4.93) since these amino acids show similar trends. However, the differences in these amino

acids do not follow the same trends when comparing compositions with p*I* values which are closer together (i.e. 6.77 compared to 6.75 or 6.41). This type of analysis could also be used to determine amino acids or phospholipids that have a greater effect on p*I* over larger p*I* ranges (e.g. comparing compositions with p*I* 7.00 ± 1.00 to compositions with p*I* 6.00 ± 1.00). Overall, these results demonstrate the ability of the model to describe differences in composition between collections of individual compositions with different p*I*.

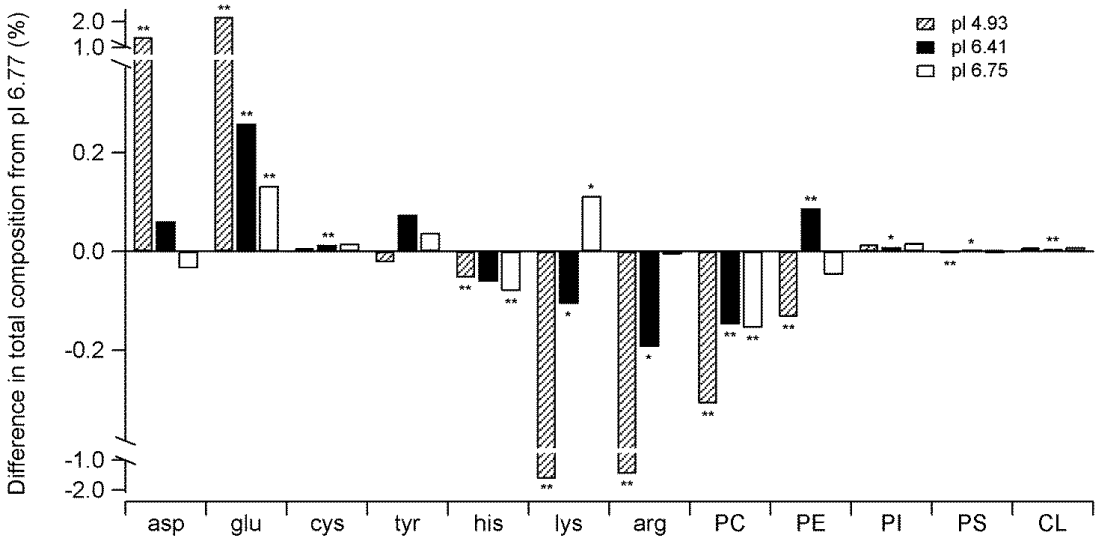

Figure 4-5. Comparison of compositions with p*I* 6.77 ± 0.01 to compositions with other p*I*s. Statistical significance was determined using t-tests (two-tailed, equal variance), * indicates $p < 0.05$; ** indicates $p < 0.001$.

4.3.5. Potential Applications of Model

This model provides a simulation of the mitochondrial outer membrane and the dependence of mitochondrial p*I* on the amino acid and phospholipid composition of the membrane, and allows an experimental p*I* distribution to be modeled. We can envision many potential applications and future refinements for this model. Post-translational modifications, damage to proteins or phospholipids, and changes in the relative amounts of specific proteins or phospholipids in the outer mitochondrial membrane are all biologically relevant processes which could be simulated with this model. The model could also be applied to other synthetic or biological particles.

Post-translational modifications to proteins in the mitochondrial outer membrane could result in a change in p*I* of the protein or mitochondrial composition. For example, phosphorylation of serine or threonine is a common post-translational modification involved in many protein signaling cascades that results in an addition of two negative charges to a protein; this modification would lower the p*I* of a mitochondrion. Future refinements in the model could be made to predict the effects of different extents of phosphorylation at specific sites. The effects of other post-translational modifications important in mitochondrial signaling such as ubiquitination could be predicted. Ubiquitination of outer mitochondrial membrane proteins is an important step in targeting damaged mitochondria for elimination by the cellular process of mitophagy.[128] This process is known to be affected in several disease states and changes in mitophagy are thought to be associated with aging.[13] Ubiquitination involves the addition of one or more

ubiquitin proteins to the side chain of lys, resulting in an increase in the number of ionizable amino acids but a net decrease in p*I* (ubiquitin has a p*I* of 6.56). Different p*I*s associated with ubiquitinylated compositions could be simulated, and this information could be used to design new experiments to analyze mitochondria marked for degradation by mitophagy.

This model could be extended to predict the effects of damage to proteins and phospholipids on mitochondrial p*I*. For instance, protein damage in the form of carbonylation of lys, arg, and his would result in changes to protein p*I*.[129] Protein carbonylation is thought to be caused by increased mitochondrial production of reactive oxygen species, and is associated with cancer, neurodegenerative disease, and other age-related diseases.[159] Our model could be used to produce compositions associated with mitochondrial outer membranes containing different degrees of carbonylated proteins.

This model could be used to predict the effect of over- or under-expression of proteins relative to phospholipids in the outer mitochondrial membrane. For example, we generated a new composition with a 10% reduction in its total protein percentage by reducing each amino acid by 10% of its initial value from the average composition for p*I* 6.77 and keeping the phospholipid percentages constant (see Table B-7 in Appendix B). The p*I* of this new composition is 6.30, a relatively large decrease of 0.47. A further extension of this idea is to predict the effect of underexpression of a known protein on the p*I* of a given composition. For example, the protein Fis1, with a p*I* of 8.88, is involved in mitochondrial fission, a process that affects mitochondrial morphology[160] and regulates

degradation of damaged mitochondria in the cell.[11] Mitochondria lacking the normal amount of this protein could be excluded from the turnover process and become dysfunctional. Assuming that Fis1 represents 1% of the total mitochondrial outer membrane proteins, we generated a new composition representing a 50% decrease of Fis1 from the average composition for p*I* 6.77 (see Table B-7 in Appendix B). This was done by reducing the percentage of each amino acid in the p*I* 6.77 composition by an amount proportional to the amount in which they are found in Fis1 (while keeping the percentages of phospholipids constant). The p*I* of this new composition is 6.73, a decrease of 0.04. While small, this p*I* difference could be resolved by cIEF. Using this approach, shifts in a mitochondrial p*I* distribution due to protein expression changes could be determined and used to design experiments or optimize separation conditions. Likewise, changes in p*I* due to changes in the phospholipid composition of the mitochondrial outer membrane could be predicted with this model. Since mitochondrial phospholipid composition directly affects many mitochondrial processes,[161] changes in phospholipid composition could represent biologically important processes or differences in mitochondrial function. For instance, translocation of oxidized cardiolipin to the outer mitochondrial membrane has been suggested to be involved in apoptosis.[162] The effect on p*I* of the increase in cardiolipin in the outer membrane could be predicted and used to design an experiment to study this process.

This method could also be adapted to other biological or synthetic particles such as cells, other organelles, or nanoparticles by changing the initial conditions involved in

the prediction. For instance, identification of microorganisms by cIEF is a promising technique for sensitive and selective characterization of different bacterial strains;[163] our method could be used to predict their surface compositions or to predict changes in their p*I*s upon modifications known to occur to their surface.

Our model could also be the basis to develop models for functional mitochondria that take into account their transmembrane potential, a factor that contributes to charge accumulation at the surface of biological membranes.[151,152] Experimental conditions conducive to support functional mitochondria during isoelectric focusing could make it possible to investigate individual mitochondrial membrane potentials by cIEF. This will make it possible to incorporate previous models of the dependence of electrophoretic mobility on membrane potential[164-166] and transmembrane pH gradients[80,82,167] into predictions of p*I* of individual functional mitochondria. This additional experimental work, combined with future refinements to our model, could shed light on such unknowns as the dependence of mitochondrial p*I* on the surface charge of the mitochondrial inner membrane and the effects of the isoelectric focusing technique itself on mitochondrial membrane potential.

4.4. Conclusions

We use a Monte Carlo method to produce individual compositions of the mitochondrial outer membrane with different percentages of amino acids and phospholipids to model the heterogeneity of mitochondrial p*I*. This method is able to match an experimentally-determined mitochondrial p*I* distribution and make predictions

about the individual compositions associated with experimental p*I*s. We validated the method by predicting the amino acid compositions of known mitochondrial outer membrane proteins. The model can be used to predict changes in p*I* upon changes to surface composition and enables many future potential applications.

Chapter 5.

Measurement of Individual Mitochondrial Membrane Potential by Capillary Electrophoresis

All data collection and analysis was performed by G. Wolken. Professor L. Thompson and her research group, primarily T. Graber, handled animal protocols and procedures.

Mitochondrial membrane potential is a highly heterogeneous component in cellular energy production which varies depending on energy demand, subcellular location, morphology, and functional status and is commonly used as an indicator of mitochondrial health or dysfunction. Since mitochondrial membrane potential is heterogeneous, methods for characterization of individual mitochondrial membrane potential and its relationship to other mitochondrial properties (e.g. surface properties such as electrophoretic mobility which relate to morphology and surface composition) are needed. Here we report on a method for the determination of individual mitochondrial membrane potential by capillary electrophoresis with laser-induced fluorescence detection (CE-LIF). Mitochondria were isolated from cultured cells, mouse muscle or liver, polarized, labeled with JC-1 (a ratiometric fluorescent probe which responds to changes in membrane potential), and separated with CE-LIF. Distributions of individual mitochondrial membrane potential and electrophoretic mobility were observed; these distributions were reproducible. Analysis of specific polarized and depolarized regions of interest allowed for the examination of membrane potential and comparison of electrophoretic mobility distributions even in preparations containing depolarized mitochondria. Through comparison of these regions of interest, dependence of electrophoretic mobility on membrane potential was observed, with higher membrane potential generally resulting in less negative electrophoretic mobility. This method could also be applied to further investigate the relationship between membrane potential and electrophoretic mobility and to characterize mitochondria from biological systems where

membrane potential heterogeneity is of interest such as cell or animal models of aging where increased heterogeneity may represent the presence of dysfunctional mitochondrial subpopulations.

5.1. Introduction

The mitochondrial membrane potential is an important property of mitochondria which is commonly used as an indication of function or dysfunction. Membrane potential arises from establishment of a proton gradient across the mitochondrial inner membrane by the enzymes of the electron transport chain, this proton gradient drives ATP production through oxidative phosphorylation. Changes in mitochondrial membrane potential result in changes in energy homeostasis and free radical production, and dysfunction in membrane potential is considered a factor in many mitochondrial-related diseases including cancer, diabetes, and Alzheimer's.[37] Moreover, changes in mitochondrial membrane potential affect turnover and regulation of dysfunctional mitochondria in the cell through fusion/fission[11] and targeting for elimination by mitophagy.[35]

Mitochondrial membrane potential within the cell is heterogeneous and varies depending on subcellular location, morphology, participation in the fusion/fission process, damage to mitochondria, and differences in mitochondrial structure. Additionally, sample preparation can affect the observed membrane potential. Different subcellular locations have different energy demands and mitochondrial membrane potential changes in response to these differences. In cultured astrocytes, mitochondria

near nuclei or the endoplasmic reticulum had lower and more uniform membrane potential than mitochondria in peripheral regions which had higher and more variable membrane potential.[19] This heterogeneity could also be due to the response of mitochondria to changes in local calcium concentration or cellular mechanisms to limit production of reactive oxygen species. Mitochondria in skeletal muscle fibers are classified as intermyofibrillar or subsarcolemmal based on their subcellular location. These subpopulations have different membrane potentials: subsarcolemmal mitochondria were previously reported to have higher membrane potential than intermyofibrillar mitochondria.[20] Upon depolarization, mitochondria undergo morphological changes, becoming more fragmented.[9] Mitochondrial morphology is controlled by the fusion/fission process; cells lacking the fusion proteins MFN1 and MFN2 had dysfunctional mitochondria and heterogeneity in membrane potential.[23] In a cell model of aging with impaired autophagy, subpopulations of mitochondria which did not exhibit noticeable fusion or fission, had larger and more varied sizes, and expressed lower levels of the fusion protein OPA1 had lower membrane potential.[168] Damaged mitochondria are eliminated from the cell by the process of mitophagy (mitochondrial-specific autophagy). In this process, damaged mitochondria with decreased membrane potential are marked for elimination through ubiquitination by the proteins PINK1 and Parkin, which accumulate at their surface.[24] It was demonstrated that only subpopulations of mitochondria with decreased membrane potential and not polarized, healthy mitochondria are marked for degradation through this mechanism.[22] In isolated mitochondria,

resistance to depolarization by carbonyl cyanide 4-(trifluoromethoxy)phenylhydrazone (FCCP) was observed in subpopulations of mitochondria with higher cardiolipin levels and higher membrane potential.[66] Adding another layer of complexity, the process of preparing samples of isolated mitochondria itself causes damage to mitochondria which may result in depolarization and additional apparent heterogeneity in membrane potential.[64]

Due to the heterogeneous nature of mitochondrial membrane potential, methods which can measure individual mitochondrial membrane potential are valuable for characterization of this heterogeneity and identification of subpopulations. While methods such as the measurement of TPP^+ uptake into mitochondria using an ion-selective electrode are able to give quantitative measurements of membrane potential in isolated mitochondria, they report only an average value.[50] Fluorescent dyes are commonly used in imaging, bulk fluorescence measurements, and flow cytometry to indicate mitochondrial membrane potential.[53] These dyes are cationic, which drives their uptake into mitochondria in a membrane potential-dependent manner according to the Nernst equation.[54] Some dyes are ratiometric, undergoing a spectral shift or transformation upon their uptake into mitochondria which can be measured and used to normalize their response across different dye concentrations or mitochondrial sizes.[55] JC-1 is one such ratiometric dye commonly used to measure mitochondrial membrane potential.[53,56] At low concentrations (less than approximately 100 nM), JC-1 exists primarily as a monomer and exhibits green fluorescence.[169] At higher concentrations, JC-

1 forms aggregates which exhibit red fluorescence. Mitochondrial membrane potential drives JC-1 uptake into mitochondria; polarized mitochondria with higher (more negative) membrane potential will accumulate JC-1 at a higher concentration than depolarized mitochondria. If a proper labeling concentration is chosen (i.e. low enough that minimal aggregation occurs outside mitochondria), these polarized mitochondria will therefore exhibit more red fluorescence from the JC-1 aggregates as well as green fluorescence from the monomeric form of the dye, whereas depolarized mitochondria will exhibit less red and primarily green fluorescence. Measurement of red/green fluorescence is then used as an indicator of membrane potential.

Capillary electrophoresis with laser-induced fluorescence detection (CE-LIF) is a separation technique which has been used for the characterization of mitochondrial heterogeneity. [86] Briefly, isolated mitochondria are labeled with a fluorescent probe or through expression of a fluorescent protein, introduced to a fused silica capillary in an aqueous buffer at physiological pH and osmolarity, and exposed to an electric field which causes them to migrate through the capillary. Fluorescence intensity and migration times of individual mitochondrial events are recorded, which reflect their content of the fluorescent probe and electrophoretic mobility, respectively. Depending on the selection of the fluorescent probe and interpretation of the observed electrophoretic mobility distributions, various mitochondrial properties such as DNA content,[170] cardiolipin levels,[87,171] the presence of a specific protein,[40] or the quality of a mitochondrial

preparation[62] may be assessed. The electrophoretic mobility of mitochondria depends on their surface charge density, which is reflective of their surface compositions.

Previous work has shown that the electrophoretic mobility of mitochondria also depends on membrane potential.[164,166,172] While this may be caused directly by changes in net charge at the mitochondrial surface due to depolarization,[166] modifications to their surface as a result of damage by increased production of reactive oxygen species (caused by an increase in membrane potential) or through increased ubiquitination through the PINK1/Parkin pathway (initiated by a decrease in membrane potential) could also affect their electrophoretic mobility. CE-LIF is capable of separating mitochondria based on differences in electrophoretic mobility, making it possible to study the relationship between mitochondrial surface compositions and membrane potential.

In this chapter, we introduce a method to measure mitochondrial membrane potential by CE-LIF. Mitochondria are isolated from cultured murine cells, liver, or muscle tissue, energized with succinate in the presence of rotenone (a complex I inhibitor), then labeled with JC-1. Valinomycin, a potassium ionophore which allows for free transport of potassium across the mitochondrial inner membrane, is used to depolarize mitochondria as a control.[173] Labeled mitochondria are then separated by CE and detected by a dual-laser excitation/dual-channel emission fluorescence detector. Measurement of red and green fluorescence from JC-1 allows for ratiometric measurement of individual mitochondrial membrane potential. Measurement of the electrophoretic mobility of individual mitochondria provides information about

mitochondrial surface charge density, which reflects the composition of the mitochondrial surface. Simultaneous measurement of membrane potential and corrected electrophoretic mobility allows for the investigation of the relationship between these properties. Through comparison of polarized and depolarized regions of interest, dependence of electrophoretic mobility on membrane potential was observed, with higher membrane potential generally resulting in less negative electrophoretic mobility. Since individual mitochondrial properties are characterized, this method is useful for investigating mitochondrial heterogeneity and assessment of membrane potential even if many mitochondria are damaged and depolarized during the preparation and separation.

5.2. Experimental

5.2.1. Reagents and Materials

Deionized water was purified using a Synergy filtration system (Millipore, Billerica, MA) and was used in preparation of all buffers and solutions. Sucrose, 4-(2-hydroxyethyl)piperazine-1-ethanesulfonic acid (HEPES), potassium hydroxide (KOH), sodium hydroxide (NaOH), 5,5′,6,6′-tetrachloro-1,1′,3,3′-tetraethyl-imidacarbocyanine iodide (JC-1), valinomycin, methanol, succinic acid, EGTA, potassium chloride (KCl), magnesium chloride ($MgCl_2$), tetraphenylphosphonium chloride (TPP^+), and polyvinyl alcohol (PVA, 99+% hydrolyzed, 89-98 kDa) were from Sigma-Aldrich (Saint Louis, MO). D-mannitol was from Riedel de-Haën (Seelze, Germany). 3-(N-morpholino)propanesulfonic acid (MOPS) was from Acros (Geel, Belgium). Fluorescein was from Molecular Probes (Eugene, OR). EDTA was from Avocado (Heysham,

Lancashire, UK). Tris was from Fisher (Fair Lawn, NJ). Rotenone was from ICN Biomedicals (Aurora, OH). 5-TAMRA was from AnaSpec (Fremont, CA). Bovine serum albumin (BSA) was from Roche (Indianapolis, IN). Hydrochloric acid (HCl) and dibasic potassium phosphate (K_2HPO_4) was from Mallinckrodt (Saint Louis, MO). Phosphate-buffered saline (PBS, 10×) was from Bio-Rad (Hercules, CA). Dulbecco's modified Eagle medium (DMEM), fetal bovine serum (FBS), and 0.5% trypsin (10×, 5 g/L trypsin, 2 g/L EDTA· 4Na, 8.5 g/L NaCl) were from Gibco (Invitrogen, Carlsbad, CA). Trypan blue stain (0.4%) was from Bio-Whittaker (Walkersville, MD). Fused-silica capillary tubing (50 μm i.d., 150 μm o.d.) was from Polymicro (Phoenix, AZ). The TPP^+ ion-selective electrode and Dri-Ref Ag/AgCl reference electrode were purchased from World Precision Instruments (Sarasota, FL).

5.2.2. Buffers and Solutions

Mitochondrial isolation buffer for cultured cells (buffer M) consisted of 210 mM mannitol, 70 mM sucrose, 10 mM HEPES, and 5.0 mM EDTA, adjusted to pH 7.4 with KOH. Mitochondrial isolation buffer for mouse liver tissue (buffer L) consisted of 10 mM tris, 10 mM MOPS, 1.0 mM EGTA, and 200 mM sucrose, adjusted to pH 7.4 with KOH. Mitochondrial isolation buffers 1 and 2 for mouse muscle tissue (buffers T_1 and T_2) consisted of 67 mM sucrose, 50 mM tris, 50 mM KCl, 10 mM EDTA, and 0.2% BSA and 250 mM sucrose, 10 mM tris, and 3.0 mM EGTA, adjusted to pH 7.4 with KOH. Respiration buffer (buffer R) consisted of 125 mM KCl, 10 mM HEPES, 5 mM $MgCl_2$, and 2 mM K_2HPO_4, adjusted to pH 7.4 with KOH. Sucrose-HEPES (buffer SH) buffer

consisted of 250 mM sucrose and 10 mM HEPES, adjusted to pH 7.4 with KOH, and was filtered to 0.2 μm before use. JC-1, fluorescein, and valinomycin were dissolved in methanol, aliquotted, dried in a vacuum evaporator (LabConco, Kansas City, MO), and stored at -20 °C. Stock solutions were prepared from a new aliquot for each experiment; JC-1 and valinomycin were reconstituted and diluted in DMSO and fluorescein was reconstituted in methanol and diluted with SH buffer. JC-1 stock solutions were sonicated for 60 minutes before further dilution. A stock succinate solution was prepared by titrating succinic acid to pH 7.4 with KOH in the presence of 10 mM HEPES. The succinate solution was filtered to 0.2 μm and stored at 4 °C. A stock rotenone solution was prepared in DMSO and stored at -20 °C. All buffers used for polarized mitochondria (buffers R and SH) contained 2.5 mM succinate and 2 μM rotenone with 2% DMSO, all buffers for depolarized mitochondria contained 2.5 mM succinate, 2 μM rotenone, and 2 μM valinomycin with 2% DMSO. The succinate concentration of 2.5 mM was chosen to limit Joule heating in the CE-LIF experiments; no detectable Joule heating was observed with this concentration of succinate in buffer SH while higher concentrations resulted in Joule heating. A standard solution of 10 mM TPP^+ was prepared in water and diluted with buffer R containing 2.5 mM succinate and 2% DMSO (and 2 μM valinomycin for analysis of depolarized mitochondria).

To reduce the fluorescence background for CE-LIF, SH buffer was photobleached using a lab-built device containing 120 blue light-emitting diodes (LEDs, Super Bright LEDs, Saint Louis, MO) (467 nm, 4.2×10^5 mcd intensity) for at least 24 hours before

use (see Figure C-1 in Appendix C). This strategy has been used to reduce the fluorescence background in capillary isoelectric focusing with LIF detection and in single molecule fluorescence experiments.[114,174]

5.2.3. Cell Culture

Adherent C2C12 mouse myoblast and L6 rat myoblast cells (ATCC, Manassas, VA) were cultured in vented 75 cm^2 flasks at 37 °C with 5% CO_2 in DMEM supplemented with 10% FBS. Cells were split after reaching 90% confluence by rinsing with PBS, releasing with 0.25% trypsin in PBS, and seeding back into the flask with fresh DMEM at splitting ratios between 1:20 and 1:40. L6 rat myoblast cells were used for initial experiments, and C2C12 mouse myoblast cells were used in later experiments for a more direct comparison to mouse tissue.

5.2.4. Fluorescence Microscopy

L6 Cells were seeded onto Lab-Tek chambered cover glass slides (ThermoFisher Scientific, Waltham, MA) overnight. Cells were labeled by adding 500 nM JC-1 to the media, 2 µM valinomycin was used as a control for depolarized mitochondria. After 30 minutes, the media was replaced with PBS and confocal fluorescence images were acquired using an Olympus IX-81 inverted fluorescence microscope (Melville, NY) equipped with a DS-IX100 disk spinning unit. A C9100-01 EM CCD camera (Hamamatsu, Bridgewater, NJ) was used to acquire images. Images were acquired in the red channel with a 2.0 s exposure time, a gain of 100, λ_{ex} = 545 ± 10 nm, λ_{em} = 597.5 ± 27.5 nm, and a 565 nm dichroic, (Olympus M-RFPHQ filter cube) and in the green

channel with a 10.0 s exposure time, a gain of 100, λ_{ex} = 470 ± 10 nm, λ_{em} = 517.5 ± 22.5 nm, and a 485 nm dichroic (Olympus U-MGFPHQ filter cube). Simple PCI software (Hamamatsu) was used to adjust contrast and apply a median smooth function to the images. See Figure C-2 in Appendix C for the unmodified images.

5.2.5. Mitochondrial Preparation and JC-1 Labeling

Mitochondria from cell culture were isolated by differential centrifugation and mechanical homogenization.[78] Cells were lifted with 0.25% trypsin in PBS and added to an equal volume of DMEM. All subsequent procedures were performed on ice or at 4 °C unless otherwise noted. Cells were washed three times with ice-cold buffer M and resuspended in 2 mL buffer M. Cells were counted with a Fuchs-Rosenthal counting chamber (Hausser Scientific, Horsham, PA) after staining with trypan blue. A typical cell concentration was 1×10^6 cells/mL. Cells were disrupted in a 2 mL Kontes glass dounce tissue grinder (Kimble Chase, Vineland, NJ) by applying strokes with loose (0.12 mm) and narrow (0.06 mm) glass pestles by hand until cell breakage from 80-100% was achieved, as monitored by trypan blue staining. After disruption, intact cells, nuclei, and other cellular debris were eliminated from the preparation by centrifugation at 600*g* for 10 min. Mitochondria in the supernatant were pelleted by centrifugation at 10000*g* for 10 min. Mitochondria were resuspended in buffer M and kept on ice. Protein content in the mitochondrial fraction was quantified using the Pierce BCA protein assay kit according to the manufacturer's instructions (Thermo, Rockford, IL). Typical mitochondrial protein concentration from this preparation was 1.60 ± 0.09 mg/mL.

Mitochondria were isolated from mouse liver and muscle tissue using a published protocol.[60] C57BL6 mice were housed in a central specific pathogen free facility and were treated in an optimally ethical and humane fashion using protocols approved by the Institutional Animal Care and Use Committee for all procedures. Briefly, a female mouse was anesthetized on the day of the experiment and the liver and hamstring muscle were excised. The liver was immersed in ice-cold buffer L and the muscle was immersed in ice-cold PBS containing 10 mM EDTA. All subsequent procedures were performed on ice or at 4 °C unless otherwise noted. For preparation of liver mitochondria, the liver was rinsed with buffer L and minced into small pieces. The pieces were rinsed and transferred to a glass 15 mL Potter-Elvehjem homogenizer (Wheaton, Millville, NJ). The liver was homogenized with 3-5 strokes of a motor-driven Teflon pestle operated at 1600 rpm (Wheaton). The homogenate was centrifuged at 600*g* for 10 min to remove nuclei, intact cells, and other debris. The supernatant was centrifuged at 7000*g* for 10 min, then the pellet was washed once with buffer L and centrifuged at 7000*g* for 10 min. The liver mitochondria were resuspended in a minimal amount of buffer L and kept on ice. For preparation of muscle mitochondria, the muscle was minced into small pieces which were then washed with PBS containing 10 mM EDTA. The minced muscle pieces were incubated with 0.05% trypsin in PBS with 10 mM EDTA for 30 min. The pieces were transferred to buffer T_1 and homogenized with 10-15 strokes of a motor-driven Teflon pestle operated at 1600 rpm The homogenate was centrifuged at 700*g* for 10 min to remove nuclei, intact cells, and other debris. The supernatant was centrifuged at 8000*g*

for 10 min, then the pellet was washed once with buffer T_2 and centrifuged at 8000*g* for 10 min. The muscle mitochondria were resuspended in a minimal amount of buffer T_2 and kept on ice. Protein content in each mitochondrial fraction was quantified using the Pierce BCA protein assay kit. Protein concentration from this preparation was 23 ± 5 mg/mL for liver mitochondria and 3.2 ± 0.6 mg/mL for muscle mitochondria.

Directly before CE-LIF measurements, aliquots from each isolated mitochondrial fraction (from cells or tissue) were centrifuged and resuspended in buffer R containing 2.5 mM succinate, 2 µM rotenone, 2% DMSO, and 2 µM valinomycin (for depolarized controls). The mitochondria were incubated in the dark for 10 min at 37 °C with 300 rpm mixing in an Eppendorf Thermomixer (Hamburg, Germany). JC-1 was then added to a final concentration of 1 µM, and the samples were incubated for an additional 10 min at 37 °C. Mitochondria were then kept at room temperature in the dark and analyzed by CE-LIF or in the plate reader. For subsequent CE-LIF runs, new aliquots from the original mitochondrial fraction were centrifuged, resuspended in buffer R with succinate, rotenone, and valinomycin (for depolarized controls), and labeled with JC-1 directly before analysis. This procedure prevents loss of JC-1 over time due to consumption of substrate or mitochondrial degradation resulting in loss of membrane potential (see Figure C-3 in Appendix C).[53]

5.2.6. Bulk Measurement

Bulk red and green fluorescence from mitochondrial samples labeled with JC-1 was measured with a BioTek Synergy 2 well plate reader (Winooski, VT) in 96-well

plates (Nunc, Roskilde, Denmark). Red (λ_{ex} = 530 ± 12.5 nm, λ_{em} = 590 ± 17.5 nm) and green (λ_{ex} = 485 ± 10 nm, λ_{em} = 528 ± 10 nm) fluorescence was acquired using auto sensitivity mode, and red/green ratios were calculated to indicate mitochondrial membrane potential. Controls (buffer R and buffer R containing JC-1 at the same concentration used for labeling mitochondria) were included (see Figure C-4 in Appendix C).

5.2.7. Membrane Potential Measurement with TPP^+ Ion-Selective Electrode

Measurement of the average membrane potential of isolated mitochondria was performed by a method which has been described previously.[50] Briefly, mitochondria were isolated from L6 rat myoblasts, then polarized and depolarized fractions were prepared as described above without JC-1 labeling. Total mitochondrial protein content was measured using the BCA assay as described above and TPP^+ uptake was measured by an ion-selective electrode. The response of the electrode to TPP^+ was calibrated by 7 µL additions of 0.1 mM TPP^+ to 700 µL of buffer R with 2.5 mM succinate and 2% DMSO (also containing 2 µM valinomycin for analysis of depolarized mitochondria) with stirring. Directly after addition of TPP^+ to a final concentration of 3.85 µM, 75 µL mitochondrial suspensions containing 0.30 mg (polarized sample) and 0.32 mg (depolarized sample) of total mitochondrial protein in the above buffer were added. Electrode response was recorded using an Orion 420 A+ pH meter (Thermo) and collected using a program written in LabView (National Instruments, Austin, TX). Membrane potential was calculated according to the previously described method.[50]

5.2.8. Instrument Description

A home-built capillary electrophoresis instrument which has been described previously[141] has been adapted for this work. For more efficient excitation of JC-1, a 5 mW HeNe laser (Melles-Griot, Carlsbad CA) was added to the instrument. The 543.5 nm light from this laser was combined with the 488 nm light from a 12 mW Ar^+ laser (Melles-Griot, Carlsbad, CA) using a 503 nm dichroic beam combiner (Semrock LM01-503-25, Rochester, NY) and was focused through the sheath-flow cuvette for post-capillary detection. Light was collected at 90° to the lasers by a 40×, 0.55 NA objective (New Focus, San Jose, CA). Scattered laser light was eliminated with a 488/543 nm dual notch filter (NF01-488/543-25, Semrock). Fluorescence was passed through a pinhole, split into red and green channels using a 540 nm longpass dichroic mirror (XF2013, Omega Optical, Brattleboro, VT), and passed through a 593 ± 20 nm (red channel) or 520 ± 17.5 nm (green channel) band-pass filter (BrightLine Fluorescence Emitter, Semrock) onto photomultiplier tubes (PMT, R1477, Hamamatsu) biased at 1000 V.

5.2.9. Capillary Preparation

Fused-silica capillaries were permanently coated with adsorbed PVA by a method adapted from Shen et al.[105] PVA coatings reduce mitochondrial adsorption to the capillary surface.[104] Briefly, three capillaries were rinsed with methanol, 1.0 M NaOH, and water for 10 min each by flushing under 10 psi nitrogen pressure. The capillaries were purged and flushed with a 5% (w/v) PVA solution for 1 h. The PVA solution was heated to 80 °C prior to flushing through the capillaries. The solution was then purged

from the capillaries. After purging, the capillaries were heated between two aluminum plates with heating tape applied to one side; temperature was controlled by a variable-voltage power source at 140 °C for 1 h. The PVA flush, N_2 purge, and heating steps were repeated once with the capillaries in the opposite orientation for a more robust coating. Capillaries were stored dry until use. Before use, the inlet and outlet were trimmed and the polyimide coating was burned off at the tips to produce capillaries with a total length of ~40 cm.

The PVA-coated capillary was installed in the instrument and initially aligned by flushing a solution of 5×10^{-9} M fluorescein and 5×10^{-8} M 5-TAMRA in SH buffer by application of pressure to the inlet. These two fluorophores were selected as they are compatible with the dual-laser excitation/dual channel fluorescence emission detection system (fluorescein is excited by the 488 nm laser and detected in the green channel, 5-TAMRA is excited by the 543.5 nm laser and detected in the red channel).

For fine alignment of the capillary, a solution of 2.5 µm Alignflow flow cytometry beads for 488 nm excitation (Invitrogen) in SH buffer was continuously injected by application of an electric field of -400 V/cm with the PMTs biased at 300V. Alignment was considered acceptable when the relative standard deviation of the average fluorescence intensity from each bead event in the red channel was less than 20% (see Figure C-5 in Appendix C).

5.2.10. CE Procedure

After the capillary was aligned, it was rinsed with SH buffer containing 2.5 mM succinate, 2 µM rotenone, and 2% DMSO directly before CE-LIF runs of polarized samples, and the same buffer with 2 µM valinomycin before runs of depolarized samples. A mitochondrial suspension to be analyzed by CE-LIF was diluted with this buffer and fluorescein was added to a final concentration of 5×10^{-10} M. Fluorescein was used as an internal standard to calculate the limit of detection and electroosmotic flow (EOF). Typical mitochondrial protein content of injected samples, as determined by the BCA protein assay (above), was 1.5 ng for liver mitochondria, 1.0 ng for muscle mitochondria, and 0.25 ng for mitochondria from cultured cells, although it was necessary to use trial and error to find a dilution factor that resulted in an acceptable number of mitochondrial events (see Data Analysis section below on peak overlap). Samples were injected hydrodynamically by siphoning; an electronically actuated valve (Parker Hannifin, Cleveland, OH) was used to increase the height difference between the inlet of the capillary and the sheath flow waste to 110 cm for 2.7 seconds. After injection, the inlet of the capillary was rinsed twice in SH buffer and switched to the vial of running buffer (as above, SH buffer containing succinate, rotenone, DMSO, and valinomycin if sample was depolarized). An electric field of -400 V/cm was applied for 15 min for the CE separation. Between runs, the capillary was rinsed with DMSO for 5 min and fresh running buffer for 5 min The peak height and migration time of fluorescein were used to calculate the limit of detection and EOF. For a typical experiment, the limit of detection (S/N = 3) was 26 ± 1 zmol and the EOF was $9.4 \pm 0.1 \times 10^{-5}$ cm^2 V^{-1} s^{-1} (n = 7). This

reduction in EOF from a previously reported value for uncoated fused silica of 5.1 ± 0.1 × 10^{-4} cm^2 V^{-1} s^{-1} indicates a successful PVA coating.[154]

5.2.11. Data Analysis

Data from the PMTs was acquired at 200 Hz, digitized by an I/O data acquisition card (PCIMIO-16E-50) operated by Labview 5.1 software (National Instruments), and stored as a binary file. Data were analyzed in Igor Pro software (Wavemetrics, Lake Oswego, OR) by a procedure written in-house which has been described previously, PeakPicks.[101] Briefly, electropherograms were median filtered to separate narrow spikes (peaks with baseline widths smaller than 200 data points or 1.0 s) from broad peaks (fluorescein). Spikes with signal intensity above a threshold of 5 standard deviations over the background signal were assigned to mitochondrial events. Coincident events (events with maxima in both red and green channels at the same migration time, with a tolerance of 0.01 s) were then selected. The electrophoretic mobility and corrected electrophoretic mobility (electrophoretic mobility minus the mobility of the EOF) was calculated for each mitochondrial event based on its migration time.

In addition to mitochondrial events, some of these events may correspond to false positives. A particular concern is the detection of free JC-1 aggregates. Although free JC-1 should migrate in the opposite direction of the detector due to its positive charge (so no free JC-1 aggregates should be detected), a blank injection was performed to measure the false positive rate. A 200 nM solution of JC-1 was injected and the number of detected coincident events was compared to the average number of events detected in four

injections of mitochondria from liver tissue (see Figure C-6 in Appendix C). This concentration of JC-1 was chosen to match the concentration that is present in the mitochondrial samples after dilution with buffer SH for injection. The number of false positives detected was calculated as less than 5% of the total number of detected coincident mitochondrial events.

An issue in individual organelle analysis by CE is whether peak overlap is a problem, i.e., whether most observed peaks represent individual or multiple comigrating components. Statistical overlap theory has been applied to this problem to determine a threshold for peak saturation, below which the number of observed events is a good estimate for the number of actual events, and so the effect of peak overlap on the observed distribution is minimal.[142,175] This statistical test has been applied to each mitochondrial CE-LIF run and it has been determined that peak overlap is not a significant problem (see Table C-1 in Appendix C).

Polarized and depolarized regions of interest (ROIs) were defined in each CE-LIF experiment. A similar graphical approach has been used previously to define groups of polystyrene microspheres with distinct fluorescence and scattering properties analyzed by CE-LIF.[176] First, red vs. green fluorescence intensities of each coincident event were plotted for polarized and depolarized samples of each type (cells, muscle, and liver). A line drawn from the origin was used to divide the data into polarized and depolarized ROIs (i.e. with the polarized ROI located above the line and the depolarized ROI below it). To verify that a linear definition of ROIs is valid, various least-squares fits (e.g.

linear, polynomial, exponential) were performed on the data; the non-linear fits were not significantly better than the linear fit (see Table C-2 in Appendix C). The slope of the line was then varied to maximize the difference between the percentage of events from polarized and depolarized samples falling in the polarized ROI (see Figure C-10 in Appendix C). Results of this ROI analysis are shown in Table C-3 in Appendix C and discussed in section 5.3.3.

5.3. Results and Discussion

5.3.1. Validation of JC-1 as Membrane Potential Indicator

JC-1 is commonly used as an indicator of mitochondrial membrane potential in intact cells and isolated mitochondria.[56,169,177] We confirmed that this dye responds to changes in mitochondrial membrane potential in L6 rat myoblasts by observation of polarized cells and depolarized cells (2 μM valinomycin) with confocal fluorescence microscopy (see Figure 5-1 A-D). Indeed, polarized cells exhibit intense red fluorescence from JC-1 aggregates, and depolarized cells exhibit very weak red fluorescence and more intense green fluorescence from JC-1 monomers. While imaging is a useful technique for observing mitochondrial membrane potential heterogeneity and provides the advantage of observations of mitochondrial morphology,[19] this technique is not suitable for measurement of mitochondrial electrophoretic mobility, which can provide additional information about subpopulations of mitochondria with different surface properties. Additionally, without automation of image collection and data analysis, characterization of large numbers of mitochondria is time-consuming.

JC-1 fluorescence in polarized and depolarized mitochondria isolated from cultured L6 rat myoblasts, C2C12 mouse myoblasts, and mouse liver and muscle tissue was observed in bulk using a well plate reader. Similar results were obtained in isolated mitochondria from all sources (i.e. polarized mitochondria exhibit more intense red fluorescence and higher red/green ratios, see Figure 5-1 E). This technique has the advantage of simplicity and is therefore useful as a general assessment of the mitochondrial membrane potential of a preparation of cells or isolated mitochondria, but reports only an average value of relative membrane potential and is not suitable for analysis of heterogeneity or subpopulations.

Membrane potential of isolated mitochondria from cultured L6 rat myoblasts was calculated by measuring uptake of TPP^+ by polarized (Figure 5-1 F) and depolarized (Figure 5-1 G) samples using an ion-selective electrode. Membrane potential was calculated as -125 mV and -80 mV for polarized and depolarized samples, respectively. These values are comparable to values previously determined by this technique: mitochondria isolated from rat liver and energized with succinate were reported to have a membrane potential of -172 mV, which dropped to around -110 mV (value estimated from the data shown in this report) upon depolarization with FCCP.[50] While a clear advantage of this technique is the ability to calculate actual values of membrane potential, it is not suitable for analysis of individual mitochondria or subpopulations and reports an average value.

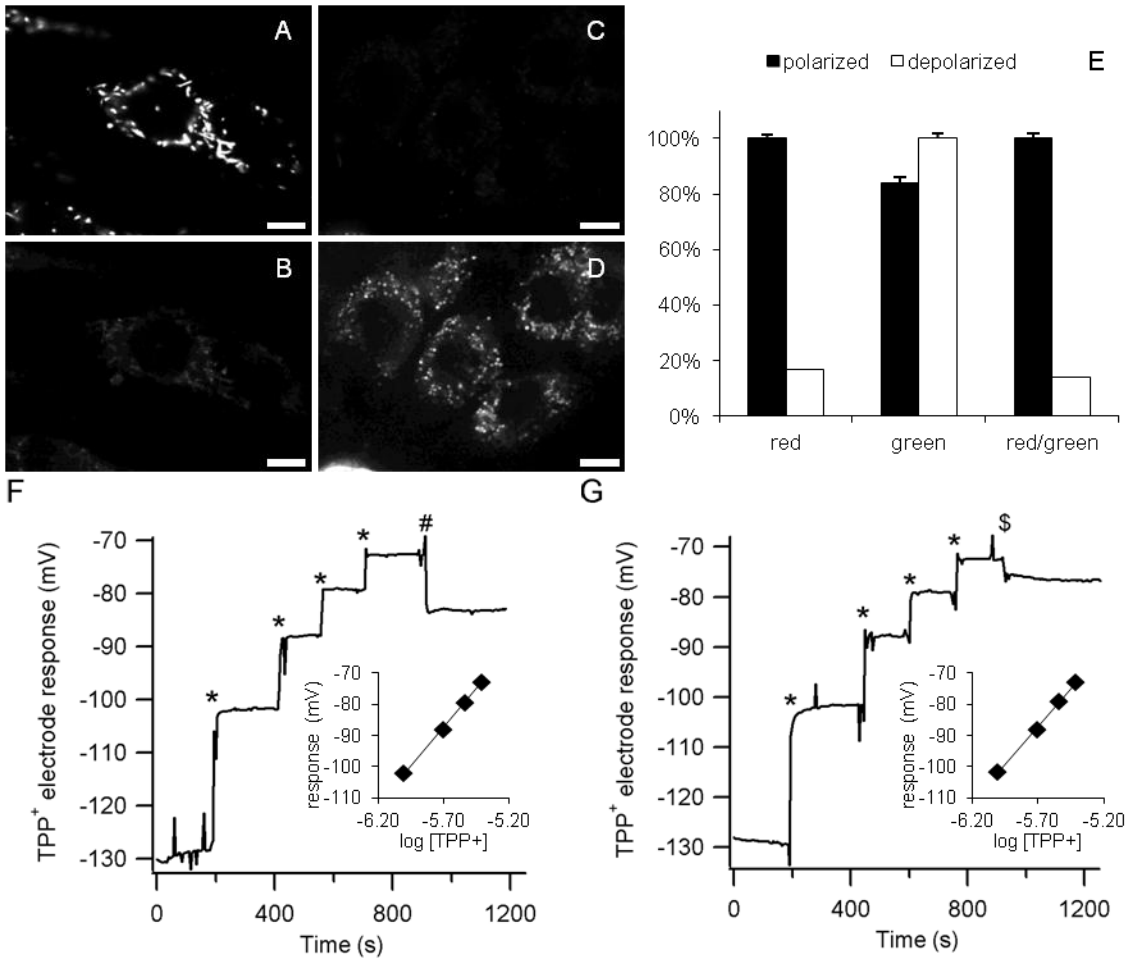

Figure 5-1. Validation of JC-1 as ratiometric probe for membrane potential. A-D) Confocal fluorescence microscopy images of polarized (A and B) and depolarized (C and D) L6 rat myoblast cells labeled with 500 nM JC-1 for 30 minutes. Polarized cells exhibit intense red fluorescence (A) from JC-1 aggregates and less intense green fluorescence (B); depolarized cells (2 µM valinomycin) exhibit very little red fluorescence (C) and more intense green fluorescence (D) from JC-1 monomers. Contrast is adjusted and median smooth function used. Scale bars are 10 µm. Red channel (A and C): 2.0 s exposure time, gain of 100, λ_{ex} = 545 ± 10 nm, λ_{em} = 597.5 ± 27.5 nm, 565 nm dichroic, Olympus M-RFPHQ filter cube; green channel (B and D): 10.0 s exposure time, gain of 100, λ_{ex} = 470 ± 10 nm, λ_{em} = 517.5 ± 22.5 nm, 485 nm dichroic, Olympus U-MGFPHQ filter cube. E) Bulk measurement of normalized red (λ_{ex} = 530 ± 12.5 nm, λ_{em} = 590 ± 17.5 nm) and green (λ_{ex} = 485 ± 10 nm, λ_{em} = 528 ± 10 nm) fluorescence from isolated mitochondria (L6 rat myoblasts) labeled with 100 nM JC-1. Depolarized (2 µM valinomycin) mitochondria show a reduced red/green ratio when compared to polarized mitochondria. Error bars represent the standard deviation of measurements from three different wells containing the same

(continued from previous page) sample. F-G) Measurement of membrane potential by TPP^+ ion-selective electrode in polarized (F) and depolarized (G, 2 µM valinomycin) mitochondria isolated from L6 rat myoblasts. The * symbols represent additions of 7 µL of 0.1 mM TPP^+ to 700 µL of buffer R with 2.5 mM succinate and 2% DMSO, # and $ represent additions of 75 µL suspensions of polarized and depolarized mitochondria in the same buffer, respectively. Total mitochondrial protein added was 0.30 (polarized sample) and 0.32 mg (depolarized sample). Membrane potential was calculated as -125 mV and -80 mV for polarized and depolarized samples, respectively.

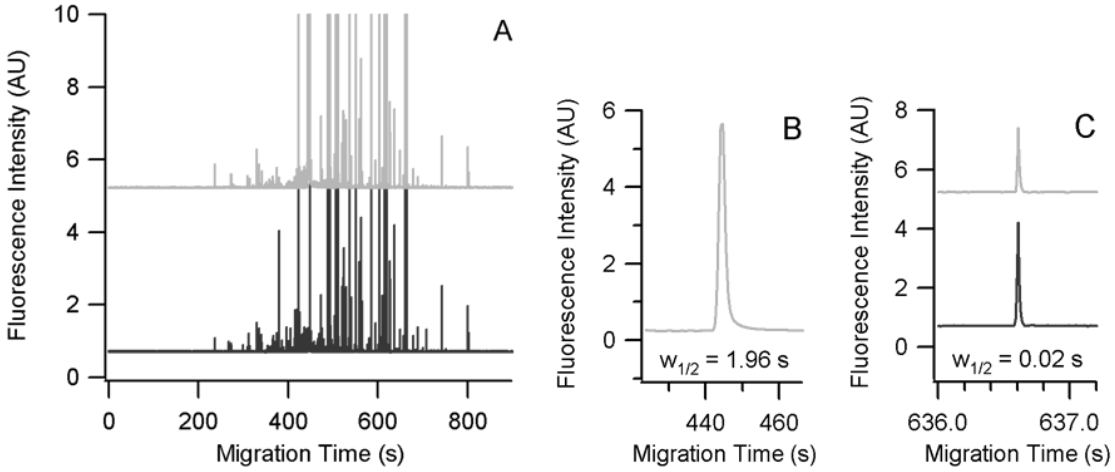

Figure 5-2. CE-LIF trace of JC-1 labeled mitochondria from muscle tissue. A) Electropherograms, bottom and top traces show JC-1 fluorescence in red (593 ± 20 nm) and green (520 ± 17.5 nm) channels, respectively. Y-offset is +5 for green channel. B) Fluorescein peak in green channel after median filtering to separate spikes from wide peaks. C) Mitochondrial event in red and green channels. Y-offset is +5 for green channel. Samples were hydrodynamically injected by creating a height difference of 110 cm between inlet and outlet for 2.7 s. Separations were performed in a 50 µm i.d. fused silica capillary coated with PVA at -400 V/cm in buffer SH with 2.5 mM succinate, 2 µM rotenone, and 2% DMSO; 2 µM valinomycin was added for CE-LIF runs of depolarized mitochondria.

Individual mitochondrial events were detected in CE-LIF separations (see Figure 5-2). Red and green fluorescence from mitochondria labeled with JC-1 was observed using this technique, similar to the results obtained in microscopy and bulk fluorescence methods. This technique allows for the observation of distributions of red/green ratios and corrected electrophoretic mobilities of individual mitochondria.

5.3.2. Reproducibility

The reproducibility of this technique was evaluated by performing three replicate injections of polarized mitochondria and three replicate injections of depolarized mitochondria isolated from C2C12 mouse myoblasts. In all CE-LIF runs, distributions of red/green ratio and corrected electrophoretic mobility were observed. Data from individual runs (see Figure C-7 in Appendix C) are combined to show overall distributions of red/green ratio (Figure 5-3 A) and corrected electrophoretic mobility (Figure 5-3 C). Individual and combined distributions from depolarized runs are shown in Figures C-8 and C-9 in Appendix C.

Overall, the distributions of red/green ratios and corrected electrophoretic mobility were reproducible. This is demonstrated by comparisons using quantile-quantile (Q-Q) plots, which have been used to compare mitochondrial migration time distributions in CE.[145] In this approach, the 5^{th} through 95^{th} percentiles of two data sets are plotted against one another; identical distributions would produce plots with points that fall on a line defined by $y = x$. Q-Q plots can be used to evaluate reproducibility by plotting data from an individual run against the data from all runs combined. The normalized sum of

squares of residuals (ss_{res}) can be determined for a more quantitative comparison of the distributions shown in a Q-Q plot. This value is calculated according to the following equation, where the median is taken from the data plotted on the *x*-axis of the Q-Q plot and the ss_{res} is calculated as reported previously.[154]

$$\text{normalized } ss_{res} = \frac{\sqrt{ss_{res}}}{median} \times 100\% \qquad \text{(Equation 5-1)}$$

The normalized ss_{res} is similar to the relative standard deviation of a data set, and larger values indicate less similar distributions. Values for ss_{res} and normalized ss_{res} are provided for all Q-Q plots (see Table C-4 in Appendix C). Distributions of red/green ratio (Figure 5-3 A) and corrected electrophoretic mobility (Figure 5-3 C) were consistent from run to run; the Q-Q plots show data points from individual runs falling close to the line. There is much more run-to-run variation in the 90-95th percentiles of the red/green ratios (normalized ss_{res} = 352%, 221%, and 370% for runs 1, 2, and 3, respectively, inset in Q-Q plot in Figure 5-3 B), but the 5-85th percentiles are reproducible (normalized ss_{res} = 26%, 18%, and 13% for runs 1, 2, and 3, respectively). For the 5-85th percentiles, the normalized ss_{res} is very low compared to the value for the 90-95th percentiles. This result represents the presence of a small number of events with very high red/green ratios and wider variation in these ratios. Distributions of corrected electrophoretic mobility are reproducible, with normalized ss_{res} = 7%, 7%, and 5% for runs 1, 2, and 3, respectively. For ROIs from individual runs of polarized and depolarized samples, distributions of red/green ratio and corrected electrophoretic mobility were almost as reproducible, with slightly more scatter away from the line (see Figure C-12 in Appendix C), this likely

represents an effect of the smaller number of events in ROIs as compared to the overall data.

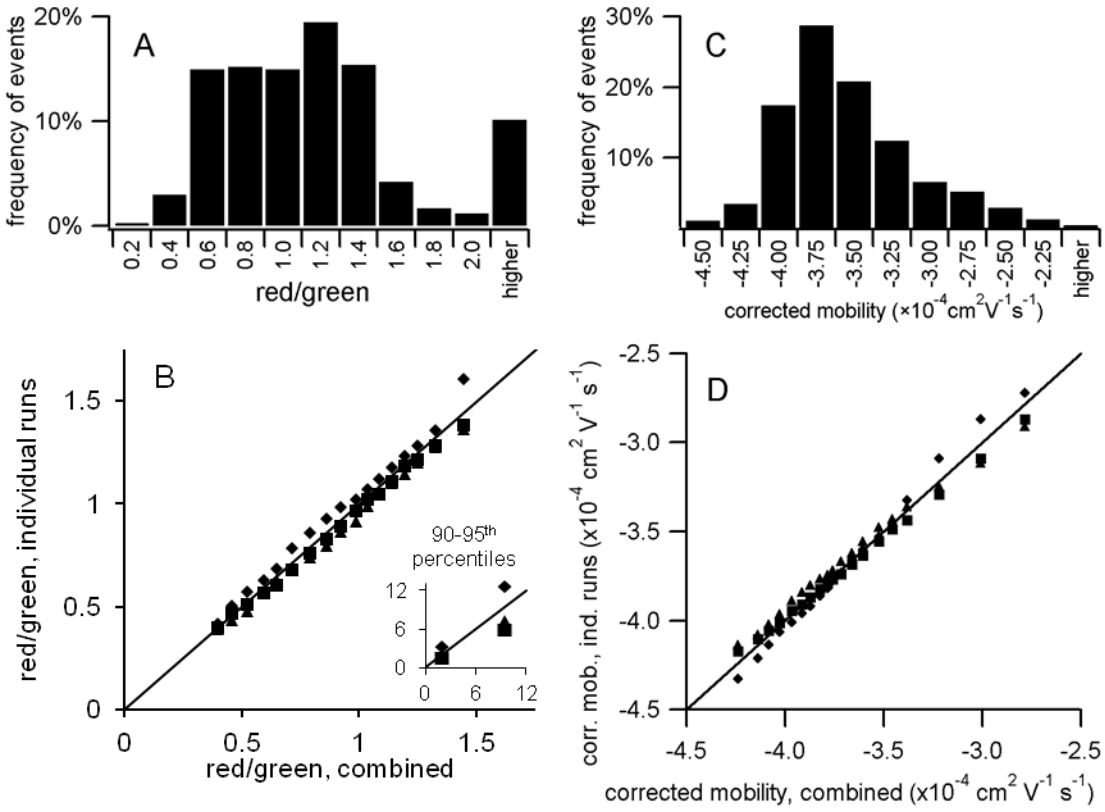

Figure 5-3. Reproducibility in multiple CE-LIF runs of polarized mitochondria isolated from C2C12 cells. A) Distribution of red/green ratios from three combined replicate runs, n = 950 detected events. B) Q-Q plot of red/green ratios from individual runs vs. combined data. This plot is a qualitative indication that the distributions of red/green ratios are reproducible (i.e. data points closely follow the *y* = *x* line shown on the plot). There is much more run-to-run variation in the 90-95th percentiles (inset in Q-Q plot in B, normalized ss_{res} = 352%, 221%, and 370% for runs 1, 2, and 3, respectively), but the 5-85th percentiles are reproducible (normalized ss_{res} = 26%, 18%, and 13% for runs 1, 2, and 3, respectively). C) Distribution of corrected electrophoretic mobility from the three combined runs. D) Q-Q plot of corrected mobility from individual runs vs. combined data. This plot is a qualitative indication that the distributions of corrected mobility are reproducible (i.e. data points closely follow the *y* = *x* line shown on the plot, normalized ss_{res} = 7%, 7%, and 5% for runs 1, 2, and 3, respectively). CE-LIF conditions as described in Figure 5-2.

5.3.3. Region of Interest (ROI) Analysis

When considering average values or overall distributions, differences in red and green fluorescence between polarized and depolarized samples were not as apparent in CE-LIF data as in bulk techniques. Several explanations are possible for this observation, including the presence of depolarized mitochondria in the polarized sample, overestimation of the membrane potential by the bulk fluorescence technique, and emission from monomers in depolarized mitochondria detected in the red fluorescence channel.

Depolarized mitochondria are expected in the mitochondrial preparations as a result of several experimental factors such as damage during mechanical homogenization or loss of membrane potential over time in isolated mitochondria. Harsh sample preparation methods (e.g. mechanical homogenization of cells and tissue[64] or mixing isolated mitochondria at 300 rpm during JC-1 labeling) could cause disruption and depolarization of some mitochondria, a change which may not be detected in bulk techniques. Isolated mitochondria lose membrane potential over time (see Figure C-3 in Appendix C), increasing the number of depolarized mitochondria in the polarized sample. All of these factors lead to the presence of depolarized mitochondria in samples typically used to assess polarization states. Additionally, there may be polarized mitochondria present in the depolarized sample: some mitochondria may be resistant to depolarization by valinomycin. Approximately 5% of a preparation of isolated mitochondria from rabbit kidney analyzed by flow cytometry were resistant to depolarization by FCCP.[66] The

authors of this study hypothesized that this resistance to depolarization could be due to higher amounts of cardiolipin in the inner membrane which acts as an “insulator” against depolarization. While FCCP is a protonophore, it is feasible that differences in membrane structure could also affect potassium transport by valinomycin through the inner membrane, leading to different degrees of resistance to depolarization.

Bulk fluorescence techniques are insensitive to the presence of depolarized mitochondria in samples containing polarized mitochondria. In the bulk fluorescence technique, it is not possible to estimate the fraction of mitochondria which are depolarized since the signal indicating polarization (e.g. red fluorescence) is from polarized mitochondria and is not necessarily influenced by the presence of depolarized mitochondria in the sample. For example, a sample containing equal amounts of both polarized and depolarized mitochondria would exhibit the same bulk red/green ratio as a sample with the same volume containing the same amount of polarized mitochondria but no depolarized mitochondria (assuming that the depolarized mitochondria do not accumulate any JC-1). Therefore, bias exists in this technique toward overestimation of the fraction of polarized mitochondria.

The detection scheme used in CE-LIF may overestimate the membrane potential of depolarized mitochondria. The 488 nm laser used excites the JC-1 monomers with high efficiency, and fluorescence from depolarized mitochondria containing only monomers is likely also detected in the red channel. This was observed in a flow cytometry experiment using cultured cells; cells depolarized with valinomycin and

excited at 488 nm exhibited significant fluorescence detected in the 585/42 nm channel of a flow cytometer; in fact, 30% compensation (subtraction of 30% of the fluorescence signal in the green channel from the signal in the red channel) was needed to separate this population of cells from polarized cells.[58]

The advantages of CE-LIF over bulk techniques are that hundreds of individual mitochondria are analyzed in a single 15-minute run and electrophoretic mobility data is collected. This allows for determination of individual mitochondrial membrane potential and investigation of mitochondrial heterogeneity. Most importantly, detection of individual mitochondria makes it possible to investigate mitochondrial membrane potential heterogeneity in CE-LIF runs containing both polarized and depolarized mitochondria; we accomplish this by definition of polarized and depolarized ROIs.

Polarized and depolarized ROIs were defined using the mitochondrial events from CE-LIF runs of polarized and depolarized (treated with valinomycin) samples and plots of red vs. green fluorescence for individual events (see Figure 5-4). The slope of a line defining the polarized and depolarized ROIs was varied to maximize the difference in the percentage of events in the polarized ROI between polarized and depolarized samples. This slope was found to be 0.96 for mitochondria from cells, 1.48 for mitochondria from muscle, and 1.47 for mitochondria from liver (see Figure C-10 and Table C-3 in Appendix C). Since the optimal ROIs for data from both muscle and liver were similar, an intermediate value of 1.475 was used to define the ROIs in both of these sample types to allow for direct comparison. Polarized ROIs contained 53% of the total events in

polarized samples from cells (a difference of 8% over the percentage of events from the depolarized samples in this ROI), 49% of the total events in polarized samples from muscle (a difference of 38%), and 18% of the total events in polarized samples from liver (a difference of 8%). A result that validates this approach is that the median red/green ratios in the depolarized ROI are similar in data from both polarized and depolarized samples (see Figure 5-5). As shown in Figure 5-4 B, mitochondrial events from polarized runs fall within both the polarized and depolarized ROIs. This approach allows for the comparison of subpopulations of polarized and depolarized mitochondria within a single sample.

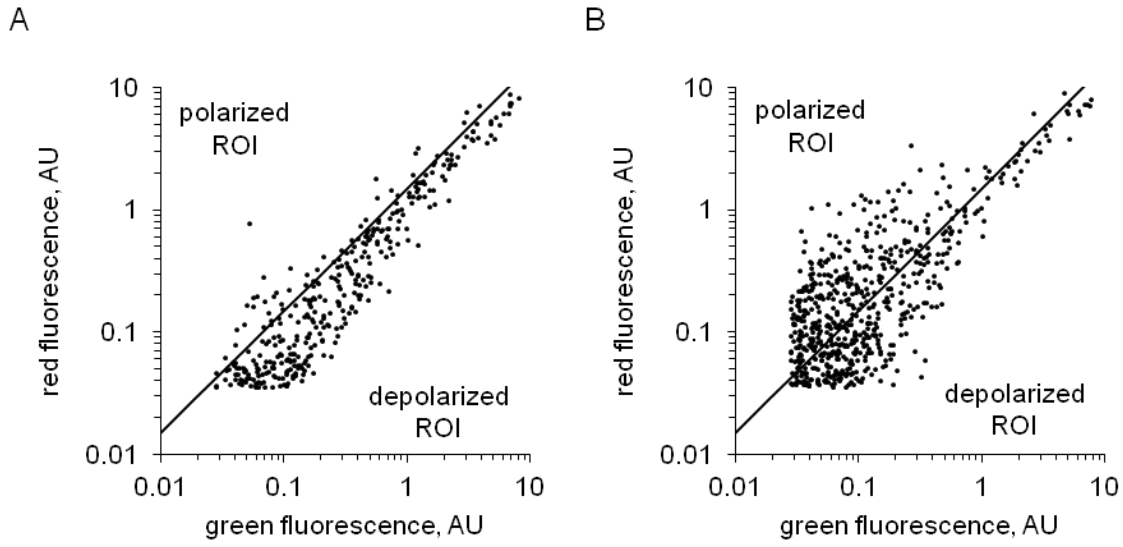

Figure 5-4. Definition of ROIs in CE-LIF. A) Mitochondrial events from depolarized muscle sample with depolarized ROI shown. B) Mitochondrial events from polarized muscle sample with depolarized ROI shown. CE-LIF conditions as in Figure 5-2. Plots are shown using a logarithmic scale. Plots with a linear scale are shown in Figure C-11 in Appendix C.

5.3.4. Comparison to Bulk Measurement

Average values from distributions of red/green ratios of individual mitochondrial events may be compared to results from measurements of bulk JC-1 fluorescence. In Figure 5-5, overall average red/green ratios and average red/green ratios from polarized and depolarized ROIs from CE-LIF analysis of individual mitochondria from liver and muscle tissue are compared to red/green ratios from bulk fluorescence measurements. Red/green ratios are generally higher in polarized samples in all groups, although the differences are not as pronounced when examining overall average values from CE-LIF data, indicating the presence of depolarized mitochondria in these polarized samples; analysis of ROIs is needed. Mitochondria from muscle generally have higher membrane potentials than mitochondria from liver in the CE-LIF runs, although this trend is reversed in bulk fluorescence measurements. Generally, liver mitochondria have higher membrane potential than muscle mitochondria under similar conditions (availability of substrate and respiratory rate).[178] In this experiment, muscle mitochondria were analyzed by CE-LIF before liver mitochondria, so liver mitochondria may have degraded and suffered losses in membrane potential by the time they were analyzed. Indeed, the first sample of liver mitochondria was analyzed 90 min after the first sample of muscle mitochondria and approximately 3 hours after the procedure for mitochondrial isolation was performed, the results in Figure C-3 in Appendix C indicate that some depolarization occurs over this time frame. In one sample of isolated mitochondria labeled with JC-1, red/green ratio decreased to 32% of its initial value over 256 min. Since isolated

mitochondrial samples were kept on ice before being labeled with JC-1 and aliquots were labeled directly before CE-LIF analysis (see Figure 5-3 in Appendix C), a more relevant comparison is that of the red/green ratio measured in the initial aliquot at t = 36 min after mitochondrial isolation to the aliquot kept on ice then labeled and measured 200 min after isolation. This sample has a red/green ratio of 79% of the first sample. Therefore, we can assign around 20% of the observed depolarization to an effect of time.

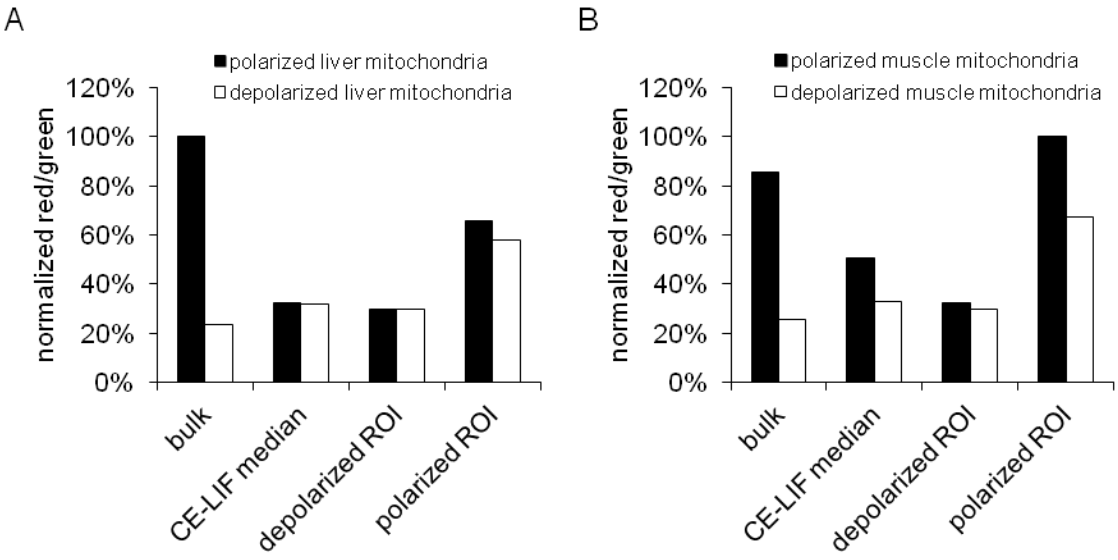

Figure 5-5. Comparison of red/green ratios from bulk measurements to median values and ROIs from CE-LIF. Mitochondria isolated from mouse liver (A) and muscle (B) tissue. All bulk measurements normalized to the highest red/green ratio among bulk measurements; all CE-LIF median values are normalized to the highest median value among CE-LIF groups (median, depolarized ROI, and polarized ROI in each sample). Bulk fluorescence measurements collected as in Figure 5-1 E, CE-LIF conditions as in Figure 5-2.

5.3.5. Comparison of ROIs and Dependence of Electrophoretic Mobility on Membrane Potential

The Q-Q plots of red/green ratio illustrate little difference in the overall distributions between polarized and depolarized samples (Figure 5-6 A and C), but a clear difference in the distributions between polarized and depolarized ROIs from polarized and depolarized samples (Figure 5-6 B and D), illustrating the utility of using ROIs to examine differences between these samples. Likewise, there is only a slight difference in the overall distributions of corrected electrophoretic mobility between polarized and depolarized samples (Figure 5-7 A and C), with the polarized sample distribution slightly less negative than the depolarized sample distribution. However, the difference in corrected electrophoretic mobility distributions between polarized and depolarized ROIs from polarized and depolarized samples is more pronounced (Figure 5-7 B and D). This result indicates an effect of membrane potential on electrophoretic mobility, with higher membrane potential generally resulting in less negative mobility. Indeed, relationships between membrane potential and electrophoretic mobility have been observed in mitochondria.[164,166,172] In these studies, polarization was reported to increase mitochondrial surface charge density (resulting in more negative electrophoretic mobility), which is contradicted by the results obtained here. However, the results obtained in previous studies used a different method to observe mitochondrial mobility. Mitochondrial migration was observed directly in a flat quartz electrophoresis chamber at the stationary layer (i.e. a distance from the surface under conditions of net zero EOF). If

the location of the stationary layer was estimated inaccurately, EOF would have an effect on the observed apparent mobility of mitochondria. In our work, mobilities were corrected for EOF based on the migration time of fluorescein, and EOF was reduced by the PVA capillary coating. Additionally, we used valinomycin to depolarize mitochondria, and the comparisons made in the previous studies were between mitochondria before and after addition of succinate in the presence of rotenone[166] and the inhibitors FCCP, antimycin A, and potassium cyanide, which may have a different effect on the surface charge density of mitochondria.[164] Differences in the ionic strength of the buffers used is also likely to influence the results – the electrophoretic mobilities of liposomes with pH gradients across their membranes were found to depend on ionic strength of the medium, with a complete change in the elution order of different liposomes caused by a change in ionic strength from 9 mM to 45 mM.[80] Further investigation is needed into the relationship between membrane potential and electrophoretic mobility.

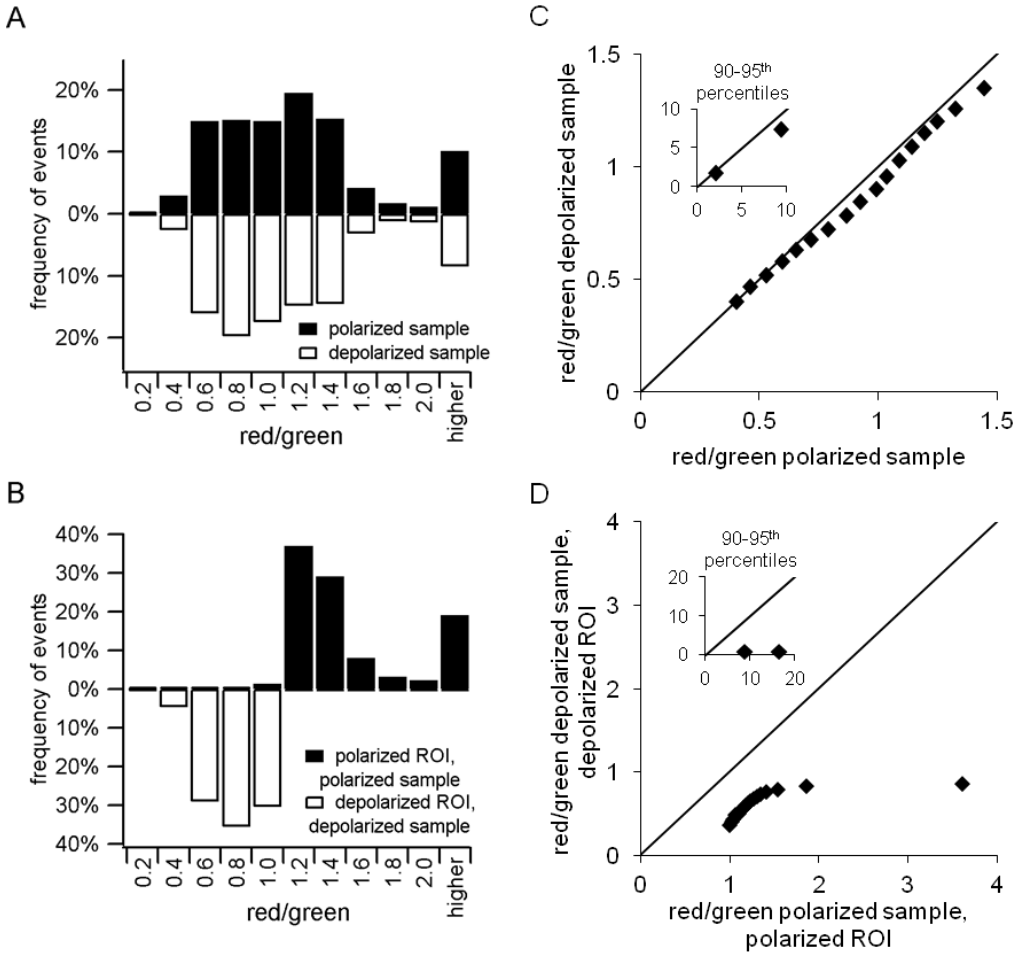

Figure 5-6. Comparison of red/green ratio distributions between polarized and depolarized samples and ROIs using mitochondria isolated from C2C12 cells. A) Histograms of polarized and depolarized samples. Polarized: n = 950 events, 3 runs. Depolarized: n = 906 events, 3 runs. B) Histograms of polarized ROIs from polarized samples and depolarized ROIs from depolarized samples. Polarized ROI: n = 501 events, 3 runs. Depolarized ROI: n = 503 events, 3 runs. C) Q-Q plot of depolarized vs. polarized samples. Differences between the overall distributions are not pronounced (i.e. data points do not deviate much from the $y = x$ line shown on the plot, normalized ss_{res} = 24% for the 5-85th percentiles). There is much more variation in the 90-95th percentiles (inset in Q-Q plot in C, normalized ss_{res} = 208%). D) Q-Q plot of depolarized ROI from depolarized samples vs. polarized ROI from polarized samples. The large deviation of the data from the $y = x$ line confirms the difference in red/green ratio used to define these ROIs and demonstrates the difference between the two distributions of red/green ratio (normalized ss_{res} = 304% for the 5-85th percentiles and 1412% for the 90-95th percentiles). CE-LIF conditions as in Figure 5-2.

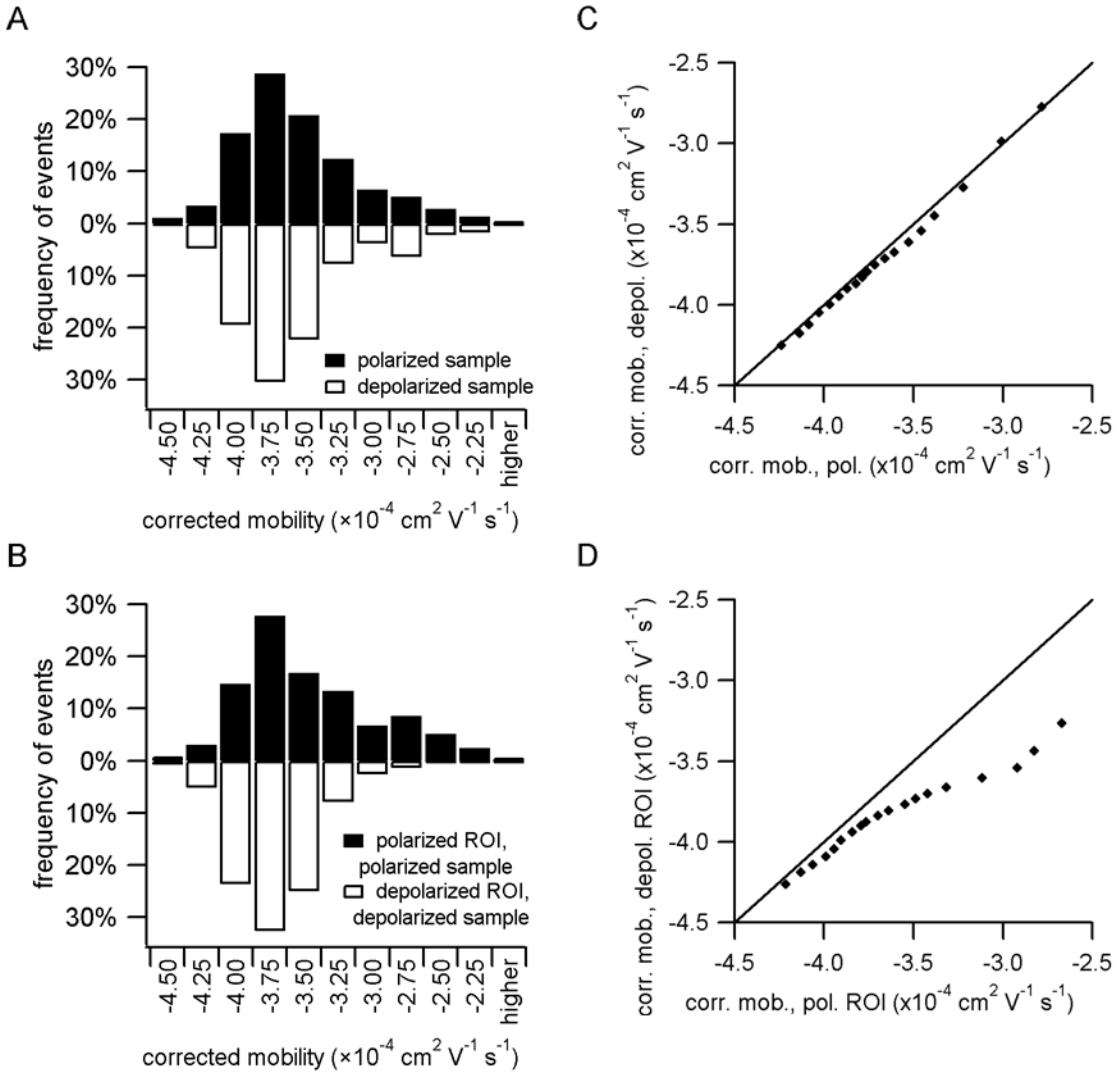

Figure 5-7. Comparison of corrected electrophoretic mobility distributions between polarized and depolarized samples and ROIs using mitochondria isolated from C2C12 cells. A) Histograms of polarized and depolarized samples. B) Histograms of polarized ROIs from polarized samples vs. depolarized ROIs from depolarized samples. C) Q-Q plot of depolarized samples vs. polarized samples. Differences between the overall distributions are not pronounced (i.e. data points closely follow the $y = x$ line shown on the plot, normalized ss_{res} = 6%). D) Q-Q plot of depolarized ROI from depolarized samples vs. polarized ROI from polarized samples. Deviation from the $y = x$ line demonstrates the differences in some, but not all, percentiles in these distributions (normalized ss_{res} = 37%). CE-LIF conditions as in Figure 5-2.

5.3.6. Comparison of Liver and Muscle Tissue Mitochondria

The distributions of red/green ratio and corrected electrophoretic mobility from polarized and depolarized mitochondria isolated from mouse muscle and liver tissue are shown in Figure 5-8. In mitochondria from muscle, differences in the red/green ratio distributions between polarized and depolarized samples were apparent even in the overall data, and were more pronounced in the ROI comparison (Figure 5-8 A). Differences in the distributions of red/green ratio from liver mitochondria were less pronounced between polarized and depolarized mitochondria when considering the overall distributions, this observation illustrates the value of measuring individual mitochondrial membrane potential and defining ROIs. As discussed previously, this result could reflect mitochondrial degradation due to the sample preparation procedure or loss of membrane potential over time, as these samples were analyzed after the muscle samples. This result supports the utility of defining a polarized ROI: as more mitochondria lose membrane potential over time, mitochondria remaining in the polarized ROI may still be used for comparison to depolarized mitochondria. Differences in distributions of corrected electrophoretic mobility are similar to those observed in the experiments with mitochondria isolated from cells. The polarized ROIs from liver and muscle tissue mitochondria exhibit mobility distribution that are shifted toward less negative mobilities when compared to the distributions from the depolarized ROIs (Figure 5-8 B and D). The Q-Q plot allows for comparisons of subtle differences between these distributions. For example, while the mobility distributions for polarized ROIs from

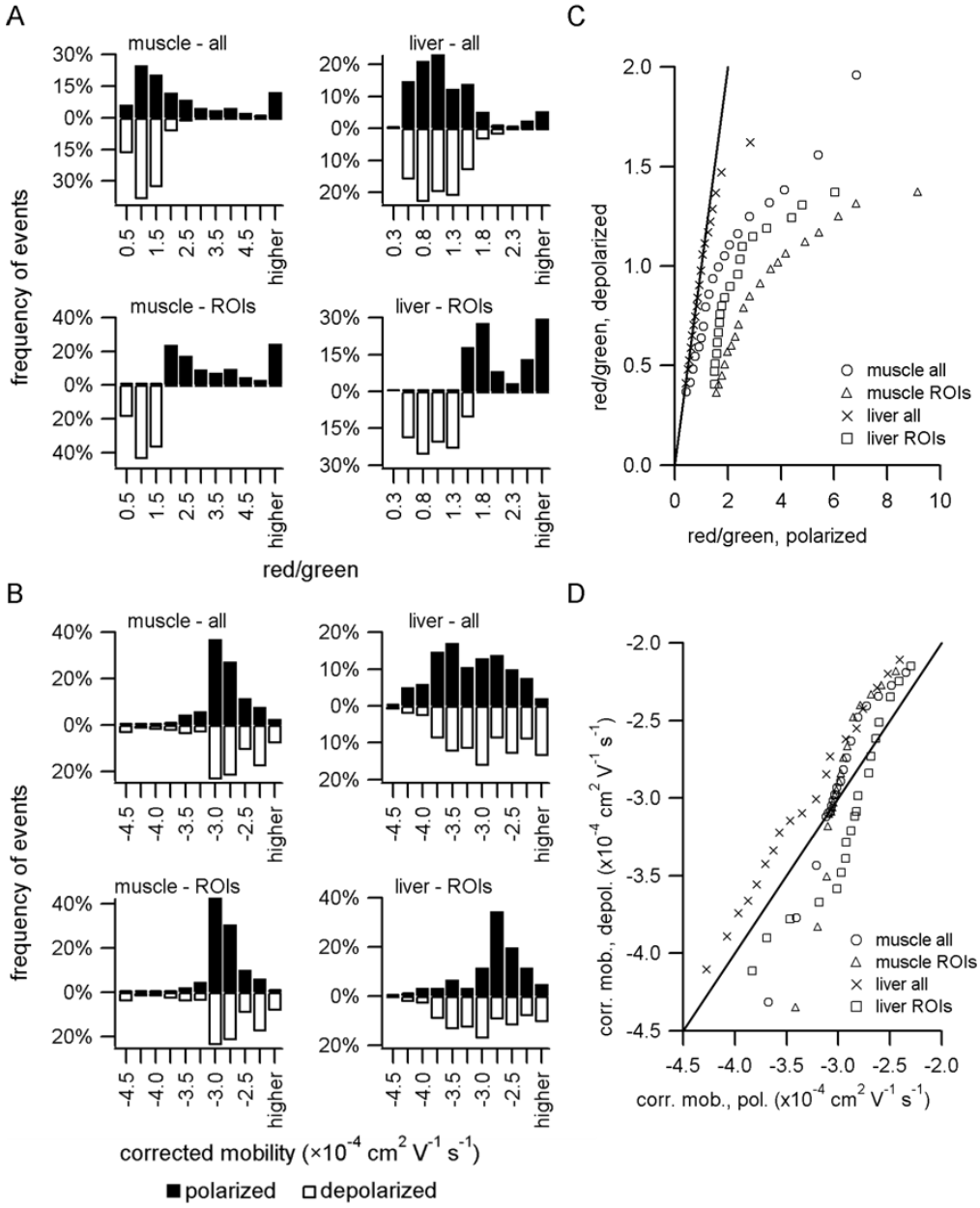

Figure 5-8. CE-LIF of muscle and liver tissue mitochondria. Histograms and Q-Q plots of red/green ratio (A and C) and corrected electrophoretic mobility (B and D). Comparisons are made between polarized and depolarized samples (all events) and between events in polarized ROIs from polarized samples and events in depolarized ROIs from depolarized samples. See Table C-3 for number of events and Table C-4 for normalized ss_{res} from Q-Q plots (in Appendix C). Position of $y = x$ line in C results from different ranges used for x and y axes. CE-LIF conditions as in Figure 5-2.

both muscle and liver tissue are shifted toward less negative values, the difference in the distributions between polarized and depolarized ROIs from liver is more uniform (i.e. points for most percentiles are evenly spaced and fall away from the $y = x$ line). This reflects the broader shape of the distributions of corrected mobility from liver mitochondria compared to muscle, which could reflect more heterogeneity in the surface composition of these mitochondria.

5.4. Conclusions

This chapter describes a method to measure membrane potential distributions in mitochondria using the ratiometric dye JC-1. An important advantage of this method over bulk measurements of membrane potential is the ability to characterize mitochondrial heterogeneity. Mitochondrial membrane potential is heterogeneous depending on subcellular location,[19,20] functional status and morphology,[20,21,168] and oxidative damage to mitochondria,[22] and plays an important role in mitochondrial maintenance by the fusion/fission process[23] and turnover by mitophagy.[24] Flow cytometry and microscopy are suitable techniques for evaluation of membrane potential heterogeneity, and similar results have been obtained to the results obtained in this work (i.e. flow cytometry[66] and microscopy[19] have been used to observe broad distributions of membrane potential and changes upon depolarization). However, CE-LIF provides the additional advantage of a separation based on mitochondrial electrophoretic mobility, which has the potential for characterization of subpopulations of mitochondria with different surface properties.

The method is applicable to mitochondria isolated from cultured cells and from muscle and liver tissue. Application of the method to these different samples revealed heterogeneity in mitochondrial membrane potential and electrophoretic mobility. Analysis of ROIs revealed additional differences between samples, and an effect of membrane potential on electrophoretic mobility.[164,166,172] The analysis of ROIs makes it possible to analyze polarized mitochondria in samples where depolarized mitochondria are present due to experimental factors that result in damage to mitochondria or loss of membrane potential in the time elapsed between preparation and analysis.

This work enables future studies of the relationship between mitochondrial membrane potential and electrophoretic mobility. Additional investigation of this relationship would aid in interpretation of data from CE-LIF experiments: the relative contributions of membrane potential and mitochondrial surface composition to mobility is unknown. For example, the effects of different inhibitors of mitochondrial respiration or depolarizing agents could be investigated and compared to the effects of treatments to the mitochondrial surface (e.g. trypsin to cleave cytoskeletal proteins).[40] Different modes of separation could also be used; for example, this labeling scheme could be used with capillary isoelectric focusing to determine relationships between mitochondrial isoelectric point and membrane potential. This technique allows for measurement of a different mitochondrial surface property which may be useful in assessing changes to the surface relevant to membrane potential (e.g. ubiquitination by PINK1/Parkin as a signal for elimination by mitophagy). Since the sample requirement is small and the method allows

for analysis of membrane potential even if some mitochondria are disrupted during sample preparation, this method could even be applied to other cell or animal models or even human tissue samples to study mitochondrial heterogeneity.

Chapter 6.

Conclusions

This main outcomes of the work described in this thesis include development of a method to measure individual p*I*s in isolated mitochondria by cIEF with laser-induced fluorescence detection, simulation of the contribution of mitochondrial surface compositions to p*I* and prediction of p*I* changes with changes in surface composition, and development of a method to measure individual mitochondrial membrane potential by CE-LIF.

In Chapter 3, we report a method for separation of mitochondria isolated from L6 rat myoblasts by cIEF with laser-induced fluorescence detection. This method revealed a distribution of individual mitochondrial p*I*, which were determined accurately through the use of fluorescent p*I* markers as internal standards. This method is reproducible and sensitive to changes in the mitochondrial p*I* distribution upon treatment with trypsin, which modifies proteins associated with the surface of the mitochondria. The ability to determine the p*I*s of individual mitochondria is an important tool for characterizing mitochondrial heterogeneity and detecting changes to the composition of the surface of mitochondria. One limitation of the method is the definition of the pH gradient above the pI 6.5 marker; improvements to the method to address this limitation are described in Chapter 7.

In Chapter 4, we describe a method to predict individual mitochondrial p*I* values using simulated surface compositions. These compositions consist of different percentages of amino acids and phospholipids found in the mitochondrial outer membrane. This method is able to match p*I* distributions of isolated mitochondria

determined by cIEF and make predictions about the individual compositions associated with experimental p*I* values. We validated the method by predicting the amino acid compositions of known mitochondrial outer membrane proteins. This method is a valuable tool to model the heterogeneity of mitochondrial p*I* and can be used to predict changes in p*I* upon changes to surface composition. In Chapter 7, we discuss possible future use of this model to predict changes in mitochondrial p*I* arising from modifications to the mitochondrial surface expected in targeting for mitophagy or upon depolarization.

Chapter 5 describes a method to measure individual mitochondrial membrane potential using CE-LIF. Mitochondria from cultured cells and mouse muscle and liver tissue were isolated, labeled with the ratiometric dye JC-1, and separated by CE-LIF which revealed heterogeneity in mitochondrial membrane potential and electrophoretic mobility distributions. Analysis of specific regions of interest defined using depolarized samples makes it possible to analyze polarized mitochondria in samples where depolarized mitochondria may be present due to biological variation or experimental factors that result in damage to mitochondria. This analysis revealed additional differences between samples, and an effect of membrane potential on electrophoretic mobility. An important advantage of this method is the ability to measure individual mitochondrial membrane potential and electrophoretic mobility, which allows for characterization of subpopulations of mitochondria with different surface properties. In Chapter 7, we discuss possible future adaptation of the labeling method described in

Chapter 5 to cIEF, which would allow for investigation of the relationships between mitochondrial p*I* and membrane potential.

Overall, the work described in this thesis represents development of new methods to study mitochondrial heterogeneity in terms of isoelectric point, surface composition, and membrane potential. Application of these methods to biological models could reveal subpopulations of mitochondria within heterogeneous populations that make critical contributions to aging and disease. Identification of the role played by these subpopulations would increase our fundamental understanding of these organelles and their contribution to aging. Insights gained through elucidation of the role of mitochondrial dysfunction and heterogeneity in aging could eventually lead to new treatments for age-related disorders and disease.

Chapter 7.

Future Work

Dr. V. Kostal cultured cells for the preliminary experiment described in Figure 7-3, and collected and analyzed the data presented in Figures 7-5 and 7-6. S. Rose collected and analyzed the data presented in the preliminary experiment shown in Figure 7-7. All other data collection and analysis for preliminary experiments was performed by G. Wolken.

In this chapter, we describe future improvements to the methods described in this thesis and applications of those methods to biological models of aging. Future improvements to the cIEF method described in Chapter 3 are discussed that will improve its analytical capabilities of accurately measuring the p*I*s of individual organelles, separating mitochondria in different p*I* ranges, and determining membrane potential. Applications of the model of mitochondrial p*I* described in Chapter 4 to understand better the implications of mitochondrial heterogeneity observed by cIEF are discussed. This chapter also describes future experiments necessary to develop a new technique for individual mitochondrial isolation by cytoskeletal disruption and electroporation which is necessary for characterization of giant mitochondria in a cell model of aging by the methods described in this thesis.

7.1. Improvements to cIEF Method

The application of the cIEF method described in Chapter 3 to biological models of aging may present new analytical challenges. Subpopulations of mitochondria in these models may be difficult to detect due to small size or low fluorophore content, which would require improvements in the limit of detection of the technique. Additionally, mitochondria from different biological systems (e.g. different tissues) may have p*I*s that fall outside the range of the cell model studied in Chapter 3. Adequate separation and accurate measurement of the p*I*s of these organelles would require changes in the p*I* markers and compounds used for focusing and mobilization. This section describes several techniques which may be implemented to improve the cIEF method discussed in

Chapter 3. These modifications would improve the limit of detection of the technique and provide better separation and accurate measurement of a wider range of p*I*s.

7.1.1. Post-Column Detection

One limitation of the cIEF method described in Chapter 3 is the achieved limit of detection. Low detection limits are important in individual organelle analysis due to the small relative intensity of the signals above the background; if detection limits are too high, smaller organelles or those that do not contain enough of the fluorescent probe used may be missed. To perform the cIEF experiments described in Chapter 3 of this work, the instrument was modified to perform on-column detection, which resulted in a higher limit of detection than previously achieved using the same instrumentation. A limit of detection of 29 ± 4 zmol was reported for fluorescein (see Chapter 3), higher than the result of 4 zmol achieved using post-column detection for CE-LIF.[40] This modification was originally performed for addition of a sample carousel at the outlet end of the capillary to allow for switching between the catholyte and chemical mobilization solutions after focusing was complete. This configuration also prevented contact between the strong base (NaOH) used as the catholyte solution and the quartz sheath flow cuvette of the instrument, since strong bases attack glass.

Adapting the instrument to perform cIEF using the sheath-flow cuvette provides the advantages of post-column detection. First, an increase in sensitivity is expected since refraction of the excitation and emission light at interfaces is minimized. Excitation light and fluorescence emission from the sample must travel through the capillary walls to

perform on-column detection; this is a problem because the capillary is cylindrical and light will refract at the glass-solution interfaces where curvature is present. With post-column detection, these interfaces are eliminated; minimal refraction should occur since the walls of the sheath-flow cuvette are perpendicular to the excitation and emission light paths. Additionally, post-column detection provides more control over the alignment for better detection of particles. The sheath-flow velocity can be adjusted to focus the sample stream exiting the capillary, and the capillary tip can be moved up or down so that a more narrow section of this stream is in front of the detector, improving the relative standard deviation of the signal detected from particles (e.g. see Figure C-5 in Appendix C). Capillary isoelectric focusing has been performed using post-column detection on a similar instrument.[114,179]

Figure 7-1 below shows a separation of p*I* markers after modification of the instrument to perform post-column detection. A valve was added to the sheath flow tubing between the sheath-flow buffer reservoir and the cuvette (see Figure 2-3 in Chapter 2) to select between two wash bottles containing catholyte (20 mM NaOH) and chemical mobilizer (350 mM acetic acid). Initially, catholyte is flowing through the cuvette; when focusing is complete, the valve is switched to the chemical mobilizer. This separation shows an average resolving power of $\Delta pI = 0.01$, better than the previous result of 0.03 with on-column detection described in Chapter 3. These results are from different experiments, so differences in the coatings of the capillaries used or in the ampholytes are more likely to have caused the difference in resolving power. While the

apparent gain in resolving power is probably not caused by the use of post-column detection, this result demonstrates that the resolving power is not negatively impacted.

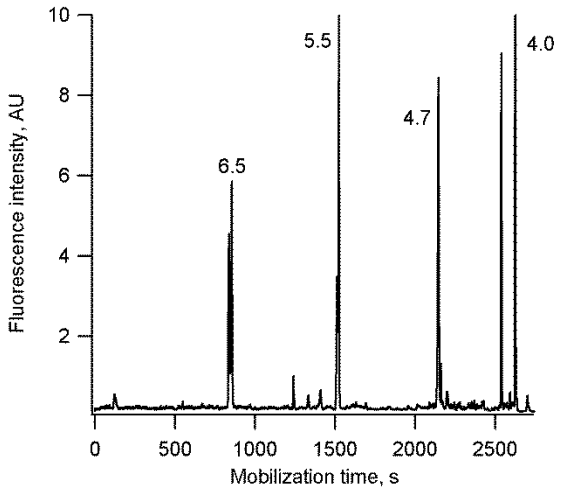

Figure 7-1. cIEF with post-column detection. Anolyte: 100 mM H_3PO_4;catholyte: 20 mM NaOH; chemical mobilizer: 350 mM acetic acid. Focusing: 400 V/cm for 23 minutes. Detection: 520 ± 17.5 nm. Ampholytes: 1% Biolyte 3-10, 1% Biolyte 4-6, 1% Pharmalyte 5-8 (GE Healthcare, Pittsburgh, PA). All other conditions as described in Figure 3-1, Chapter 3.

One issue involved with performing post-column detection is exposure of the quartz sheath-flow cuvette to a strong base, which will cause damage over time. To prevent this issue, another anolyte/catholyte combination (glutamic acid/lysine) should be used. This anolyte/catholyte has been reported to provide no difference in performance in terms of resolution between proteins in a test mixture when used with a coated capillary.[180] The results shown below in Figure 7-2 demonstrate the use of glutamic acid and lysine as an alternative anolyte and catholyte. Compared to the classical anolyte/catholyte pair of H_3PO_4/NaOH, there is no significant difference in resolving power. This combination should be used in future cIEF experiments with post-column detection to prevent damage to the sheath-flow cuvette.

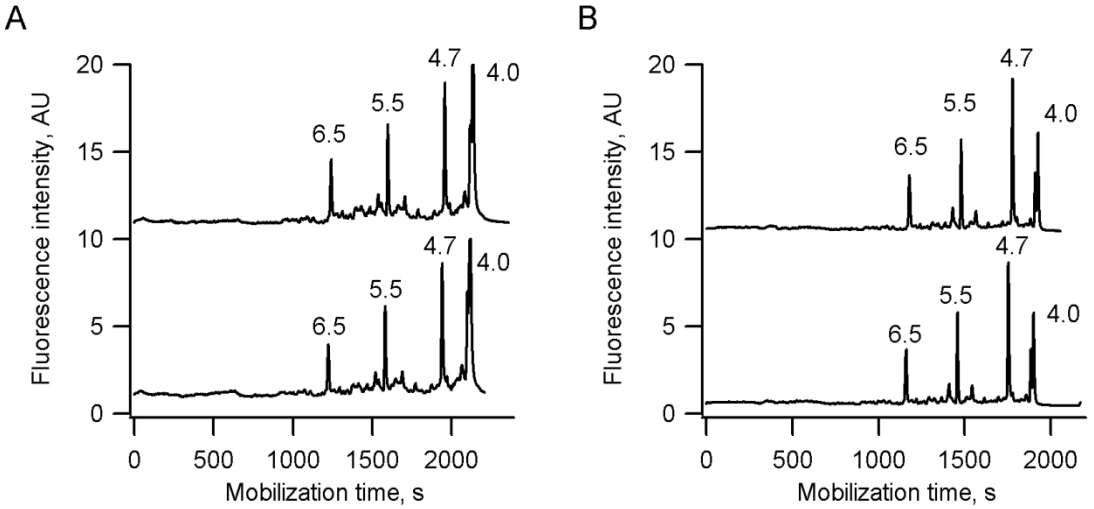

Figure 7-2. Comparison of lysine/glutamic acid to H_3PO_4/NaOH as anolyte/catholyte in cIEF. (A) Two replicate separations of p*I* markers using 50 mM glutamic acid/50 mM lysine (Sigma-Aldrich, Saint Louis, MO) as anolyte/catholyte, average resolving power $\Delta pI = 0.04 \pm 0.02$. (B) Two replicate separations using 100 mM H_3PO_4 and 20 mM NaOH (Sigma-Aldrich) as anolyte/catholyte. Average resolving power $\Delta pI = 0.04 \pm 0.01$. Top traces in A and B have y-offset = 10. Focusing: 400 V/cm for 23 minutes. Ampholytes: 1% Biolyte 3-10, 1% Biolyte 4-6, 1% Pharmalyte 5-8. Chemical mobilizer: 10 mM glutamic acid. Detection: 535 ± 17.5 nm. All other conditions as described in Figure 3-1, Chapter 3.

7.1.2. Ampholytes

In the work described in Chapter 3, Biolyte 3-10 was mixed with Biolyte 4-6 to improve resolution between pH 4 and 6 because previous reports of mitochondrial p*I* were between 3.9 and 6.[130-134] The work described in Chapter 3 revealed that mitochondrial p*I*s were distributed between 3.9 to 6.9 (see Chapter 3, Table 3-1) Blending different pH ranges of ampholytes or solutions of the same pH range from different suppliers can improve resolution in cIEF.[106] Increases in resolution in terms of resolving power cannot be predicted since carrier ampholytes are complex mixtures of many compounds of unknown structure. However, the separation of two compounds with

very similar p*I*s can be improved since the chances that an ampholytes with intermediate p*I* will be present (a prerequisite for separation in cIEF) are increased. Likewise, use of a narrow pH-range mixture of ampholytes can improve resolution in a specific pH range of interest by increasing the number of ampholytes in that range. In Figures 7-1 and 7-2 shown above, Pharmalyte 5-8 was added to the two pH ranges of Biolyte, this should improve resolution across the entire pH range where mitochondria were focused. The results in Figure 7-1 suggest an improvement in resolving power (average $\Delta pI = 0.01$), but the results in Figure 7-2 did not improve over the resolving power reported in Chapter 3 ($\Delta pI = 0.04$ in Figure 7-2, 0.03 reported in Chapter 3). An additional experiment is needed since these results were obtained on different days using different capillaries, so the capillary coating could have affected the resolving power.

In one of the reports mentioned in the previous paragraph, mitochondria isolated from rat kidney had an average p*I* of 3.9.[130] Since mitochondrial p*I* is heterogeneous, this suggests that some mitochondria in this preparation had p*I*s significantly lower than 3.9, implying a significant contribution from molecules in the outer membrane with low pK_as such as glu, asp, PI, or PS (see Table 4-1 in Chapter 4). Future analysis using cIEF of mitochondria from different biological sources, other organelles, or other particles may therefore require improvements to focusing performance at the ends of the pH gradient (i.e. 3 and 10 in the current system). One method to accomplish this is the inclusion of so-called sacrificial ampholytes.[181] In this technique, additional compounds with high and low p*I* are added to the ampholytes. Iminodiacetic acid and arginine have been used,[181]

but any combination of zwitterionic compounds with p*I*s higher and lower than the range of the ampholytes could be used. During focusing, there is loss of high- and low-p*I* ampholytes and sample components due to an isotachophoretic process at either end of the capillary. If appropriate sacrificial ampholytes are chosen (i.e. one with higher p*I* and one with lower p*I* than the pH range of the ampholytes used), these compounds focus at either end of the capillary. During focusing, these sacrificial ampholytes will gradually migrate out of either end of the capillary instead of the ampholytes and sample components near the ends of the pH gradient, and the full range of the pH gradient is better preserved.

7.1.2. p*I* Markers

In the cIEF method described in Chapter 3, the internal standards used had a minimum p*I* of 4.0 and a maximum p*I* of 6.5. However, individual mitochondria were detected with p*I*s from 3.9 to 6.9 (see Table 3-1 in Chapter 3), therefore some reported p*I*s were extrapolated. Since the pH gradient in cIEF is known to be non-linear,[111] assigning p*I* values to analytes via extrapolation is problematic. If better accuracy is needed in determination of the p*I*s of analytes outside the range of the markers used in the current method, additional p*I* markers could be added. As discussed in Chapter 2, any combination of small molecule p*I* markers,[115] fluorescent peptides,[111] or proteins labeled with Chromeo dyes[114] could be used. See the recent review by Righetti for a table of 17 commercially available proteins and tryptic peptides produced by a digest of cytochrome C that could be used as markers with p*I* ranging from 3.67 to 10.65.[112]

7.2. Application of cIEF to Aging Models

7.2.1. Application to Cell Model

In a cell model of aging with impaired autophagy, heterogeneity in mitochondrial size, membrane potential, and expression of proteins involved in fusion and fission was observed.[18] In this work, a pharmacological inhibitor, 3-methyl adenine, was used to block autophagy through inhibition of class III phosphatidylinositol 3-kinases. The formation of giant mitochondria with diameters larger than 1 μm was observed. These giant mitochondria expressed lower levels of a fusion protein, Opa1, and had significantly lower membrane potentials when compared to smaller mitochondria. They were observed to be excluded from the fusion process and did not exchange their contents with normal mitochondria. These differences suggest giant mitochondria represent a separate subpopulation of dysfunctional mitochondria. Although they have been studied using existing methods, the mechanism of formation of giant mitochondria, the causes of their accumulation in aging cells, and the extent of their damage and dysfunction are not completely understood – these organelles are difficult to study since they coexist with normal mitochondria in the cell and have not been isolated. The cIEF method described in Chapter 3 can be applied to cell models of aging containing giant mitochondria to determine whether there are differences in the mitochondrial p*I* distributions when compared to normal cells. If differences are determined, they could be used as a basis for separation of giant mitochondria from normal mitochondria and further characterization of their properties.

Since giant mitochondria have lower mitochondrial membrane potential, they could be targeted for elimination by mitophagy but not removed by this process, possibly because of hindrance in transport to the autophagosome due to their large size.[25] Upon loss of membrane potential, the protein PINK1 accumulates on the surface of mitochondria and recruits Parkin, which modifies mitochondrial proteins by ubiquitination.[24] This results in extraction and degradation of some mitochondrial proteins (e.g. MFN1 and MFN2), although this is not required for mitophagy and the complete mechanism for mitophagy targeting is not understood.[25] Accumulation of PINK1 and Parkin at the mitochondrial surface, ubiquitination, and degradation of surface proteins are all modifications that could result in changes to mitochondrial surface charge that would modify mitochondrial p*I*. Oxidative damage to mitochondrial proteins by increased levels of reactive oxygen species in aging cells, such as carbonylation of lysine, arginine, and histidine residues,[129] could also result in changes to p*I* by changing the net charge of these amino acid residues. Due to all these possible modifications, giant mitochondria are hypothesized to have different surface properties from normal mitochondria which would result in differences in p*I* which may be detected by cIEF.

The experiments described and proposed below use inhibition of ATG7 via siRNA as the preferred cell model of aging. Previous studies used 3MA to inhibit autophagy and form giant mitochondria in cell models.[17,18] 3MA inhibits formation of the isolation membrane, a step near the beginning of the autophagy pathway involved in

initial formation of the autophagosome.[182] As a result, 3MA can cause toxicity through its effects on other cellular pathways. A gene called autophagy-related gene 7 (ATG7) codes for a protein (also referred to as ATG7) involved in the vesicle elongation process, a step further downstream in the autophagy pathway.[182] Inhibition of this gene via transfection with silencing RNA (siRNA) has advantages over use of 3MA as an aging model, including less toxicity and less drastic impairment of autophagy (since this process still occurs in aging cells). Additionally, this model is being used in ongoing quantitative proteomics studies in the Arriaga lab.

The preliminary results in Figure 7-3 below show the p*I* distributions determined with cIEF of mitochondria from L6 cells treated with siRNA against ATG7 compared to mitochondria from control cells. The Q-Q plot suggests a difference in the p*I* distributions between these two groups, with the siRNA-treated cells displaying more mitochondrial events with lower p*I*s. However, the number of events detected is likely too small to draw conclusions about real differences in the p*I* distributions between these two groups, and the two individual runs of each sample were not reproducible (data not shown), so the variation in the Q-Q plot cannot be assigned to a difference between the siRNA ATG7 and control groups. Moreover, these mitochondria were isolated by mechanical homogenization. This is a harsh technique which may not preserve the structure of giant mitochondria (see section 7.3.1 below). These experiments should be repeated with the disruption technique to be developed in future work described in section 7.3 below, which is expected to be compatible with release of giant mitochondria.

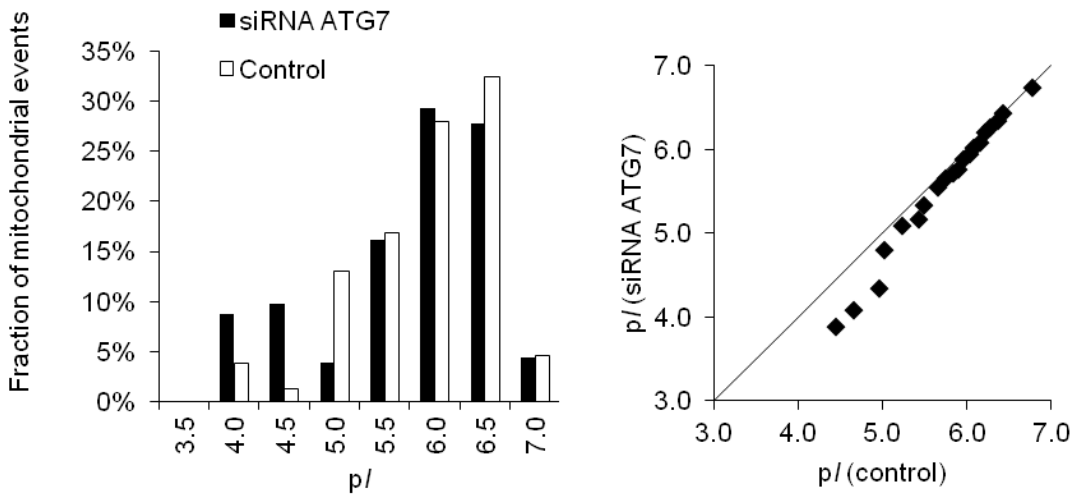

Figure 7-3. p*I* distributions determined by cIEF of mitochondria from siRNA ATG7-treated cells vs. control cells. L6 rat myoblasts were transfected with siRNA for ATG7 (40 nM siRNA for 24 hours with siRNA sequence: CCUGGUCAUCCAUUCUGCAGAAUAA) delivered with Lipofectamine 2000 (Invitrogen, Grand Island, NY) for 24 hours. Transfected and untreated (control) cells were harvested and mitochondria isolated by mechanical homogenization using a 2 mL glass dounce homogenizer with glass pestle with 0.06 mm clearance (Kontes, Vineland, NJ), labeled with 5 µM 10-N-nonyl acridine orange (NAO, Molecular Probes, Eugene, OR), and analyzed by cIEF. Focusing: 400 V/cm for 20 min. Mobilization: 500 V/cm. All other experimental details as described in Figure 3-1 in Chapter 3. Two cIEF runs were performed using each sample and combined. siRNA ATG7 cells: n = 205; control cells: n = 154. In this experiment, siRNA ATG7 cells were cultured and transfected by Dr. Vratislav Kostal.

One limitation in the application of the cIEF method to investigate mitochondrial heterogeneity in aging models is the dye used for labeling mitochondria. While NAO is specific to mitochondria, it does not indicate mitochondrial intactness or membrane potential, which may influence surface properties. Additionally, using NAO for labeling is not sufficient for detection of giant mitochondria in this technique as aggregates of normal mitochondria may be mistaken for giant mitochondria (e.g. both should display

intense NAO fluorescence). An additional improvement of this method would be to use JC-1 instead of NAO for labeling mitochondria. This would allow for studies relating membrane potential to p*I*, and could aid in identification of giant mitochondria in this technique as these organelles are hypothesized to have lower mitochondrial membrane potential than normal mitochondria.[18] The preliminary results shown below in Figure 7-4 demonstrate the feasibility of using this dye for cIEF. These results show detection of JC-1 labeled mitochondria from L6 cells in red and green fluorescence channels.

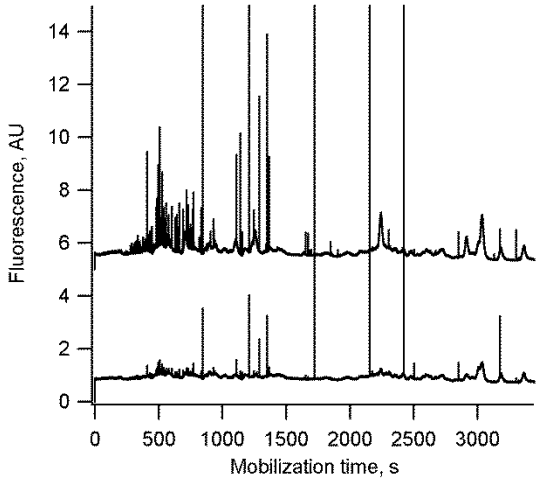

Figure 7-4. cIEF of JC-1 labeled mitochondria. Mitochondria from L6 cells were isolated using mechanical homogenization and labeled with 1 µM JC-1 for 5 min in buffer R with 2.5 mM succinate (see Chapter 5 for buffer R composition). They were then analyzed by cIEF as described in Figure 3-1 in Chapter 3. Red fluorescence channel: bottom trace, 593 ± 20 nm. Green fluorescence channel: top trace, 535 ± 17.5 nm, y-offset = 5. Single-laser excitation at 488 nm. Focusing: 400 V/cm for 21 min. Mobilization: 400 V/cm. n = 81 coincident mitochondrial events; 101 events in red channel and 243 events in green channel.

Several improvements may be needed to adapt the cIEF method to use of JC-1 as a dye for labeling mitochondria. For instance, the experiment shown in Figure 7-4 was performed using a single excitation wavelength and not the dual-laser excitation scheme

described in Chapter 5, this improved detection scheme should be used in the future. Also, no substrate was present in the focusing solution, so mitochondria may lose their membrane potential during focusing. Additional experiments are needed to investigate the behavior of JC-1 labeled mitochondria during focusing. For example, red/green ratio distributions obtained in cIEF could be compared to results from the CE method described in Chapter 5 to determine whether polarized mitochondria are detected in cIEF. If only depolarized mitochondria are detected, improvements to prevent the loss of membrane potential during focusing would be necessary. It would be detrimental to the separation to include a substrate such as succinate, as the only way to ensure its presence throughout the entire pH range during focusing and mobilization would be to add it to the catholyte solution, where it would migrate through the capillary toward the anode and act as a chemical mobilizer. One way to address this issue could be to perform the procedure in shorter separation capillaries to minimize the separation time and prevent loss of mitochondrial membrane potential. If JC-1 retention is found to be a problem, other dyes for mitochondrial membrane potential which may be retained longer in depolarized mitochondria could be investigated as alternatives.

In the long term, development of a method to measure individual mitochondrial membrane potential and isoelectric point distributions could shed light on the relationship between these properties. As discussed in the Potential Applications section of Chapter 4, the effect of membrane potential on p*I* is unknown. Experimental data relating membrane potential to p*I* could allow for the estimation of the relative contributions of the amino

acid and phospholipid composition of the mitochondrial outer membrane and mitochondrial membrane potential to mitochondrial surface charge. The model of mitochondrial surface composition described in this chapter could be expanded to include a term for membrane potential, which could be used to make predictions about p*I* changes that might occur with changes to membrane potential and surface composition relevant to aging (e.g. depolarization of mitochondria and ubiquitination of mitochondrial proteins). These predictions could be used to help design methods for better separation of mitochondrial subpopulations.

7.2.2. Mouse Models of Aging

While cell models of aging are useful, characterizing mitochondrial heterogeneity and dysfunction in animal models are important for increased understanding of human aging. The cIEF method described in Chapter 3 could also be applied to mouse models of aging. This method can be used as a tool to characterize heterogeneity in a surface property of mitochondria that relates to their oxidative damage, protein and phospholipid composition, and modification by mitophagy targeting and could possibly be used to separate subpopulations of mitochondria in aging tissue for further characterization of their properties. Mitochondria could be isolated from muscle tissue of young and old mice using a standard technique for mitochondrial isolation of disruption by mechanical homogenization and differential centrifugation (also used in the work described in Chapter 5).[60] These mitochondria could then be labeled with NAO or JC-1 according to the methods described in Chapter 3 or in this chapter and analyzed by cIEF to determine

whether differences in p*I* or membrane potential distributions are present between age groups. It is anticipated that differences are present, since differences in electrophoretic mobility distributions have been observed using CE-LIF between different age groups and by muscle fiber type.[183] Based on these observed differences, it is likely that p*I* will be less acidic (since electrophoretic mobility was less negative) and that more heterogeneity will be observed in aging tissue. Mitochondrial membrane potential is also expected to decrease, but could also be more heterogeneous as damaged mitochondria accumulate in aging tissue and other mitochondria must compensate for their reduced energy output.

Additionally, this method could be applied to different subpopulations of mitochondria isolated from tissue. In muscle, mitochondria are classified as subsarcolemmal (beneath sarcolemma) or intermyofibrillar (between myofibrils) based on their location in the muscle fiber. Differences in fatty acid metabolism,[184] insulin resistance,[185] protein expression,[10] apoptosis signaling,[20] and oxidative damage in the form of carbonylation[186] have been observed between these two subpopulations. Additionally, age-related mitochondrial changes are different between these subpopulations.[187] These subpopulations could be isolated from tissue using a published protocol[10] and subjected separately to cIEF analysis to determine differences in p*I* distributions. The model of mitochondrial surface compositions described in Chapter 4 could be used to interpret differences in these populations. Characterization of the

heterogeneity of surface compositions of these populations could shed light on variations in damage to their surface, protein expression, and targeting for mitophagy.

7.3. Mitochondrial Isolation by Cytoskeleton Disruption and Electroporation

7.3.1. Limitations of Current Methods for Mitochondrial Isolation

Current methods for mitochondrial isolation from cells or tissue have limitations which are detrimental to their use in the characterization of delicate mitochondrial subpopulations such as giant mitochondria. While techniques such as mechanical homogenization[60] or nitrogen cavitation[61] are capable of producing isolated fractions of mitochondria suitable for analysis by CE or cIEF, the choice of technique and how it is applied (e.g. the number or force of strokes in mechanical homogenization or the number of rounds of cavitation) has an effect on the electrophoretic properties of the mitochondria.[62] Moreover, mechanical homogenization disrupts mitochondrial structure and has an effect on mitochondrial function. This technique caused changes in respiration, hydrogen peroxide generation, and the sensitivity of the permeability pore transition to calcium (a measure of apoptosis) when compared to mitochondria which were studied in permeabilized muscle fibers (i.e. not subjected to an isolation technique).[63,64] The authors of these studies hypothesize that mitochondrial membranes are transiently ruptured during homogenization and then re-form in solution to create a mitochondrial suspension with more uniform, spherical morphology than exists in their natural state of a more tubular, interconnected network.[188] While these studies were done

in mitochondria isolated from skeletal muscle, it is logical to assume that similar disruption of membranes could occur in mitochondria isolated from cultured cells as well.

Mitochondrial analysis by CE and cIEF would benefit from a new method which is less disruptive to mitochondrial membranes and has reproducible effects on their electrophoretic properties. While disruption to their native morphology will occur with any isolation technique if mitochondria are reticulated and part of an interconnected network, giant mitochondria are an isolated subpopulation that does not participate in fusion with normal mitochondria[18] and it should be possible to develop a technique which does not disrupt their morphology. The method below describes mitochondrial isolation by disruption of cytoskeleton by colchicine to prevent normal cytoskeleton growth in cell culture and digitonin/trypsin treatment to permeabilize the cell membrane and digest cytoskeletal proteins, followed by delivery of a pulsed electric field (electroporation) to further disrupt the cell. This method should be less harsh than current methods for mitochondrial isolation as it avoids use of shearing forces which disrupt mitochondrial membranes. Mitochondria released by this method have been characterized by fluorescence microscopy and flow cytometry, we propose further characterization by the cIEF method described in Chapter 3 of this work.

7.3.2. Disruption of Cytoskeleton and Electroporation

Mitochondria are anchored to the cellular scaffold of cytoskeletal proteins. These attachments help control mitochondrial morphology, motility, and cellular localization.[38]

Isolation methods to produce preparations of individual mitochondria must disrupt mitochondrial-cytoskeleton interactions. The proposed method utilizes a two-pronged approach to detach mitochondria from cytoskeleton in the cell. Treatment with colchicine in culture prevents polymerization of tubulin (a component of cytoskeleton) via a colchicine-tubulin binding interaction.[189] This disrupts the cytoskeletal network as the cell grows. After the cells are harvested, they are treated with digitonin and trypsin in suspension. Digitonin binds to cholesterol in the cell membrane which disrupts and permeabilizes the membrane, allowing trypsin to enter the cell.[190] Trypsin cleaves proteins C-terminal to lysine and arginine residues,[147] digesting the remaining cytoskeletal proteins attached to mitochondria. The digitonin/trypsin treatment strategy has been used to release mitochondria from single cells for analysis by CE.[88] After disruption of cytoskeletal binding to mitochondria by colchicine treatment in culture followed by digitonin/trypsin treatment of the cell suspension, electric pulses are delivered to the cells to release mitochondria. As pulses are delivered, the cell is disrupted as mitochondria and other cellular components migrate at different rates in the electric field. While research into electroporation as a method to disrupt membranes of organelles using very strong (>10 kV/cm) and very short (<1 μs) electric pulses is a growing field, the strength (350 V/cm) and duration (1-5 ms) of the pulses used for this method is in the region of conventional electroporation, which is used for gene delivery and results in cell survival; minimal or no damage is expected to mitochondria.[191]

Current methods for mitochondrial isolation are inadequate to disrupt their interaction with cytoskeletal proteins, which affect their electrophoretic properties. Previous work investigated cytoskeleton bound to mitochondria isolated by mechanical homogenization.[40] CE-LIF analysis of mitochondria using a probe specific to a cytoskeletal protein revealed that some but not all mitochondria were bound to detectable levels of cytoskeleton, and effects of this cytoskeleton binding on electrophoretic mobility distributions were observed. Mitochondria were "shaved' of bound cytoskeleton by treatment with the protease trypsin, this treatment also resulted in differences in electrophoretic mobility distributions. This work suggests that a method to disrupt cytoskeletal binding to isolated mitochondria is important for their isolation from the cell for analysis of their electrophoretic properties.

Mitochondrial release by digitonin/trypsin treatment combined with electroporation was demonstrated, shown in Figure 7-5 below. This data demonstrates that mitochondria are released from the cell membrane by this technique and remain intact. In this experiment, electric pulses were applied before digitonin/trypsin treatment to aid delivery of trypsin into the cell.

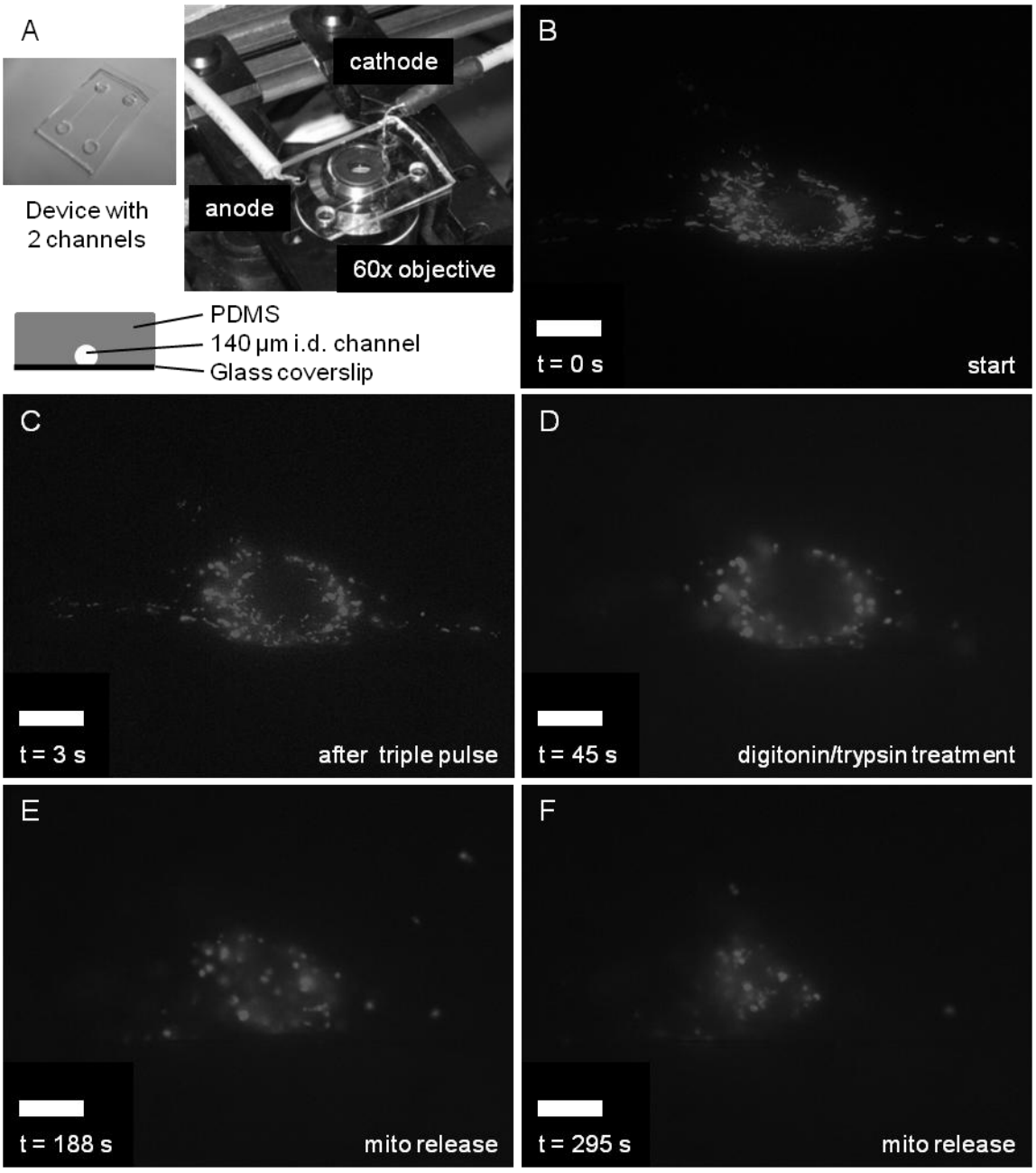

Figure 7-5. Mitochondria released by application of electric field and digitonin/trypsin treatment. (A) Microchannel chamber device used to deliver electric pulses. (B) Single cell adhered to microchannel before pulse delivery. (C) Cell after three ~0.5 pulses of 200 V/cm (cathode positioned on left side of image). Some disruption of the cell occurs, mitochondria remain intact, demonstrated by retention of soluble DsRed2 fluorescent fusion protein inside the mitochondrial matrix.

(Figure 7-5, continued) (D) Addition of 6 µg/mL digitonin (Calbiochem, San Diego, CA) and 750 µg/mL trypsin (Invitrogen) in buffer SH (see section 5.2.2 in Chapter 5 for composition) begins cell membrane permeabilization and cytoskeleton cleavage. (E) Mitochondria are released after incubation with digitonin/trypsin. Mitochondria are outside of the cell and remain intact. Mitochondrial movement is due to diffusion and slight hydrodynamic flow in microchannel induced by height difference between inlet and outlet reservoirs. (F) Continued release of mitochondria. Mitochondria drift out of the cell and out of the focal plane. Mitochondria in L6 rat myoblast cell visualized by expression of DsRed2 fusion protein with mitochondrial targeting sequence (Clonetech, Mountain View, CA, see the procedure in Kostal and Arriaga[40] for cell culture and transfection details). After transfection, cells were harvested and delivered into a 140 µm i.d. cylindrical microchannel fabricated in polydimethylsiloxane (PDMS, Sylgard 184 kit was from Dow Corning, Midland, MI and was used according to the manufacturer's instructions). Microchannels were fabricated using a 20 mm long fused silica capillary (Polymicro, Pheonix, AZ) attached to a glass slide by application of a spot of epoxy at each end as a mold. PDMS prepolymer solution was cast over the mold as a thin film (~5 mm film thickness) and allowed to cure. After curing, the PDMS film was removed from the mold, inlet and outlet reservoirs (~5 mm diameter) were punched through the film at each end of the channel, and the channel was applied to a glass microscope coverslip. Microchannels were coated with poly-L-lysine before use to improve cell adhesion (Sigma-Aldrich, Saint Louis, MO). Cells were allowed to attach overnight in DMEM with 10% FBS, 100 IU/mL penicillin, and 100 µg/mL streptomycin (cell culture reagents from Invitrogen). DMEM was exchanged with buffer SH before imaging. The electric field was applied by manually controlling a Spellman CZE 1000 high voltage power supply (Plainview, NY) connected to platinum electrodes placed in the inlet and outlet reservoirs. Scale bar = 10 µm. Images acquired using Olympus IX81 inverted fluorescence microscope (Melville, NY) equipped with a 120W mercury lamp, DS-IX100 disk spinning unit, 60x oil immersion objective (NA = 1.45), RFP filter cube (λ_{ex} = 545 ± 10 nm, λ_{em} = 597.5 ± 27.5 nm, 565 nm dichroic, Olympus M-RFPHQ filter cube) and C9100-01 EM CCD camera (Hamamatsu, Bridgewater, NJ). This experiment was performed by Dr. Vratislav Kostal.

The experiment shown in Figure 7-6 below demonstrates the migration of mitochondria out of the cell in the electric field. This result demonstrates that mitochondria remain intact and are not damaged by the electric field after they are released from the cell. These experiments should be repeated with colchicine treatment of the cells to compare the effects of disruption of cytoskeleton in culture on the observed mitochondrial morphology and disruption of the cell by this method. Additionally, the CE-LIF method for determination of cytoskeletal binding to mitochondria described above should be used for additional validation that this method disrupts the binding between mitochondria and cytoskeleton.[40]

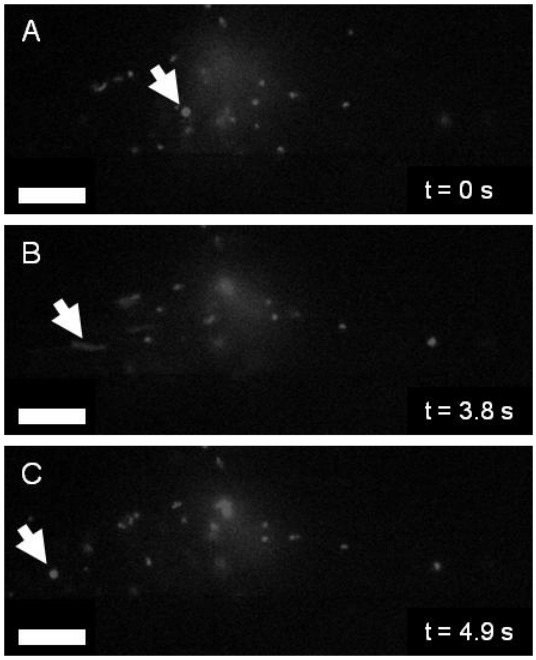

Figure 7-6. Mitochondrial migration out of cell in applied electric field. (A) Cell treated with digitonin/trypsin before electric field pulses were applied. (B) During application of a pulse (~0.5 s, 200 V/cm, cathode at left of image), single mitochondrion is moving and appears as streak. (C) After several pulses, mitochondrion is intact and outside of the cell. All experimental conditions as described in Figure 7-5. This experiment was performed by Dr. Vratislav Kostal.

Flow cytometry was used to characterize the size distributions of mitochondria released from L6 rat myoblasts transfected with ATG7-siRNA for 24 h and control cells. A mitochondrial-specific dye, MitoTracker Red, was used to label mitochondria. This probe was chosen to allow for dual labeling using a cytoskeleton-specific probe conjugated to a green fluorophore (data not shown). The flow cytometry results shown in Figure 7-7 below suggest that mitochondria isolated from ATG7-siRNA treated cells are larger than those from control cells, suggesting that this method is appropriate for isolation of giant mitochondria. However, flow cytometry has modest sensitivity for detection of individual organelles and may miss subpopulations. Additional characterization of the mitochondria released by this method is needed.

One limitation of the previous work was the reproducibility of pulse delivery. In the imaging experiments described in Figures 7-5 and 7-6, pulses were delivered manually with no precise control over their duration. In the experiment described in Figure 7-7, more control over pulse duration was possible, but pulse spacing was still controlled manually. An improved instrument, the Bio-Rad Gene Pulser Xcell, will be used for the future experiments. This instrument is capable of faster, automated pulse delivery, delivering 60 square wave pulses of 350 V/cm and 5 ms duration in under two minutes, which should increase the reproducibility of this technique.

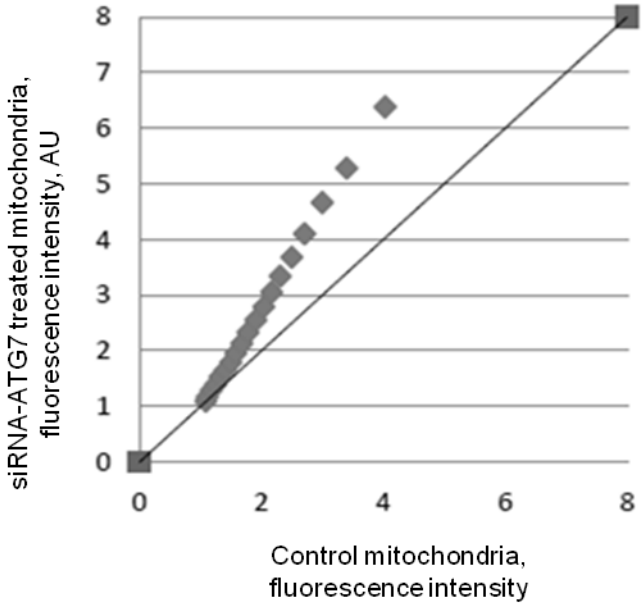

Figure 7-7. Q-Q plot of fluorescence intensity distributions measured by flow cytometry of ATG7 siRNA-treated cells vs. control cells. Culture conditions for L6 cells were as described in Chapter 3. The cells were treated with 14 µM colchicine for 15 h, cells were harvested with trypsin (Invitrogen) and washed with phosphate-buffered saline (Invitrogen), then mitochondria were labeled by suspending the cells with 250 nM MitoTracker Red (Molecular Probes, Eugene, OR) for 45 min at 37 °C in mitochondrial isolation buffer (see Chapter 3 for composition and suppliers). After labeling, cells were washed and mitochondria were isolated via digitonin/trypsin treatment (0.03 µM digitonin and 0.08 µM trypsin for 20 min at 4 °C) and electroporation. Cells were disrupted using a Gene Pulser II electroporator (Bio-Rad, Hercules, CA). Exponential decay pulses were delivered at 350 V/cm at 25 µF, with time constants ranging from 1.9 to 2.8 ms. Data collected with a FACS ExCalibur 501 Bench Top flow cytometer (Becton and Dickinson, San Jose, CA). Excitation: 488 nm Ar^+ laser. FL2 emission filter (585/42 nm). 10000 events per sample detected using the "Low" setting, fluorescence intensities plotted on a logarithmic scale. Gating was used in FL and side scatter plots to define an exclusion region for whole cells present in the preparation. This experiment was performed by Scott Rose.

7.3.3. cIEF of Mitochondria Isolated by Cytoskeletal Disruption and Electroporation

Ultimately, development of a method compatible with isolation of giant mitochondria from cell models of aging will make it possible to characterize these organelles using the methods described in this thesis. The cIEF method described in Chapter 3, with improvements described in section 7-1 above, can be used to characterize mitochondria from ATG7-siRNA treated cells and untreated control cells released by colchicine/digitonin/trypsin treatment and electroporation. Characterization of these samples using cIEF will test the hypothesis that giant mitochondria have different p*I*s based on differences in their surface properties. An additional technique should be used to confirm that mitochondrial isolation by cytoskeletal disruption and electroporation is a suitable technique for analysis of giant mitochondria. Besides being subjected to analysis by cIEF, these preparations can be characterized by transmission electron microscopy (TEM) to examine morphological differences in the mitochondria released by this technique if the amount of sample permits (i.e. conventional preparation for TEM requires a pellet after centrifugation of the mitochondria). Isolated mitochondria prepared by a conventional method (i.e. mechanical homogenization as described in Chapter 3) can also be used to prepare samples for comparison by cIEF and TEM to investigate the differences in sample preparation methods on the electrophoretic and morphological properties of isolated mitochondria.

Analysis of giant mitochondria in aging models requires development of the method for mitochondrial isolation described in this section. This method can be validated by TEM and the CE-LIF method for quantitation of cytoskeletal binding to mitochondria, as described above. This method would be a valuable tool in the analysis of mitochondrial heterogeneity as it would allow for analysis of delicate mitochondrial subpopulations which may not survive traditional isolation techniques. Moreover, this method would enable detection of differences in the p*I* distributions of mitochondrial preparations from cells with inhibited autophagy vs. untreated cells which could not be observed using current methods for mitochondrial isolation. Ultimately, determination of differences in p*I* could lead to a method for the preparative separation of giant and normal mitochondria, which would enable further characterization to elucidate their role in the aging process.

7.3.4. Separations for Proteomics

If application of the techniques described in this chapter to aging models reveal subpopulations of mitochondria with different p*I*s, this could be used as a basis for separation of these subpopulations for analysis by mass spectrometry-based proteomics. This field encompasses a broad array of techniques whose ultimate goal is to identify and quantify all the proteins in a biological system.

Since cIEF is not a preparative technique, scaling up the separation to produce different mitochondrial fractions separated by p*I* would be necessary to provide sufficient sample for a proteomics experiment. This can be achieved by translating the separation

from the capillary to the free-flow electrophoresis format. Free-flow isoelectric focusing is a powerful method to separate analytes by p*I* and which allows for continuous collection of fractions.[77] Free-flow electrophoresis techniques have been widely applied to preparation of protein or organelle fractions for analysis by proteomics.[192] This technique has been adapted to the microchip format and applied to separations of mitochondria.[59] One caveat is that the resolving power of this technique does not match that of cIEF, so differences in the p*I* of subpopulations of interest would need to be at least 0.25 pH units apart (the resolving power demonstrated in a recently described device for free-flow isoelectric focusing).[193] An additional limitation in the use of isoelectric focusing for proteomics sample preparation is that carrier ampholytes can be detrimental identification of molecules by mass spectrometry. The large number of compounds present in carrier ampholytes mixtures can result in noisy spectra which makes detection of peptides and small molecules difficult. A new strategy using a mixture of six amino acids to establish the pH gradient in cIEF addresses this issue.[194] This strategy could be adapted to establish the pH gradient in a preparative microfluidic device.

Strategies for future proteomics experiments would depend on the source of mitochondria. If cell models are used, stable isotope labeling by amino acids in cell culture (SILAC) is an established technique that can provide excellent relative quantitation of proteins between samples.[195] For animal models, isobaric tags for the relative quantitation of peptides (iTRAQ),[196] super-SILAC,[197] or stable isotope labeling

of mammals (SILAM)[198] could be used depending on the resources available. These techniques achieve protein quantitation by labeling at the peptide level (iTRAQ), by comparison to an isotopically-labeled spike-in standard (super-SILAC), or by isotopic labeling of the entire animal at the protein level (SILAM). A standard protocol of in-gel digestion and peptide extraction could be used for sample preparation,[199] although if sample sizes are limited, in-solution digestion could be performed. A high-performance liquid chromatography separation of peptides coupled to an Orbitrap-family mass spectrometer (Thermo) is the gold standard for mass-spectrometry based proteomics.

Characterization of mitochondrial subpopulations by these techniques could result in discovery of new biomarkers for age-related diseases (i.e. proteins that are up- or down-regulated in a specific disease that could be used for identification or earlier diagnosis). Additionally, the ability to determine quantitative changes in specific proteins in these subpopulations could shed light on the molecular mechanisms involved in aging.

7.3.5. Application to Other Organelles

Analysis of other organelles by the methods described in this chapter could shed light on the heterogeneity in other organelle populations, reveal subpopulations with different functional characteristics, and provide additional insight into a myriad of cellular processes. As long as an appropriate fluorescent labeling strategy exists, preparations of any organelle of interest could be characterized by the cIEF technique described in this thesis. For an extensive list of organelle-specific antibodies, synthetic probes, and fluorescent proteins that can be targeted to organelles, see the recent review

by Satori et al.[48] Cytoskeletal-organelle connections are not limited to mitochondria – the method for mitochondrial isolation by disruption of cytoskeleton and electroporation could provide a valuable tool for preparation of fractions of other difficult-to-isolate or delicate organelles. Determination of p*I* distributions of other individual organelles by the cIEF method described in Chapter 3 could lead to new insights into their surface composition by application of the modeling method described in Chapter 4 of this work. Detection of subpopulations with different p*I* could lead to preparative separations to prepare enriched fractions for analysis by proteomics. These future applications could represent important advances in our understanding of subcellular heterogeneity.

Bibliography

(1) World Health Organization, US National Institute of Aging, 2011.
(2) Harman, D. Aging - a theory based on free-radical and radiation-chemistry. *J Gerontol* **1956**, *11*, 298-300.
(3) Balaban, R. S.; Nemoto, S.; Finkel, T. Mitochondria, oxidants, and aging. *Cell* **2005**, *120*, 483-495.
(4) Speakman, J. R.; Selman, C. The free-radical damage theory: Accumulating evidence against a simple link of oxidative stress to ageing and lifespan. *Bioessays* **2011**, *33*, 255-259.
(5) Brunk, U. T.; Terman, A. The mitochondrial-lysosomal axis theory of aging - Accumulation of damaged mitochondria as a result of imperfect autophagocytosis. *Eur J Biochem* **2002**, *269*, 1996-2002.
(6) Terman, A.; Gustafsson, B.; Brunk, U. T. The lysosomal-mitochondrial axis theory of postmitotic aging and cell death. *Chem-Biol Interact* **2006**, *163*, 29-37.
(7) Terman, A.; Kurz, T.; Navratil, M.; Arriaga, E. A.; Brunk, U. T. Mitochondrial Turnover and Aging of Long-Lived Postmitotic Cells: The Mitochondrial-Lysosomal Axis Theory of Aging. *Antioxid Redox Sign* **2010**, *12*, 503-535.
(8) Kuznetsov, A. V.; Margreiter, R. Heterogeneity of Mitochondria and Mitochondrial Function within Cells as Another Level of Mitochondrial Complexity. *International Journal of Molecular Sciences* **2009**, *10*, 1911-1929.
(9) Galloway, C. A.; Lee, H.; Yoon, Y. Mitochondrial morphology-emerging role in bioenergetics. *Free Radical Bio Med* **2012**, *53*, 2218-2228.
(10) Ferreira, R.; Vitorino, R.; Alves, R. M. P.; Appell, H. J.; Powers, S. K.; Duarte, J. A.; Amado, F. Subsarcolemmal and intermyofibrillar mitochondria proteome differences disclose functional specializations in skeletal muscle. *Proteomics* **2010**, *10*, 3142-3154.
(11) Twig, G.; Elorza, A.; Molina, A. J. A.; Mohamed, H.; Wikstrom, J. D.; Walzer, G.; Stiles, L.; Haigh, S. E.; Katz, S.; Las, G.; Alroy, J.; Wu, M.; Py, B. F.; Yuan, J.; Deeney, J. T.; Corkey, B. E.; Shirihai, O. S. Fission and selective fusion govern mitochondrial segregation and elimination by autophagy. *Embo J.* **2008**, *27*, 433-446.
(12) Youle, R. J.; van der Bliek, A. M. Mitochondrial Fission, Fusion, and Stress. *Science* **2012**, *337*, 1062-1065.
(13) Green, D. R.; Galluzzi, L.; Kroemer, G. Mitochondria and the Autophagy-Inflammation-Cell Death Axis in Organismal Aging. *Science* **2011**, *333*, 1109-1112.
(14) Tauchi, H.; Sato, T. Age Changes in Size and Number of Mitochondria of Human Hepatic Cells. *J Gerontol* **1968**, *23*, 454-&.
(15) Sato, T.; Tauchi, H. Formation of Enlarged and Giant Mitochondria in Aging Process of Human Hepatic Cells. *Acta Pathol Japon* **1975**, *25*, 403-412.
(16) Sachs, H. G.; Colgan, J. A.; Lazarus, M. L. Ultrastructure of Aging Myocardium - Morphometric Approach. *Am J Anat* **1977**, *150*, 63-71.

(17) Terman, A.; Dalen, H.; Eaton, J. W.; Neuzil, J.; Brunk, U. T. Mitochondrial recycling and aging of cardiac myocytes: the role of autophagocytosis. *Exp Gerontol* **2003**, *38*, 863-876.
(18) Navratil, M.; Terman, A.; Arriaga, E. A. Giant mitochondria do not fuse and exchange their contents with normal mitochondria. *Exp Cell Res* **2008**, *314*, 164-172.
(19) Keil, V. C.; Funke, F.; Zeug, A.; Schild, D.; Muller, M. Ratiometric high-resolution imaging of JC-1 fluorescence reveals the subcellular heterogeneity of astrocytic mitochondria. *Pflugers Archiv-European Journal of Physiology* **2011**, *462*, 693-708.
(20) Adhihetty, P. J.; Ljubicic, V.; Menzies, K. J.; Hood, D. A. Differential susceptibility of subsarcolemmal and intermyofibrillar mitochondria to apoptotic stimuli. *Am. J. Physiol.-Cell Physiol.* **2005**, *289*, C994-C1001.
(21) Galloway, C. A.; Lee, H.; Nejjar, S.; Jhun, B. S.; Yu, T. Z.; Hsu, W.; Yoon, Y. Transgenic Control of Mitochondrial Fission Induces Mitochondrial Uncoupling and Relieves Diabetic Oxidative Stress. *Diabetes* **2012**, *61*, 2093-2104.
(22) Narendra, D.; Tanaka, A.; Suen, D. F.; Youle, R. J. Parkin is recruited selectively to impaired mitochondria and promotes their autophagy. *J. Cell Biol.* **2008**, *183*, 795-803.
(23) Chen, H. C.; Chomyn, A.; Chan, D. C. Disruption of fusion results in mitochondrial heterogeneity and dysfunction. *J Biol Chem* **2005**, *280*, 26185-26192.
(24) Youle, R. J.; Narendra, D. P. Mechanisms of mitophagy. *Nat Rev Mol Cell Bio* **2011**, *12*, 9-14.
(25) Gomes, L. C.; Scorrano, L. Mitochondrial morphology in mitophagy and macroautophagy. *Biochim. Biophys. Acta-Mol. Cell Res.* **2013**, *1833*, 205-212.
(26) Green, D. R.; Reed, J. C. Mitochondria and apoptosis. *Science* **1998**, *281*, 1309-1312.
(27) Twig, G.; Hyde, B.; Shirihai, O. S. Mitochondrial fusion, fission and autophagy as a quality control axis: The bioenergetic view. *Bba-Bioenergetics* **2008**, *1777*, 1092-1097.
(28) Short, K. R.; Bigelow, M. L.; Kahl, J.; Singh, R.; Coenen-Schimke, J.; Raghavakaimal, S.; Nair, K. S. Decline in skeletal muscle mitochondrial function with aging in humans. *P Natl Acad Sci USA* **2005**, *102*, 5618-5623.
(29) Brownlee, M. Biochemistry and molecular cell biology of diabetic complications. *Nature* **2001**, *414*, 813-820.
(30) Vanneste, J.; Deaguilar, P. V. Mitochondrial Alterations in the Spinal Ganglion Neurons in Aging Rats. *Acta Neuropathol* **1981**, *54*, 83-87.
(31) Vincow, E. S.; Merrihew, G.; Thomas, R. E.; Shulman, N. J.; Beyer, R. P.; MacCoss, M. J.; Pallanck, L. J. The PINK1-Parkin pathway promotes both mitophagy and selective respiratory chain turnover in vivo. *P Natl Acad Sci USA* **2013**, *110*, 6400-6405.
(32) Gegg, M. E.; Cooper, J. M.; Chau, K. Y.; Rojo, M.; Schapira, A. H. V.; Taanman, J. W. Mitofusin 1 and mitofusin 2 are ubiquitinated in a PINK1/parkin-dependent manner upon induction of mitophagy. *Hum. Mol. Genet.* **2010**, *19*, 4861-4870.

(33) Poole, A. C.; Thomas, R. E.; Andrews, L. A.; McBride, H. M.; Whitworth, A. J.; Pallanck, L. J. The PINK1/Parkin pathway regulates mitochondrial morphology. *P Natl Acad Sci USA* **2008**, *105*, 1638-1643.
(34) Ishihara, N.; Jofuku, A.; Eura, Y.; Mihara, K. Regulation of mitochondrial morphology by membrane potential, and DRP1-dependent division and FZO1-dependent fusion reaction in mammalian cells. *Biochem. Biophys. Res. Commun.* **2003**, *301*, 891-898.
(35) Matsuda, N.; Sato, S.; Shiba, K.; Okatsu, K.; Saisho, K.; Gautier, C. A.; Sou, Y.; Saiki, S.; Kawajiri, S.; Sato, F.; Kimura, M.; Komatsu, M.; Hattori, N.; Tanaka, K. PINK1 stabilized by mitochondrial depolarization recruits Parkin to damaged mitochondria and activates latent Parkin for mitophagy. *J. Cell Biol.* **2010**, *189*, 211-221.
(36) Lecoeur, H.; Langonne, A.; Baux, L.; Rebouillat, D.; Rustin, P.; Prevost, M. C.; Brenner, C.; Edelman, L.; Jacotot, E. Real-time flow cytometry analysis of permeability transition in isolated mitochondria. *Exp Cell Res* **2004**, *294*, 106-117.
(37) Huttemann, M.; Lee, I.; Pecinova, A.; Pecina, P.; Przyklenk, K.; Doan, J. W. Regulation of oxidative phosphorylation, the mitochondrial membrane potential, and their role in human disease. *J Bioenerg Biomembr* **2008**, *40*, 445-456.
(38) Boldogh, I. R.; Pon, L. A. Mitochondria on the move. *Trends Cell Biol.* **2007**, *17*, 502-510.
(39) Anesti, V.; Scorrano, L. The relationship between mitochondrial shape and function and the cytoskeleton. *Biochim. Biophys. Acta-Bioenerg.* **2006**, *1757*, 692-699.
(40) Kostal, V.; Arriaga, E. A. Capillary Electrophoretic Analysis Reveals Subcellular Binding between Individual Mitochondria and Cytoskeleton. *Anal Chem* **2011**, *83*, 1822-1829.
(41) Cottet-Rousselle, C.; Ronot, X.; Leverve, X.; Mayol, J. F. Cytometric Assessment of Mitochondria Using Fluorescent Probes. *Cytom. Part A* **2011**, *79A*, 405-425.
(42) Zand, K.; Pham, T.; Davila, A.; Wallace, D. C.; Burke, P. J. Nanofluidic Platform for Single Mitochondria Analysis Using Fluorescence Microscopy. *Anal Chem* **2013**, *85*, 6018-6025.
(43) Suraniti, E.; Vajrala, V. S.; Goudeau, B.; Bottari, S. P.; Rigoulet, M.; Devin, A.; Sojic, N.; Arbault, S. Monitoring Metabolic Responses of Single Mitochondria within Poly(dimethylsiloxane) Wells: Study of Their Endogenous Reduced Nicotinamide Adenine Dinucleotide Evolution. *Anal Chem* **2013**, *85*, 5146-5152.
(44) Poot, M.; Zhang, Y. Z.; Krämer, J. A.; Wells, K. S.; Jones, L. J.; Hanzel, D. K.; Lugade, A. G.; Singer, V. L.; Haugland, R. P. Analysis of mitochondrial morphology and function with novel fixable fluorescent stains. *Journal of Histochemistry & Cytochemistry* **1996**, *44*, 1363-72.
(45) Maftah, A.; Petit, J. M.; Ratinaud, M.-H.; Julien, R. 10-N Nonyl-Acridine Orange: A fluorescent probe which stains mitochondria independently of their energetic state. *Biochem. Biophys. Res. Commun.* **1989**, *164*, 185-190.

(46) Zielonka, J.; Vasquez-Vivar, J.; Kalyanaraman, B. Detection of 2-hydroxyethidium in cellular systems: a unique marker product of superoxide and hydroethidine. *Nat. Protocols* **2008**, *3*, 8-21.
(47) Llopis, J.; McCaffery, J. M.; Miyawaki, A.; Farquhar, M. G.; Tsien, R. Y. Measurement of cytosolic, mitochondrial, and Golgi pH in single living cells with green fluorescent proteins. *P Natl Acad Sci USA* **1998**, *95*, 6803-6808.
(48) Satori, C. P.; Henderson, M. M.; Krautkramer, E. A.; Kostal, V.; Distefano, M. M.; Arriaga, E. A. Bioanalysis of Eukaryotic Organelles. *Chem Rev* **2013**, *113*, 2733-2811.
(49) Fritzky, L.; Lagunoff, D. Advanced methods in fluorescence microscopy. *Anal. Cell. Pathol.* **2013**, *36*, 5-17.
(50) Labajova, A.; Vojtiskova, A.; Krivakova, P.; Kofranek, J.; Drahota, Z.; Houstek, J. Evaluation of mitochondrial membrane potential using a computerized device with a tetraphenylphosphonium-selective electrode. *Anal Biochem* **2006**, *353*, 37-42.
(51) Lim, T. S.; Davila, A.; Wallace, D. C.; Burke, P. Assessment of mitochondrial membrane potential using an on-chip microelectrode in a microfluidic device. *Lab Chip* **2010**, *10*, 1683-1688.
(52) Lim, T. S.; Davila, A.; Zand, K.; Wallace, D. C.; Burke, P. J. Wafer-scale mitochondrial membrane potential assays. *Lab on a Chip* **2012**, *12*, 2719-2725.
(53) Perry, S. W.; Norman, J. P.; Barbieri, J.; Brown, E. B.; Gelbard, H. A. Mitochondrial membrane potential probes and the proton gradient: a practical usage guide. *Biotechniques* **2011**, *50*, 98-+.
(54) Ehrenberg, B.; Montana, V.; Wei, M. D.; Wuskell, J. P.; Loew, L. M. Membrane-Potential Can Be Determined in Individual Cells from the Nernstian Distribution of Cationic Dyes. *Biophys. J.* **1988**, *53*, 785-794.
(55) Broder, J.; Majumder, A.; Porter, E.; Srinivasamoorthy, G.; Keith, C.; Lauderdale, J.; Sornborger, A. Estimating weak ratiometric signals in imaging data. I. Dual-channel data. *J. Opt. Soc. Am. A-Opt. Image Sci. Vis.* **2007**, *24*, 2921-2931.
(56) Smiley, S. T.; Reers, M.; Mottolahartshorn, C.; Lin, M.; Chen, A.; Smith, T. W.; Steele, G. D.; Chen, L. B. Intracellular Heterogeneity in Mitochondrial-Membrane Potentials Revealed by a J-Aggregate-Forming Lipophilic Cation Jc-1. *P Natl Acad Sci USA* **1991**, *88*, 3671-3675.
(57) Cossarizza, A.; Ceccarelli, D.; Masini, A. Functional heterogeneity of an isolated mitochondrial population revealed by cytofluorometric analysis at the single organelle level. *Exp Cell Res* **1996**, *222*, 84-94.
(58) Perelman, A.; Wachtel, C.; Cohen, M.; Haupt, S.; Shapiro, H.; Tzur, A. JC-1: alternative excitation wavelengths facilitate mitochondrial membrane potential cytometry. *Cell Death Dis.* **2012**, *3*.
(59) Lu, H.; Gaudet, S.; Schmidt, M. A.; Jensen, K. F. A microfabricated device for subcellular organelle sorting. *Anal Chem* **2004**, *76*, 5705-5712.
(60) Frezza, C.; Cipolat, S.; Scorrano, L. Organelle isolation: functional mitochondria from mouse liver, muscle and cultured filroblasts. *Nat Protoc* **2007**, *2*, 287-295.

(61) Gross, V. S.; Greenberg, H. K.; Baranov, S. V.; Carlson, G. M.; Stavrovskaya, I. G.; Lazarev, A. V.; Kristal, B. S. Isolation of functional mitochondria from rat kidney and skeletal muscle without manual homogenization. *Anal Biochem* **2011**, *418*, 213-223.
(62) Fuller, K. M.; Arriaga, E. A. Capillary electrophoresis monitors changes in the electrophoretic behavior of mitochondrial preparations. *J Chromatogr B* **2004**, *806*, 151-159.
(63) Picard, M.; Ritchie, D.; Wright, K. J.; Romestaing, C.; Thomas, M. M.; Rowan, S. L.; Taivassalo, T.; Hepple, R. T. Mitochondrial functional impairment with aging is exaggerated in isolated mitochondria compared to permeabilized myofibers. *Aging Cell* **2010**, *9*, 1032-1046.
(64) Picard, M.; Taivassalo, T.; Ritchie, D.; Wright, K. J.; Thomas, M. M.; Romestaing, C.; Hepple, R. T. Mitochondrial Structure and Function Are Disrupted by Standard Isolation Methods. *PLoS One* **2011**, *6*.
(65) Poe, B. G.; Navratil, M.; Arriaga, E. A. Analysis of subcellular sized particles - Capillary electrophoresis with post-column laser-induced fluorescence detection versus flow cytometry. *J Chromatogr A* **2006**, *1137*, 249-255.
(66) Saunders, J. E.; Beeson, C. C.; Schnellmann, R. G. Characterization of functionally distinct mitochondrial subpopulations. *J Bioenerg Biomembr* **2013**, *45*, 87-99.
(67) Cormack, B. P.; Valdivia, R. H.; Falkow, S. FACS-optimized mutants of the green fluorescent protein (GFP). *Gene* **1996**, *173*, 33-38.
(68) Schiro, P. G.; Gadd, J. C.; Yen, G. S.; Chiu, D. T. High-Throughput Fluorescence-Activated Nanoscale Subcellular Sorter with Single-Molecule Sensitivity. *The Journal of Physical Chemistry B* **2012**, *116*, 10490-10495.
(69) Giddings, J. C. Field-Flow Fractionation - Analysis of Macromolecular, Colloidal, and Particulate Materials. *Science* **1993**, *260*, 1456-1465.
(70) Mozersky, S. M.; Caldwell, K. D.; Jones, S. B.; Maleeff, B. E.; Barford, R. A. Sedimentation Field Flow Fractionation of Mitochondrial and Microsomal-Membranes from Corn Roots. *Anal Biochem* **1988**, *172*, 113-123.
(71) Kang, D.; Oh, S.; Reschiglian, P.; Moon, M. H. Separation of mitochondria by flow field-flow fractionation for proteomic analysis. *Analyst* **2008**, *133*, 505-515.
(72) Battu, S.; Cook-Moreau, J.; Cardot, P. J. P. Sedimentation field-flow fractionation: Methodological basis and applications for cell sorting. *J Liq Chromatogr R T* **2002**, *25*, 2193-2210.
(73) Roman, M. C.; Brown, P. R. Free-Flow Electrophoresis. *Anal Chem* **1994**, *66*, A86-A94.
(74) Krivankova, L.; Bocek, P. Continuous free-flow electrophoresis. *Electrophoresis* **1998**, *19*, 1064-1074.
(75) Zischka, H.; Braun, R. J.; Marantidis, E. P.; Buringer, D.; Bornhovd, C.; Hauck, S. M.; Demmer, O.; Gloeckner, C. J.; Reichert, A. S.; Madeo, F.; Ueffing, M. Differential analysis of Saccharomyces cerevisiae mitochondria by free flow electrophoresis. *Mol Cell Proteomics* **2006**, *5*, 2185-2200.

(76) Heidrich, H.-G.; Stahn, R.; Hannig, K. The surface charge of rat liver mitochondria and their membranes: Clarification of Some Controversies Concerning Mitochondrial Structure. *The Journal of Cell Biology* **1970**, *46*, 137-150.
(77) Turgeon, R. T.; Bowser, M. T. Micro free-flow electrophoresis: theory and applications. *Anal Bioanal Chem* **2009**, *394*, 187-198.
(78) Kostal, V.; Fonslow, B. R.; Arriaga, E. A.; Bowser, M. T. Fast Determination of Mitochondria Electrophoretic Mobility Using Micro Free-Flow Electrophoresis. *Anal Chem* **2009**, *81*, 9267-9273.
(79) Pysher, M. D.; Hayes, M. A. Effects of deformability, uneven surface charge distributions, and multipole moments on biocolloid electrophoretic migration. *Langmuir* **2005**, *21*, 3572-3577.
(80) Pysher, M. D.; Hayes, M. A. Examination of the electrophoretic behavior of liposomes. *Langmuir* **2004**, *20*, 4369-4375.
(81) Chen, S. B. Electrophoretic mobility of a spherical liposome. *J. Colloid Interface Sci.* **2010**, *348*, 177-182.
(82) Chen, Y.; Arriaga, E. A. Individual electrophoretic mobilities of liposomes and acidic organelles displaying pH gradients across their membranes. *Langmuir* **2007**, *23*, 5584-5590.
(83) Hjerten, S.; Zhu, M. D. Adaptation of the Equipment for High-Performance Electrophoresis to Isoelectric-Focusing. *J Chromatogr* **1985**, *346*, 265-270.
(84) Subirats, X.; Blaas, D.; Kenndler, E. Recent developments in capillary and chip electrophoresis of bioparticles: Viruses, organelles, and cells. *Electrophoresis* **2011**, *32*, 1579-1590.
(85) Kostal, V.; Arriaga, E. A. Recent advances in the analysis of biological particles by capillary electrophoresis. *Electrophoresis* **2008**, *29*, 2578-2586.
(86) Duffy, C. F.; Fuller, K. M.; Malvey, M. W.; O'Kennedy, R.; Arriaga, E. A. Determination of electrophoretic mobility distributions through the analysis of individual mitochondrial events by capillary electrophoresis with laser-induced fluorescence detection. *Anal Chem* **2002**, *74*, 171-176.
(87) Fuller, K. M.; Duffy, C. F.; Arriaga, E. A. Determination of the cardiolipin content of individual mitochondria by capillary electrophoresis with laser-induced fluorescence detection. *Electrophoresis* **2002**, *23*, 1571-1576.
(88) Johnson, R. D.; Navratil, M.; Poe, B. G.; Xiong, G. H.; Olson, K. J.; Ahmadzadeh, H.; Andreyev, D.; Duffy, C. F.; Arriaga, E. A. Analysis of mitochondria isolated from single cells. *Anal Bioanal Chem* **2007**, *387*, 107-118.
(89) Ahmadzadeh, H.; Thompson, L. V.; Arriaga, E. A. On-column labeling for capillary electrophoretic analysis of individual mitochondria directly sampled from tissue cross sections. *Anal Bioanal Chem* **2006**, *384*, 169-174.
(90) Navratil, M.; Poe, B. G.; Arriaga, E. A. Quantitation of DNA copy number in individual mitochondrial particles by capillary electrophoresis. *Anal Chem* **2007**, *79*, 7691-7699.

(91) Allen, P. B.; Doepker, B. R.; Chiu, D. T. High-Throughput Capillary-Electrophoresis Analysis of the Contents of a Single Mitochondria. *Anal Chem* **2009**, *81*, 3784-3791.
(92) Moore, A. W.; Jorgenson, J. W. Study of Zone Broadening in Optically Gated High-Speed Capillary Electrophoresis. *Anal Chem* **1993**, *65*, 3550-3560.
(93) Henley, W. H.; Jorgenson, J. W. Ultra-high voltage capillary electrophoresis > 300 kV: Recent advances in instrumentation and analyte detection. *J Chromatogr A* **2012**, *1261*, 171-178.
(94) Plenert, M. L.; Shear, J. B. Microsecond electrophoresis. *P Natl Acad Sci USA* **2003**, *100*, 3853-3857.
(95) Henley, T. H.; Wilburn, R. T.; Crouch, A. M.; Jorgenson, J. W. Flow counterbalanced capillary electrophoresis using packed capillary columns: Resolution of enantiomers and isotopomers. *Anal Chem* **2005**, *77*, 7024-7031.
(96) Shimura, K.; Waki, T.; Okada, M.; Toda, T.; Kimoto, I.; Kasai, K. Analysis of protein-protein interactions with a multi-capillary electrophoresis instrument. *Electrophoresis* **2006**, *27*, 1886-1894.
(97) Liu, Z.; Pawliszyn, J. Capillary isoelectric focusing of proteins with liquid core waveguide laser-induced fluorescence whole column imaging detection. *Anal Chem* **2003**, *75*, 4887-4894.
(98) Kappes, T.; Hauser, P. C. Electrochemical detection methods in capillary electrophoresis and applications to inorganic species. *J Chromatogr A* **1999**, *834*, 89-101.
(99) Chen, D. Y.; Dovichi, N. J. Yoctomole detection limit by laser-induced fluorescence in capillary electrophoresis. *J. Chromatogr. B-Biomed. Appl.* **1994**, *657*, 265-269.
(100) Kleparnik, K. Recent advances in the combination of capillary electrophoresis with mass spectrometry: From element to single-cell analysis. *Electrophoresis* **2013**, *34*, 70-85.
(101) Duffy, C. F.; Gafoor, S.; Richards, D. P.; Admadzadeh, H.; O'Kennedy, R.; Arriaga, E. A. Determination of properties of individual liposomes by capillary electrophoresis with postcolumn laser-induced fluorescence detection. *Anal Chem* **2001**, *73*, 1855-1861.
(102) Gelfi, C.; Curcio, M.; Righetti, P. G.; Sebastiano, R.; Citterio, A.; Ahmadzadeh, H.; Dovichi, N. J. Surface modification based on Si-O and Si-C sublayers and a series of N-substituted acrylamide top-layers for capillary electrophoresis. *Electrophoresis* **1998**, *19*, 1677-1682.
(103) Righetti, P. G.; Gelfi, C.; Verzola, B.; Castelletti, L. The state of the art of dynamic coatings. *Electrophoresis* **2001**, *22*, 603-611.
(104) Whiting, C. E.; Arriaga, E. A. CE-LIF analysis of mitochondria using uncoated and dynamically coated capillaries. *Electrophoresis* **2006**, *27*, 4523-4531.
(105) Shen, Y. F.; Smith, R. D. High-resolution capillary isoelectric focusing of proteins using highly hydrophilic-substituted cellulose-coated capillaries. *J Microcolumn Sep* **2000**, *12*, 135-141.

(106) Righetti, P. G.; Simo, C.; Sebastiano, R.; Citterio, A. Carrier ampholytes for IEF, on their fortieth anniversary (1967-2007), brought to trial in court: The verdict. *Electrophoresis* **2007**, *28*, 3799-3810.
(107) Mazzeo, J. R.; Krull, I. S. Capillary Isoelectric-Focusing of Proteins in Uncoated Fused-Silica Capillaries Using Polymeric Additives. *Anal Chem* **1991**, *63*, 2852-2857.
(108) Thormann, W.; Mosher, R. A. High-resolution computer simulation of electrophoretic mobilization in isoelectric focusing. *Electrophoresis* **2008**, *29*, 1676-1686.
(109) Beckers, J. L.; Everaerts, F. M.; Ackermans, M. T. Determination of absolute mobilities, pK values and separation numbers by capillary zone electrophoresis - effective mobility as a parameter for screening. *J Chromatogr* **1991**, *537*, 407-428.
(110) Shen, Y. F.; Xiang, F.; Veenstra, T. D.; Fung, E. N.; Smith, R. D. High-resolution capillary isoelectric focusing of complex protein mixtures from lysates of microorganisms. *Anal Chem* **1999**, *71*, 5348-5353.
(111) Shimura, K.; Zhi, W.; Matsumoto, H.; Kasai, K. Accuracy in the determination of isoelectric points of some proteins and a peptide by capillary isoelectric focusing: Utility of synthetic peptides as isoelectric point markers. *Anal Chem* **2000**, *72*, 4747-4757.
(112) Righetti, P. G. Determination of the isoelectric point of proteins by capillary isoelectric focusing. *J Chromatogr A* **2004**, *1037*, 491-499.
(113) Banks, P. R. Fluorescent derivatization for low concentration protein analysis by capillary electrophoresis. *Trac-Trend Anal Chem* **1998**, *17*, 612-622.
(114) Ramsay, L. M.; Dickerson, J. A.; Dada, O.; Dovichi, N. J. Femtomolar Concentration Detection Limit and Zeptomole Mass Detection Limit for Protein Separation by Capillary Isoelectric Focusing and Laser-Induced Fluorescence Detection. *Anal Chem* **2009**, *81*, 1741-1746.
(115) Slais, K.; Horka, M.; Novackova, J.; Friedl, Z. Fluorescein-based pl markers for capillary isoelectric focusing with laser-induced fluorescence detection. *Electrophoresis* **2002**, *23*, 1682-1688.
(116) Pyell, U. Characterization of nanoparticles by capillary electromigration separation techniques. *Electrophoresis* **2010**, *31*, 814-831.
(117) Michen, B.; Graule, T. Isoelectric points of viruses. *Journal of Applied Microbiology* **2010**, *109*, 388-397.
(118) Bjellqvist, B.; Hughes, G. J.; Pasquali, C.; Paquet, N.; Ravier, F.; Sanchez, J. C.; Frutiger, S.; Hochstrasser, D. The focusing positions of polypeptides in immobilized pH gradients can be predicted from their amino acid sequences. *Electrophoresis* **1993**, *14*, 1023-1031.
(119) Bjellqvist, B.; Basse, B.; Olsen, E.; Celis, J. E. Reference points for comparisons of 2-dimensional maps of proteins from different human cell types defined in a pH scale where isoelectric points correlate with polypeptide compositions. *Electrophoresis* **1994**, *15*, 529-539.

(120) Rezwan, K.; Meier, L. P.; Gauckler, L. J. A prediction method for the isoelectric point of binary protein mixtures of bovine serum albumin and lysozyme adsorbed on colloidal titania and alumina particles. *Langmuir* **2005**, *21*, 3493-3497.
(121) Hovius, R.; Lambrechts, H.; Nicolay, K.; Dekruijff, B. Improved methods to isolate and subfractionate rat-liver mitochondria. Lipid composition of the inner and outer membrane. *Biochim Biophys Acta* **1990**, *1021*, 217-226.
(122) Hovius, R.; Thijssen, J.; Vanderlinden, P.; Nicolay, K.; Dekruijff, B. Phospholipid asymmetry of the outer membrane of rat liver mitochondria: Evidence for the presence of cardiolipin on the outside of the outer membrane. *Febs Lett* **1993**, *330*, 71-76.
(123) deKroon, A.; Dolis, D.; Mayer, A.; Lill, R.; deKruijff, B. Phospholipid composition of highly purified mitochondrial outer membranes of rat liver and Neurospora crassa. Is cardiolipin present in the mitochondrial outer membrane? *Biochimica Et Biophysica Acta-Biomembranes* **1997**, *1325*, 108-116.
(124) Liu, J. H.; Dai, Q.; Chen, J.; Durrant, D.; Freeman, A.; Liu, T.; Grossman, D.; Lee, R. M. Phospholipid scramblase 3 controls mitochondrial structure, function, and apoptotic response. *Molecular Cancer Research* **2003**, *1*, 892-902.
(125) Gebert, N.; Joshi, A. S.; Kutik, S.; Becker, T.; McKenzie, M.; Guan, X. L.; Mooga, V. P.; Stroud, D. A.; Kulkarni, G.; Wenk, M. R.; Rehling, P.; Meisinger, C.; Ryan, M. T.; Wiedemann, N.; Greenberg, M. L.; Pfanner, N. Mitochondrial cardiolipin involved in outer-membrane protein biogenesis: implications for Barth syndrome. *Current Biology* **2009**, *19*, 2133-2139.
(126) The-Uniprot-Consortium. Reorganizing the protein space at the Universal Protein Resource (UniProt). *Nucleic Acids Research* **2012**, *40*, D71-D75.
(127) Smith, A. C.; Robinson, A. J. Mitominer, an integrated database for the storage and analysis of mitochondrial proteomics data. *Mol Cell Proteomics* **2009**, *8*, 1324-1337.
(128) Narendra, D. P.; Youle, R. J. Targeting mitochondrial dysfunction: role for PINK1 and Parkin in mitochondrial quality control. *Antioxid. Redox Signal.* **2011**, *14*, 1929-1938.
(129) Amici, A.; Levine, R. L.; Tsai, L.; Stadtman, E. R. Conversion of amino acid residues in proteins and amino acid homopolymers to carbonyl derivatives by metal-catalyzed oxidation reactions. *J Biol Chem* **1989**, *264*, 3341-3346.
(130) Plummer, D. T. Electrophoretic behaviour of mitochondria from kidney and liver rats. *Biochemical Journal* **1965**, *96*, 729-732.
(131) Katyare, S. S.; Fatterpaker, P.; Sreenivasan, A. Heterogeneity of rat liver mitochondrial fractions and the effect of tri-iodothyronine on their protein turnover. *Biochem. J.* **1970**, *118*, 111-121.
(132) Ericson, I. Determination of isoelectric point of rat-liver mitochondria by cross-partition. *Biochimica Et Biophysica Acta* **1974**, *356*, 100-107.
(133) Lundberg, P.; Ericson, I. Mitochondrial inner membrane changes determined by cross partition. *Biochemical and Biophysical Research Communications* **1975**, *65*, 530-536.

(134) Sanchezprieto, J.; Lopezperez, M. J. Influence of the conformational state on the isoelectric points of rat brain synaptosomes, mitochondria and mitoplasts. *Biochimica Et Biophysica Acta* **1984**, *778*, 81-86.
(135) Wallace, D. C. Mitochondrial diseases in man and mouse. *Science* **1999**, *283*, 1482-1488.
(136) Chen, H. C.; Detmer, S. A.; Ewald, A. J.; Griffin, E. E.; Fraser, S. E.; Chan, D. C. Mitofusins Mfn1 and Mfn2 coordinately regulate mitochondrial fusion and are essential for embryonic development. *J. Cell Biol.* **2003**, *160*, 189-200.
(137) Kohlheyer, D.; Eijkel, J. C. T.; Schlautmann, S.; van den Berg, A.; Schasfoort, R. B. M. Microfluidic high-resolution free-flow isoelectric focusing. *Anal Chem* **2007**, *79*, 8190-8198.
(138) Horka, M.; Ruzicka, F.; Horky, J.; Hola, V.; Slais, K. Capillary isoelectric focusing and fluorometric detection of proteins and microorganisms dynamically modified by poly(ethylene glycol) pyrenebutanoate. *Anal Chem* **2006**, *78*, 8438-8444.
(139) Horka, M.; Kubicek, O.; Kubesovi, A.; Kubickova, Z.; Rosenbergova, K.; Slais, K. Testing of the influenza virus purification by CIEF. *Electrophoresis* **2010**, *31*, 331-338.
(140) Forner, F.; Arriaga, E. A.; Mann, M. Mild protease treatment as a small-scale biochemical method for mitochondria purification and proteomic mapping of cytoplasm-exposed mitochondrial proteins. *J Proteome Res* **2006**, *5*, 3277-3287.
(141) Poe, B. G.; Duffy, C. F.; Greminger, M. A.; Nelson, B. J.; Arriaga, E. A. Detection of heteroplasmy in individual mitochondrial particles. *Anal. Bioanal. Chem.* **2010**, *397*, 3397-3407.
(142) Davis, J. M.; Arriaga, E. A. Evaluation of peak overlap in migration-time distributions determined by organelle capillary electrophoresis: Type-II error analogy based on statistical-overlap theory. *J Chromatogr A* **2009**, *1216*, 6335-6342.
(143) Righetti, P. G.; Righetti, A. B.; Galante, E. Some Optical-Properties of Carrier Ampholytes for Isoelectric Focusing. *Anal Biochem* **1975**, *63*, 423-432.
(144) Righetti, P. G.; Citterio, A.; Girault, H. Gel-free IEF in a membrane-sealed multicompartment cell for proteome prefractionation. *Electrophoresis* **2007**, *28*, 1860-1866.
(145) Whiting, C. E.; Arriaga, E. A. Evaluation of individual particle capillary electrophoresis experiments via quantile analysis. *J Chromatogr A* **2007**, *1157*, 446-453.
(146) Benard, G.; Rossignol, R. Ultrastructure of the mitochondrion and its bearing on function and bioenergetics. *Antioxid. Redox Signal.* **2008**, *10*, 1313-1342.
(147) Olsen, J. V.; Ong, S. E.; Mann, M. Trypsin cleaves exclusively C-terminal to arginine and lysine residues. *Mol. Cell. Proteomics* **2004**, *3*, 608-614.
(148) Gao, L.; Liu, S. R. Cross-linked polyacrylarnide coating for capillary isoelectric focusing. *Anal Chem* **2004**, *76*, 7179-7186.
(149) Dada, O. O.; Ramsay, L. M.; Dickerson, J. A.; Cermak, N.; Jiang, R.; Zhu, C. R.; Dovichi, N. J. Capillary array isoelectric focusing with laser-induced fluorescence detection: milli-pH unit resolution and yoctomole mass detection limits in a 32-channel system. *Anal. Bioanal. Chem.* **2010**, *397*, 3305-3310.

(150) Wen, J.; Wilker, E. W.; Yaffe, M. B.; Jensen, K. F. Microfluidic Preparative Free-Flow Isoelectric Focusing: System Optimization for Protein Complex Separation. *Anal Chem* **2010**, *82*, 1253-1260.
(151) Dukhin, A. S. Biospecific Mechanism of Double-Layer Formation and Peculiarities of Cell Electrophoresis. *Colloid Surface A* **1993**, *73*, 29-48.
(152) Dukhin, A. S.; Ulberg, Z. R.; Karamushka, V. I.; Gruzina, T. G. Peculiarities of live cells' interaction with micro- and nanoparticles. *Advances in Colloid and Interface Science* **2010**, *159*, 60-71.
(153) Shimura, K. Recent advances in IEF in capillary tubes and microchips. *Electrophoresis* **2009**, *30*, 11-28.
(154) Wolken, G. G.; Kostal, V.; Arriaga, E. A. Capillary Isoelectric Focusing of Individual Mitochondria. *Anal Chem* **2011**, *83*, 612-618.
(155) Moncelli, M. R.; Becucci, L.; Guidelli, R. The intrinsic pK_a values for phosphatidylcholine, phosphatidylethanolamine, and phosphatidylserine in monolayers deposited on mercury electrodes. *Biophysical Journal* **1994**, *66*, 1969-1980.
(156) Tsui, F. C.; Ojcius, D. M.; Hubbell, W. L. The intrinsic pK_a values for phosphatidylserine and phosphatidylethanolamine in phosphatidylcholine host bilayers. *Biophysical Journal* **1986**, *49*, 459-468.
(157) Kates, M.; Syz, J. Y.; Gosser, D.; Haines, T. H. pH-dissociation characteristics of cardiolipin and its 2'-deoxy analogue. *Lipids* **1993**, *28*, 877-882.
(158) Terrell, G. R.; Scott, D. W. Oversmoothed Nonparametric Density Estimates. *J. Am. Stat. Assoc.* **1985**, *80*, 209-214.
(159) Nystrom, T. Role of oxidative carbonylation in protein quality control and senescence. *Embo J.* **2005**, *24*, 1311-1317.
(160) Stojanovski, D.; Koutsopoulos, O. S.; Okamoto, K.; Ryan, M. T. Levels of human Fis1 at the mitochondrial outer membrane regulate mitochondrial morphology. *J Cell Sci* **2004**, *117*, 1201-1210.
(161) Osman, C.; Voelker, D. R.; Langer, T. Making heads or tails of phospholipids in mitochondria. *J Cell Biol* **2011**, *192*, 7-16.
(162) Korytowski, W.; Basova, L. V.; Pilat, A.; Kernstock, R. M.; Girotti, A. W. Permeabilization of the mitochondrial outer membrane by Bax/truncated Bid (tBid) proteins as sensitized by cardiolipin hydroperoxide translocation. Mechanistic implications for the intrinsic pathway of oxidative apoptosis. *J Biol Chem* **2011**, *286*, 26334-26343.
(163) Horka, M.; Horky, J.; Kubesova, A.; Zapletalova, E.; Slais, K. The trace analysis of microorganisms in real samples by combination of a filtration microcartridge and capillary isoelectric focusing. *Anal. Bioanal. Chem.* **2011**, *400*, 3133-3140.
(164) Kamo, N.; Muratsugu, M.; Kurihara, K.; Kobatake, Y. Change in Surface-Charge Density and Membrane-Potential of Intact Mitochondria during Energization. *Febs Lett* **1976**, *72*, 247-250.

(165) Aiuchi, T.; Kamo, N.; Kurihara, K.; Kobatake, Y. Significance of surface-potential in interaction of 8-anilino-1-naphthalenesulfonate with mitochondria - fluorescence intensity and zeta potential. *Biochemistry* **1977**, *16*, 1626-1630.
(166) Tsoneva, I. C.; Tomov, T. C. Relationship between the Power of Energization and the Electrophoretic Mobility of Rat-Liver Mitochondria. *Bioelectroch Bioener* **1984**, *12*, 253-258.
(167) Phayre, A. N.; Farfano, H. M. V.; Hayes, M. A. Effects of pH gradients on liposomal charge states examined by capillary electrophoresis. *Langmuir* **2002**, *18*, 6499-6503.
(168) Nauratil, M.; Terman, A.; Arriaga, E. A. Giant mitochondria do not fuse and exchange their contents with normal mitochondria. *Exp Cell Res* **2008**, *314*, 164-172.
(169) Reers, M.; Smith, T. W.; Chen, L. B. J-Aggregate Formation of a Carbocyanine as a Quantitative Fluorescent Indicator of Membrane-Potential. *Biochemistry-Us* **1991**, *30*, 4480-4486.
(170) Moe, M. K.; Samuelsen, P. J.; Nielsen, H. V.; Nielsen, K. M. Separation of DNA-containing organelles from Toxoplasma gondii by CZE. *Electrophoresis* **2010**, *31*, 1344-1349.
(171) Zhao, W. F.; Waisum, O.; Fung, Y. S.; Cheung, M. P. Analysis of mitochondria by capillary electrophoresis: Cardiolipin levels decrease in response to carbonyl cyanide 4-(trifluoromethoxy) phenylhydrazone. *Eur. J. Lipid Sci. Technol.* **2010**, *112*, 1058-1066.
(172) Aiuchi, T.; Kamo, N.; Kurihara, K.; Kobatake, Y. Significance of Surface-Potential in Interaction of 8-Anilino-1-Naphthalenesulfonate with Mitochondria - Fluorescence Intensity and Zeta Potential. *Biochemistry-Us* **1977**, *16*, 1626-1630.
(173) Pressman, B. C. Biological applications of ionophores. *Annu. Rev. Biochem.* **1976**, *45*, 501-530.
(174) Herman, T. K.; Mackowiak, S. A.; Kaufman, L. J. High power light emitting diode based setup for photobleaching fluorescent impurities. *Rev Sci Instrum* **2009**, *80*.
(175) Davis, J. M.; Arriaga, E. A. Estimation of Migration-Time and Mobility Distributions in Organelle Capillary Electrophoresis with Statistical-Overlap Theory. *Anal Chem* **2010**, *82*, 307-315.
(176) Andreyev, D.; Arriaga, E. A. Simultaneous laser-induced fluorescence and scattering detection of individual particles separated by capillary electrophoresis. *Anal Chem* **2007**, *79*, 5474-5478.
(177) Salvioli, S.; Ardizzoni, A.; Franceschi, C.; Cossarizza, A. JC-1, but not DiOC(6)(3) or rhodamine 123, is a reliable fluorescent probe to assess Delta Psi changes in intact cells: Implications for studies on mitochondrial functionality during apoptosis. *Febs Lett* **1997**, *411*, 77-82.
(178) Rolfe, D. F. S.; Hulbert, A. J.; Brand, M. D. Characteristics of Mitochondrial Proton Leak and Control of Oxidative-Phosphorylation in the Major Oxygen-Consuming Tissues of the Rat. *Bba-Bioenergetics* **1994**, *1188*, 405-416.
(179) Ramsay, L. M.; Dickerson, J. A.; Dovichi, N. J. Attomole protein analysis by CIEF with LIF detection. *Electrophoresis* **2009**, *30*, 297-302.

(180) Poitevin, M.; Peltre, G.; Descroix, S. Use of quasi-isoelectric buffers as anolyte and catholyte to improve capillary isoelectric focusing performances. *Electrophoresis* **2008**, *29*, 1687-1693.
(181) Mack, S.; Cruzado-Park, I.; Chapman, J.; Ratnayake, C.; Vigh, G. A systematic study in CIEF: Defining and optimizing experimental parameters critical to method reproducibility and robustness. *Electrophoresis* **2009**, *30*, 4049-4058.
(182) Maiuri, M. C.; Zalckvar, E.; Kimchi, A.; Kroemer, G. Self-eating and self-killing: crosstalk between autophagy and apoptosis. *Nat Rev Mol Cell Biol* **2007**, *8*, 741-752.
(183) Ahmadzadeh, H.; Andreyev, D.; Arriaga, E. A.; Thompson, L. V. Capillary Electrophoresis Reveals Changes in Individual Mitochondrial Particles Associated With Skeletal Muscle Fiber Type and Age. *The Journals of Gerontology Series A: Biological Sciences and Medical Sciences* **2006**, *61*, 1211-1218.
(184) Koves, T. R.; Noland, R. C.; Bates, A. L.; Henes, S. T.; Muoio, D. M.; Cortright, R. N. Subsarcolemmal and intermyofibrillar mitochondria play distinct roles in regulating skeletal muscle fatty acid metabolism. *Am. J. Physiol.-Cell Physiol.* **2005**, *288*, C1074-C1082.
(185) Chomentowski, P.; Coen, P. M.; Radikova, Z.; Goodpaster, B. H.; Toledo, F. G. S. Skeletal Muscle Mitochondria in Insulin Resistance: Differences in Intermyofibrillar Versus Subsarcolemmal Subpopulations and Relationship to Metabolic Flexibility. *J. Clin. Endocrinol. Metab.* **2011**, *96*, 494-503.
(186) Feng, J.; Navratil, M.; Thompson, L. V.; Arriaga, E. A. Estimating relative carbonyl levels in muscle microstructures by fluorescence imaging. *Anal Bioanal Chem* **2008**, *391*, 2591-2598.
(187) Chabi, B.; Ljubicic, V.; Menzies, K. J.; Huang, J. H.; Saleem, A.; Hood, D. A. Mitochondrial function and apoptotic susceptibility in aging skeletal muscle. *Aging Cell* **2008**, *7*, 2-12.
(188) Picard, M.; Taivassalo, T.; Gouspillou, G.; Hepple, R. T. Mitochondria: isolation, structure and function. *J. Physiol.-London* **2011**, *589*, 4413-4421.
(189) Ravelli, R. B. G.; Gigant, B.; Curmi, P. A.; Jourdain, I.; Lachkar, S.; Sobel, A.; Knossow, M. Insight into tubulin regulation from a complex with colchicine and a stathmin-like domain. *Nature* **2004**, *428*, 198-202.
(190) Miller, R. G. Interactions between digitonin and bilayer-membranes. *Biochimica Et Biophysica Acta* **1984**, *774*, 151-157.
(191) Weaver, J. C.; Smith, K. C.; Esser, A. T.; Son, R. S.; Gowrishankar, T. R. A brief overview of electroporation pulse strength-duration space: A region where additional intracellular effects are expected. *Bioelectrochemistry* **2012**, *87*, 236-243.
(192) Islinger, M.; Eckerskorn, C.; Volkl, A. Free-flow electrophoresis in the proteomic era: A technique in flux. *Electrophoresis* **2010**, *31*, 1754-1763.
(193) Wen, J. A.; Albrecht, J. W.; Jensen, K. F. Microfluidic preparative free-flow isoelectric focusing in a triangular channel: System development and characterization. *Electrophoresis* **2010**, *31*, 1606-1614.

(194) Zhu, G. J.; Sun, L. L.; Yang, P.; Dovichi, N. J. On-line amino acid-based capillary isoelectric focusing-ESI-MS/MS for protein digests analysis. *Anal Chim Acta* **2012**, *750*, 207-211.
(195) Ong, S. E.; Blagoev, B.; Kratchmarova, I.; Kristensen, D. B.; Steen, H.; Pandey, A.; Mann, M. Stable isotope labeling by amino acids in cell culture, SILAC, as a simple and accurate approach to expression proteomics. *Mol Cell Proteomics* **2002**, *1*, 376-386.
(196) Ross, P. L.; Huang, Y. L. N.; Marchese, J. N.; Williamson, B.; Parker, K.; Hattan, S.; Khainovski, N.; Pillai, S.; Dey, S.; Daniels, S.; Purkayastha, S.; Juhasz, P.; Martin, S.; Bartlet-Jones, M.; He, F.; Jacobson, A.; Pappin, D. J. Multiplexed protein quantitation in Saccharomyces cerevisiae using amine-reactive isobaric tagging reagents. *Mol Cell Proteomics* **2004**, *3*, 1154-1169.
(197) Geiger, T.; Cox, J.; Ostasiewicz, P.; Wisniewski, J. R.; Mann, M. Super-SILAC mix for quantitative proteomics of human tumor tissue. *Nat. Methods* **2010**, *7*, 383-U64.
(198) Wu, C. C.; MacCoss, M. J.; Howell, K. E.; Matthews, D. E.; Yates, J. R. Metabolic labeling of mammalian organisms with stable isotopes for quantitative proteomic analysis. *Anal Chem* **2004**, *76*, 4951-4959.
(199) Shevchenko, A.; Tomas, H.; Havlis, J.; Olsen, J. V.; Mann, M. In-gel digestion for mass spectrometric characterization of proteins and proteomes. *Nat Protoc* **2006**, *1*, 2856-2860.

Appendix A

Supporting Information for Chapter 3

A.1. Control for False Positives

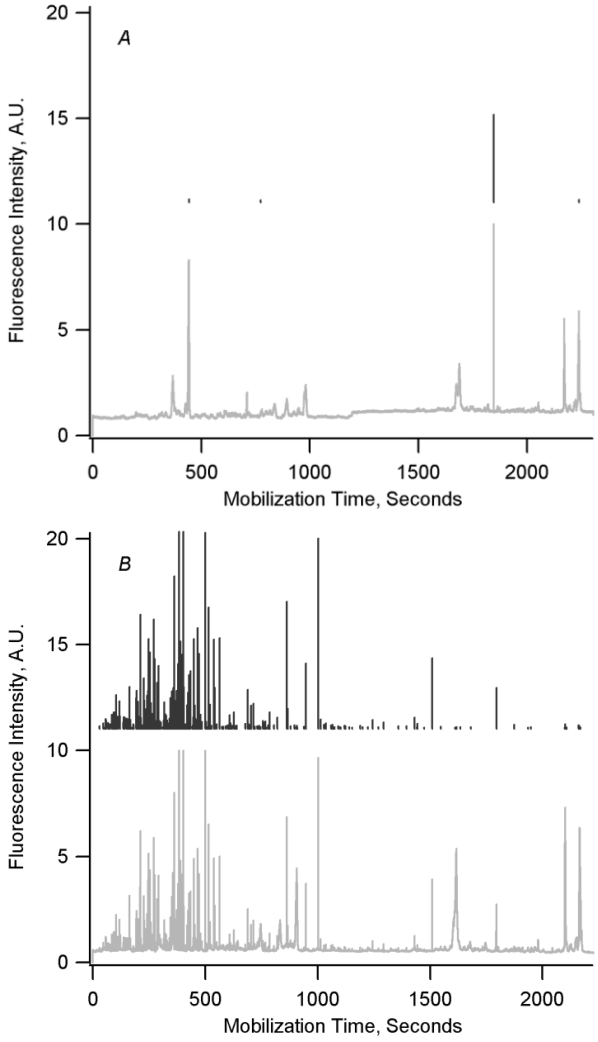

Figure A-1. Control for false positives. *A)* shows a cIEF trace of unlabeled mitochondria, which mainly shows broad peaks corresponding to p*I* standards. *B)* shows a replicate run of the same sample in which mitochondria were labeled with NAO. There are 7 spikes selected as events in *A* and 509 spikes selected as events in *B* (top traces, y-axis offset) when a threshold of 5 standard deviations over the background signal is used. Separation conditions for both runs: 1% Biolyte 3-10, 1% Biolyte 4-6, 230 mM sucrose, 0.02 ng/mL of each fluorescent p*I* marker. The anolyte, catholyte, and chemical mobilizer were 100 mM H_3PO_4, 20 mM NaOH, and 350 mM acetic acid. The electric field applied during focusing and mobilization was 400 V/cm. Detection was at 535 ± 17.5 nm, data acquisition was at 100 Hz, 1000 V was applied to the PMT.

A.2. Peak Overlap

To determine that peak overlap is not a significant problem, we have adapted a statistical test designed for mitochondrial capillary electrophoresis.[1] In the experiment shown in Figure 3-2, the 360 events can be represented in a histogram with 10 bins, as shown in Figure 3-3 (A2). Now, the most crowded bin (from pI = 6.00 to 6.33, or t_m = 379.41 to 229.96 seconds) contains 99 events, and by measuring the baseline peak widths we calculate an average peak standard deviation σ = 0.016 ± 0.006 seconds. The reduced peak standard deviation s can be calculated by $s = \log(\sigma/X)$ where X is the width in seconds of a bin. Using the equation $\bar{m} = -751.38 - 1429.1s - 1061.4s^2 - 391.14s^3 - 71.756s^4 - 5.4210s^5$ for β_t = 0.90, we can calculate a critical peak saturation threshold $\bar{m}$ of 189 peaks. Since the number of observed peaks in this bin (99) is much smaller than the critical peak saturation threshold, we can say that the observed peak number is a good representation of the number of actual peaks in this experiment, and peak overlap is not a significant issue. Repeating this analysis for the experiment shown in Figure 3-3 *(*A1) also results in a critical peak saturation threshold of $\bar{m} = 189$, which is above the number of observed peaks in the most crowded bin (116 peaks from pI = 6.00 to 6.33 or t_m = 409.32 to 260.16 seconds).

A.3. Photobleaching of Carrier Ampholytes

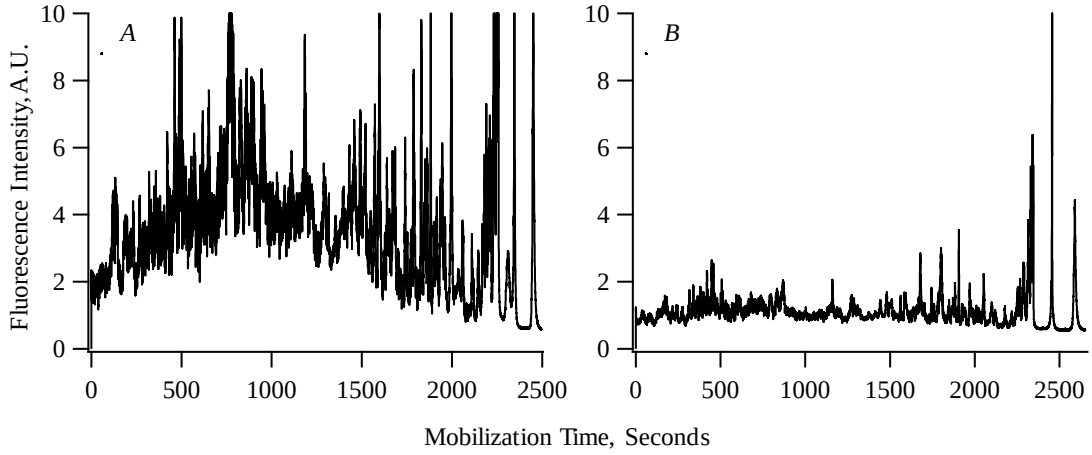

Figure A-2. Effect of photobleaching carrier ampholytes. (A) is not photobleached, (B) is photobleached overnight with an LED. A solution of 2% Biolyte 3-10 and 2% Biolyte 4-6 with 220 mM sucrose was injected by pressure and focused at 600 V/cm for 20 minutes in an HPC-coated capillary of total length 41.5 cm and effective length 38.2 cm. Mobilization was at 600 V/cm with 20 mM acetic acid, detection at 535 ± 17.5 nm, data acquisition at 10 Hz, 1000 V applied to PMT. The average signal is 3.57 ± 1.84 V for (A) and 1.11 ± 0.45 V for (B).

A.4. Propagation of Error in p*I* Determination

It is informative to calculate the uncertainty introduced by using a linear interpolation between two p*I* markers to determine the p*I* of an individual mitochondrion. Standard formulas for calculation of uncertainty in linear regression do not apply because the p*I* is calculated using only two data points. Accordingly, we must first derive an expression for calculating the p*I* of an individual mitochondrion (pI_x) using the mobilization times ($t_{m,std1}$ and $t_{m,std2}$) and pIs (pI_{std1} and pI_{std2}) of the standards and the mobilization time ($t_{m,x}$) of the mitochondrion. An expression for pI_x is found by writing an equality for the Pythagorean distances between the pairs of points $(t_{m,std1}, pI_{std1}), (t_{m,std2}, pI_{std2})$, $(t_{m,std1}, pI_{std1}), (t_{m,x}, pI_x)$, and $(t_{m,x}, pI_x), (t_{m,std2}, pI_{std2})$, then solving for pI_x. This is shown below graphically.

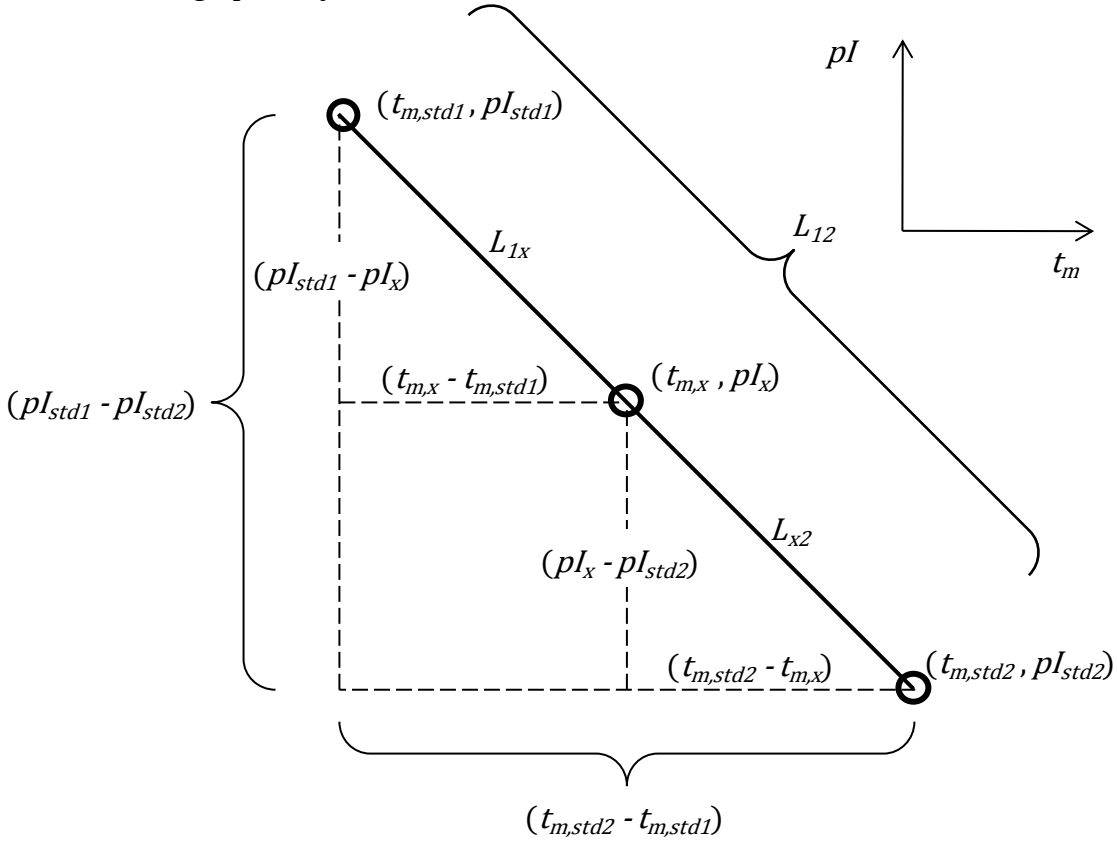

Figure A-3. Graphical representation of p*I* determination.

In Figure A-3, the distances between the pairs of points are:

$$L_{12} = \sqrt{(pI_{std1} - pI_{std2})^2 + \left(t_{m,std2} - t_{m,std1}\right)^2} \qquad \text{(Equation A-1)}$$

$$L_{1x} = \sqrt{(pI_{std1} - pI_x)^2 + \left(t_{m,x} - t_{m,std1}\right)^2} \qquad \text{(Equation A-2)}$$

$$L_{x2} = \sqrt{(pI_x - pI_{std2})^2 + \left(t_{m,std2} - t_{m,x}\right)^2} \qquad \text{(Equation A-3)}$$

Setting $L_{12} = L_{1x} + L_{x2}$ and solving the expression for pI_x, we get:

$$pI_x = \frac{pI_{std2} \times t_{m,std1} - pI_{std1} \times t_{m,std2} + pI_{std1} \times t_{m,x} - pI_{std2} \times t_{m,x}}{t_{m,std1} - t_{m,std2}} = F \qquad \text{(Equation A-4)}$$

To find the uncertainty in pI_x calculated by *F*, we must evaluate the following expression:[2]

$$e_{pI_x} = \sqrt{\left(\frac{\partial F}{\partial pI_{std1}}\right)^2 e_{pI_{std1}}^2 + \left(\frac{\partial F}{\partial pI_{std2}}\right)^2 e_{pI_{std2}}^2 + \left(\frac{\partial F}{\partial t_{m,std1}}\right)^2 e_{t_{m,std1}}^2 + \left(\frac{\partial F}{\partial t_{m,std2}}\right)^2 e_{t_{m,std2}}^2 + \left(\frac{\partial F}{\partial t_{m,x}}\right)^2 e_{t_{m,x}}^2}$$

(Equation A-5)

The *e* terms in equation A-5 are the uncertainties in the p*I*s and mobilization times. Evaluating and simplifying this expression (using Mathematica 7.01.0 software, Wolfram Research Inc.), we can write the following expression:

$$e_{pI_x} = \sqrt{\frac{1}{(t_{m,std1} - t_{m,std2})^4} \begin{pmatrix} e_{pI_{std1}}^2 (t_{m,std1} - t_{m,std2})^2 (t_{m,std2} - t_{m,x})^2 + \\ e_{pI_{std2}}^2 (t_{m,std1} - t_{m,std2})^2 (t_{m,std1} - t_{m,x})^2 + \\ e_{t_{m,std1}}^2 (pI_{std1} - pI_{std2})^2 (t_{m,std2} - t_{m,x})^2 + \\ e_{t_{m,std2}}^2 (pI_{std1} - pI_{std2})^2 (t_{m,std1} - t_{m,x})^2 + \\ e_{t_{m,x}}^2 (pI_{std1} - pI_{std2})^2 (t_{m,std1} - t_{m,std2})^2 \end{pmatrix}}$$

(Equation A-6)

The uncertainties in the measurement of mobilization times (the e_{t_m} terms) are 0.01 seconds because the data is collected at 100 Hz. The uncertainties in the p*I* of each standard (the $e_{pI_{std}}$terms) are assumed to be 0.1 pH units. For the mitochondrial cIEF

experiment shown in Figure 3-1, the mobilization times of the p*I* 6.5 and 5.5 standards are, respectively, 148.04 seconds and 611.67 seconds. Shown below is a plot of p*I* vs. t_m for these two standards, with the dashed lines representing the p*I* plus or minus the calculated uncertainties from equation A-6 above. Uncertainties range from a maximum of 0.14 at $t_m = 0$ to a minimum of 0.07 at $t_m = 379.86$, directly between the p*I* markers.

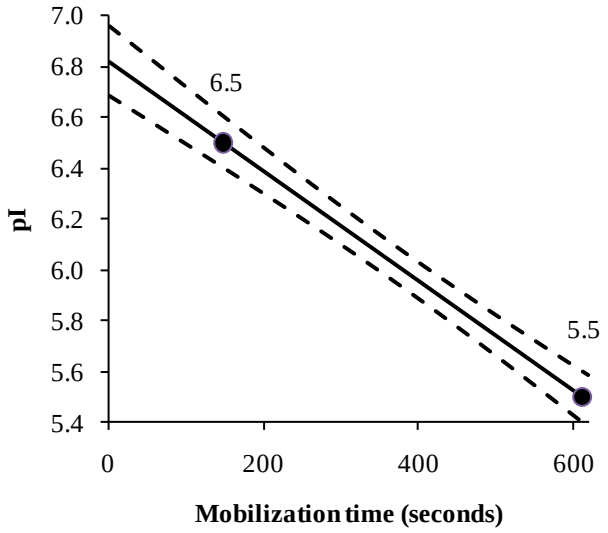

Figure A-4. Uncertainty in p*I* calculation.

References for Appendix A

1. Davis, J. M.; Arriaga, E. A., Evaluation of peak overlap in migration-time distributions determined by organelle capillary electrophoresis: Type-II error analogy based on statistical-overlap theory. *J Chromatogr A* **2009,** *1216* (35), 6335-6342.
2. Harris, D. C., *Quantitative chemical analysis*. W.H. Freeman and Co.: New York, 2003.

Appendix B

Supporting Information for Chapter 4

B.1. Initial Conditions

Amino acid component of model. The complete proteome of the outer mitochondrial membrane is unknown, so we determined initial conditions for the amino acid component of the model by defining an "average protein" to avoid biasing the results of the model toward those mitochondrial membrane proteins which have already been discovered by current techniques. First, the average sequence length in the UniProt Knowledgebase protein database was 351 amino acids (accessed Dec. 18, 2009).[1] Data on the relative abundance of amino acids in proteins is also available from this database (Table B-1). We calculated abundance by mass for each of the twenty common amino acids (molecular weight multiplied by relative abundance). We then calculated an abundance-weighted average molecular weight for an amino acid of 129.0 Da. Therefore, the "average protein" of 351 amino acids has a molecular weight of 45283 Da. From this value, we calculate 0.04528 mg protein/nmol protein for the "average protein". We next considered only the ionizable amino acids to find the relative abundance of ionizable amino acids in an "average protein" (Table B-2). We assume a model of a transmembrane protein with a hydrophobic transmembrane domain and hydrophilic domains exposed on the inside and outside of the membrane. Assuming ionizable amino acids are located only in these hydrophilic domains, and that the inner and outer domains are of equal size, we calculate that each "average protein" (with 351 total amino acid residues) has 53 ionizable amino acids on the outer surface of the membrane (since the relative abundance of ionizable amino acids on the outer surface of the membrane to all amino acids is 15%, Table B-2).

Although the complete proteome of the outer mitochondrial membrane is unknown, a comparison of the average ionizable amino acid composition of known mitochondrial outer membrane proteins (from Table B-4) to the normalized ionizable amino acid composition of the "average protein" reveals a difference of 1.1% or less for each amino acid with a total absolute difference of less than 4%. This comparison is shown in Table B-2 (below). This result suggests that the "average protein" is a reasonable model for mitochondrial outer membrane proteins.

Phospholipid component of model. We have included five phospholipids that contribute to mitochondrial p*I* (see Table 4-1 in Chapter 4). Both Hovius et al. and de Kroon et al. determined the relative phospholipid composition and phospholipid to protein ratio in outer mitochondrial membranes of mitochondria isolated from rat liver.[2-3] We use an average value of their determinations. We excluded phospholipids determined by de Kroon et al. to be less than 1% each of the outer mitochondrial membrane (phosphatidic acid, phosphatidylglycerol, lyso-phospholipids, and sphingomyelin, representing a total of 1.7% of their determination). We also consider the determination by Hovius et al. of accessible (outer leaflet) outer membrane phospholipids in rat liver mitochondria by multiplying the average abundance of outer membrane phospholipids by the fraction that is present on the cytosolic side of the outer mitochondrial membrane (see Table B-3).[4] Cardiolipin (CL) was previously thought to be exclusively found in the inner mitochondrial membrane, but we include it in our model as an outer mitochondrial membrane phospholipid. While de Kroon et al. did not detect significant levels of CL in

the outer membrane, other reports have determined that from 9 to 25% of the outer mitochondrial membrane phospholipids are CL.[5-6] Therefore, it seems prudent to consider CL as an outer membrane phospholipid in the model (see Table 4-1 in Chapter 4).

Phospholipid to protein ratio. de Kroon et al. (1997) and Hovius et al. (1990) determined phospholipid to protein ratios in the outer mitochondrial membrane of 1220 and 1110 nmol phosphorus per mg protein, respectively. We use an average value of these two determinations and the ratio determined above for an "average protein" of 0.04528 mg protein per nmol protein to calculate a ratio of 52.76 mol phospholipid per mol protein in our model. Combining this ratio and our assumption of 53 ionizable amino acids on the outer surface of the membrane per "average protein," we calculate a ratio of 1.0 mol phospholipid per mol ionizable amino acid for the outer membrane surface. We use this ratio and the values for initial conditions of amino acids and phospholipids to determine initial conditions in numbers of amino acids and phospholipids for the model (Table 1 in Chapter 4).

Table B-1. Average amino acid composition of all known proteins.[a]

Amino acid	Average composition (%)	Molecular weight (Da)	Composition normalized by molecular weight[b] (%)
ala	8.28	89.1	5.72
arg	5.54	174.2	7.48
asn	4.05	132.1	4.15
asp	5.45	133.1	5.62
cys	1.35	121.2	1.27
gln	3.94	146.2	4.46
glu	6.77	147.1	7.72
gly	7.09	75.1	4.12
his	2.27	155.2	2.73
ile	5.99	131.2	6.09
leu	9.67	131.2	9.84
lys	5.86	146.2	6.64
met	2.42	149.2	2.80
phe	3.86	165.2	4.95
pro	4.68	115.1	4.18
ser	6.50	105.1	5.29
thr	5.32	119.1	4.91
trp	1.07	204.2	1.69
tyr	2.91	181.2	4.08
val	6.88	117.2	6.25
Total	**100%**	N/A	**100%**

a. Calculated from all entries in the complete Uniprot KB protein database (http://ca.expasy.org/sprot/relnotes/relstat.html, accessed Dec. 18, 2009)
b. Normalized by multiplying the average composition of each amino acid by the molecular weight of that amino acid and dividing by the average molecular weight of all the amino acids

Table B-2. Ionizable amino acids contributing to isoelectric point for initial conditions and comparison to average amino acid composition from known outer mitochondrial membrane proteins.

Amino acid	Average composition (%)	Normalized composition (%)	Normalized composition, OMM proteins[a] (%)	Absolute value of difference (%)
arg	5.54	18.37	18.43	0.06
asp	5.45	18.08	17.40	0.68
cys	1.35	4.48	5.58	1.10
glu	6.77	22.45	23.19	0.74
his	2.27	7.53	7.06	0.47
lys	5.86	19.44	18.85	0.59
tyr	2.91	9.65	9.48	0.17
Total	**30%**	**100%**	**100%**	**3.81%**

a. Average composition of outer mitochondrial membrane (OMM) proteins in Table B-4

Table B-3. Phospholipid composition for initial conditions.

Phospholipid	Composition of OM[a] (%)	Accessible on OM[b] (%)	Composition, adjusted for accessibility (%)
phosphatidylcholine (PC)	52.18	55	47.59
phosphatidylethanolamine (PE)	29.70	77	37.93
cardiolipin (CL)	4.70	100	7.80
phosphatidylinositol (PI)	11.84	30	5.89
phosphatidylserine (PS)	1.58	30	0.78
Total	**100%**	N/A	**100%**

a. Average value from Hovius et al. (1990) and de Kroon et al.

b. "Accessible" means accessible by phospholipase A_2 and indicates the phospholipid is located in the outer leaflet of the outer mitochondrial membrane (OM) as determined by Hovius et al. (1993)

B.2. Equation for Isoelectric Point

We derive the Z_x(pH) terms from Equation 4-1 (in Chapter 4) for each functional group by using the Henderson-Hasselbach equation, which is as follows for acidic functional groups

$$\mathrm{pH} = \mathrm{p}K_{a,x} + \log\frac{A_x^-}{\mathrm{H}A_x} \qquad \text{(Equation B-1)}$$

where A^-_x and $\mathrm{H}A_x$ are the fractions of the ionized and neutral forms of x. Now, these fractions are described by

$$A_x^- + \mathrm{H}A_x = 1 \qquad \text{(Equation B-2)}$$

so by combining Equations S-1 and S-2 and solving for the ionized form, we obtain

$$A_x^- = \frac{10^{(\mathrm{pH}-\mathrm{p}K_{a,x})}}{1 + 10^{(\mathrm{pH}-\mathrm{p}K_{a,x})}} = \alpha_x(\mathrm{pH}) \qquad \text{(Equation B-3)}$$

For basic functional groups, the Henderson-Hasselbach equation is written as

$$\mathrm{pH} = \mathrm{p}K_{a,x} + \log\frac{B_x}{B\mathrm{H}_x^+} \qquad \text{(Equation B-4)}$$

and so by a similar derivation we obtain the following expression for the ionized form.

$$B\mathrm{H}_x^+ = \frac{1}{1 + 10^{(\mathrm{pH}-\mathrm{p}K_{a,x})}} = \alpha_x(\mathrm{pH}) \qquad \text{(Equation B-5)}$$

Equation 4-1 (from Chapter 4) is then used with either Equation B-3 or B-5 for all the functional groups shown in Table 4-1 (in Chapter 4) to find the pI of an individual composition (with different n_x for each amino acid and phospholipid). An additional + 1 term is included in the expression for PC to account for its quaternary ammonium cation. The complete expression (Equation B-6) is shown below.

$$
\begin{aligned}
&Z(pH) \\
&\quad = n_{Asp}\left(-\left(\frac{10^{(pH-4.05)}}{10^{(pH-4.05)}+1}\right)\right) + n_{Glu}\left(-\left(\frac{10^{(pH-4.45)}}{10^{(pH-4.45)}+1}\right)\right) + n_{Cys}\left(-\left(\frac{10^{(pH-9.00)}}{10^{(pH-9.00)}+1}\right)\right) \\
&\quad + n_{Tyr}\left(-\left(\frac{10^{(pH-10.00)}}{10^{(pH-10.00)}+1}\right)\right) + n_{His}\left(\frac{1}{10^{(pH-5.98)}+1}\right) + n_{Lys}\left(\frac{1}{10^{(pH-10.00)}+1}\right) + n_{Arg}\left(\frac{1}{10^{(pH-12.00)}+1}\right) \\
&\quad + n_{PC}\left(-\left(\frac{10^{(pH-0.8)}}{10^{(pH-0.8)}+1}\right)+1\right) + n_{PE}\left(-\left(\frac{10^{(pH-0.5)}}{10^{(pH-0.5)}+1}\right)+\left(\frac{1}{10^{(pH-9.6)}+1}\right)\right) + n_{PI}\left(-\left(\frac{10^{(pH-1.0)}}{10^{(pH-1.0)}+1}\right)\right) \\
&\quad + n_{PS}\left(-\left(\frac{10^{(pH-2.3)}}{10^{(pH-2.3)}+1}\right)-\left(\frac{10^{(pH-3.6)}}{10^{(pH-3.6)}+1}\right)+\left(\frac{1}{10^{(pH-9.8)}+1}\right)\right) + n_{CL}\left(-\left(\frac{10^{(pH-2.8)}}{10^{(pH-2.8)}+1}\right)-\left(\frac{10^{(pH-8.5)}}{10^{(pH-8.5)}+1}\right)\right)
\end{aligned}
$$

(Equation B-6)

B.3. Comparison to Mitochondrial Outer Membrane Proteins

The list of mitochondrial outer membrane proteins was obtained using two protein databases (the Mitominer[7] and Uniprot Knowledgebase[1] databases, accessed 7/22/2011). Appropriate keywords and search parameters were used to select proteins from *Rattus norvegicus* located in the mitochondrial outer membrane.

Table B-4. Mitochondrial outer membrane proteins.

Protein name	p*I*[a]	Accession	IPI
TOM22_RAT	4.2603	Q75Q41	IPI00417749
Q5K547_RAT	4.3491	Q5K547	IPI00231893
Q9QWT2_RAT	4.4969	Q9QWT2	IPI00957420
Q7TS62_RAT	4.7136	Q7TS62	IPI00231894
BAX_RAT	4.8403	Q63690	IPI00211129
Q63144_RAT	4.8637	Q63144	IPI00193233
B2CL1_RAT	4.8659	P53563	IPI00211135
Q9WUI5_RAT	4.9214	Q9WUI5	IPI00231893
AKAP1_RAT	4.9303	O88884	IPI00213479
Q548R7_RAT	5.0048	Q548R7	IPI00231893
CYB5B_RAT	5.0070	P04166	IPI00193233
TIM8A_RAT	5.0615	Q9WVA1	IPI00204831
SNN_RAT	5.1904	P61808	IPI00208675
MIRO2_RAT	5.4537	Q7TSA0	IPI00337111
PEBP1_RAT	5.4771	P31044	IPI00230937
GLPK_RAT	5.4915	Q63060	IPI00950299
MFF_RAT	5.5226	Q4KM98	IPI00358063
Q5U345_RAT	5.5782	Q5U345	IPI00480662
SPT19_RAT	5.6849	Q920Q3	IPI00200836
HXK2_RAT	5.7560	P27881	IPI00201057
O54892_RAT	5.7560	O54892	IPI00201057
SHLB1_RAT	5.7882	Q6AYE2	IPI00392306
PI4KB_RAT	5.8126	O08561	IPI00193760
Q4QRB8_RAT	5.8838	Q4QRB8	IPI00949912
A1L1L6_RAT	5.9882	A1L1L6	IPI00557644
ARLY_RAT	5.9993	P20673	IPI00325599
2ABB_RAT	6.0149	P36877	IPI00206749
MAVS_RAT	6.0649	Q66HG9	IPI00364200
GIMA5_RAT	6.1071	Q8K3L6	IPI00202353
MFN1_RAT	6.1182	Q8R4Z9	IPI00201334
HXK1_RAT	6.2994	P05708	IPI00202543
SYJ2B_RAT	6.3616	Q9WVJ4	IPI00205132
SAM50_RAT	6.3649	Q6AXV4	IPI00372941
Q6IRL2_RAT	6.4260	Q6IRL2	IPI00951357

continued on next page

continued from previous page

MFN2_RAT	6.5249	Q8R500	IPI00325525
TM40L_RAT	6.6361	A4F267	IPI00202955
ACSL1_RAT	6.6572	P18163	IPI00188989
NOS1_RAT	6.7061	P29476	IPI00204773
Q9ET45_RAT	6.7227	Q9ET45	IPI00324438
ACSL6_RAT	6.7383	P33124	IPI00324041
FRAP_RAT	6.7439	P42346	IPI00339164
VAMP1_RAT	6.9806	Q63666	IPI00211083
ACSL5_RAT	7.3039	O88813	IPI00213231
NLRX1_RAT	7.5506	Q5FVQ8	IPI00369394
ASSY_RAT	8.0496	P09034	IPI00211127
AOFA_RAT	8.2896	P21396	IPI00202370
GPAT1_RAT	8.4207	P97564	IPI00205564
B2GV33_RAT	8.4296	B2GV33	IPI00955184
AOFB_RAT	8.5752	P19643	IPI00231774
ABCB6_RAT	8.6585	O70595	IPI00199586
ACSL3_RAT	8.6919	Q63151	IPI00205908
NB5R3_RAT	8.7641	P20070	IPI00231662
TOM40_RAT	8.7741	Q75Q40	IPI00421376
VDAC1_RAT	8.8152	Q9Z2L0	IPI00421874
CPT1A_RAT	8.8274	P32198	IPI00213538
FIS1_RAT	8.8830	P84817	IPI00371036
CPT1B_RAT	8.9008	Q63704	IPI00196647
VDAC3_RAT	9.0041	Q9R1Z0	IPI00231067
MOSC2_RAT	9.0297	O88994	IPI00214398
CXA1_RAT	9.0419	P08050	IPI00231746
PGAM5_RAT	9.0419	Q562B5	IPI00392594
TOM20_RAT	9.0486	Q62760	IPI00208207
KMO_RAT	9.0519	O88867	IPI00213422
BAD_RAT	9.1430	O35147	IPI00206258
CISD1_RAT	9.1730	B0K020	IPI00870183
Q4KLN2_RAT	9.2586	Q4KLN2	IPI00766105
TOM34_RAT	9.2886	Q3KRD5	IPI00565421
B5DFG1_RAT	9.3064	B5DFG1	IPI00208560
Q6Q6S2_RAT	9.5231	Q6Q6S2	IPI00231746
B0BN02_RAT	9.6353[b]	B0BN02	IPI00368621
MGST1_RAT	9.7564[b]	P08011	IPI00230889
ADT1_RAT	9.8520[b]	Q05962	IPI00231927
Q99PC8_RAT	10.0364[b]	Q99PC8	IPI00231774

a. p*I* calculated from amino acid compositions

b. These proteins were excluded from the analysis because their p*I*s were too high for compositions to be generated.

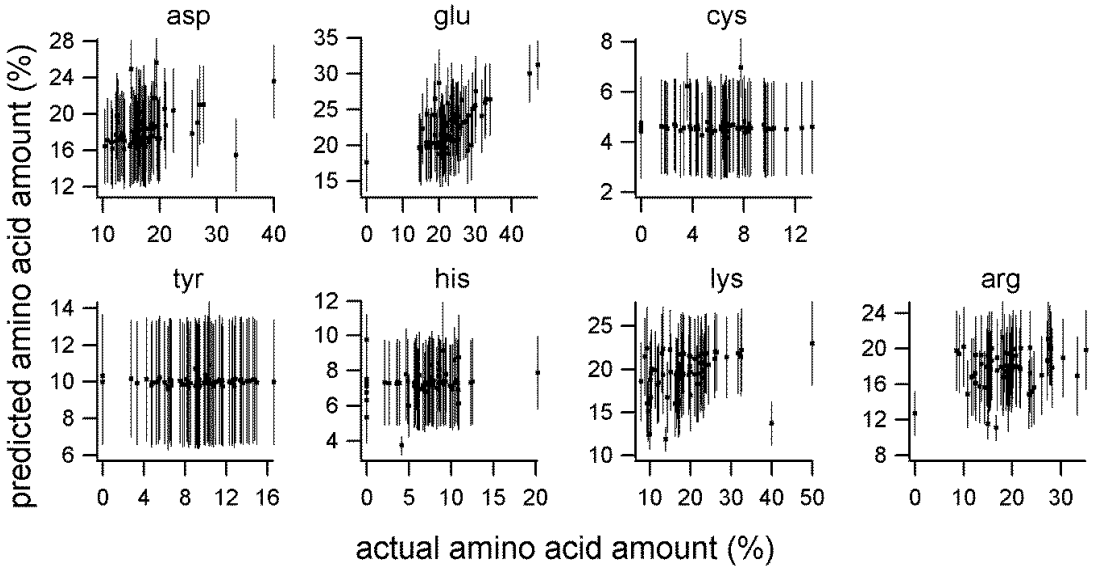

Figure B-1. Comparison of predicted compositions to known compositions of mitochondrial outer membrane proteins. Average percentages of amino acids in predicted compositions with similar p*I* (± 0.02) were plotted against actual percentages of amino acids in known protein sequences of mitochondrial outer membrane proteins. Error bars are plus/minus one standard deviation of the average percent of each amino acid in the predicted compositions. Trends may be difficult to appreciate due to the large standard deviation associated with each determination.

B.4. Comparison of Compositions

Table B-5. Simulated compositions associated with several p*I*s representative of experimental individual mitochondrial p*I*.[a]

p*I*	**6.77**	**6.75**	**6.41**	**4.93**
Ionizable species	Composition (%)[b]			
asp	7.11 ± 1.87	7.08 ± 1.83	7.17 ± 1.88	8.51 ± 2.25
glu	8.24 ± 1.83	8.37 ± 1.89	8.50 ± 1.94	10.41 ± 2.67
cys	2.24 ± 0.65	2.26 ± 0.66	2.25 ± 0.65	2.25 ± 0.66
tyr	4.80 ± 1.39	4.84 ± 1.37	4.88 ± 1.35	4.78 ± 1.37
his	3.89 ± 1.08	3.81 ± 1.07	3.83 ± 1.08	3.84 ± 1.08
lys	11.84 ± 1.91	11.95 ± 1.89	11.73 ± 1.99	10.22 ± 2.34
arg	11.11 ± 1.81	11.10 ± 1.91	10.91 ± 2.01	9.64 ± 2.27
PC	23.78 ± 2.45	23.63 ± 2.47	23.64 ± 2.41	23.48 ± 2.60
PE	18.92 ± 2.00	18.87 ± 2.11	19.00 ± 2.09	18.78 ± 2.19
PI	3.83 ± 0.50	3.85 ± 0.51	3.84 ± 0.49	3.85 ± 0.52
PS	0.39 ± 0.06	0.39 ± 0.06	0.39 ± 0.06	0.39 ± 0.06
CL	3.85 ± 0.48	3.86 ± 0.50	3.85 ± 0.50	3.85 ± 0.52
Total	**100%**	**100%**	**100%**	**100%**
N[c]	6017	6248	7808	19362

a. Each column represents all compositions within 0.01 pH units of the p*I*.
b. For a given p*I* the data is shown as the average ± one standard deviation of the amount of each species in compositions that were included in the calculation.
c. N = number of compositions included in the calculation

Table B-6. Difference from p*I* 6.77 composition.[a]

p*I*	6.75	6.41	4.93
Ionizable species	Difference (%)		
asp	-0.03	0.06	1.40
glu	0.13	0.26	2.18
cys	0.02	0.01	0.01
tyr	0.04	0.07	-0.02
his	-0.08	-0.06	-0.05
lys	0.11	-0.11	-1.62
arg	-0.01	-0.19	-1.46
PC	-0.16	-0.15	-0.31
PE	-0.05	0.09	-0.13
PI	0.02	0.01	0.01
PS	-0.001	0.0002	-0.004
CL	0.01	0.01	0.01

a. Calculated as the amount of each ionizable species from the p*I* 6.77 composition minus the amount from the compositions denoted in each column.

Table B-7. Compositions representing changes in total protein and Fis1.[a]

p*I*	6.77	6.30[a]	6.73[b]
Ionizable species	Composition (%)		
asp	7.11	6.73	7.09
glu	8.24	7.80	8.23
cys	2.24	2.12	2.24
tyr	4.80	4.54	4.79
his	3.89	3.68	3.89
lys	11.84	11.21	11.83
arg	11.11	10.52	11.04
PC	23.78	25.01	23.84
PE	18.92	19.90	18.97
PI	3.83	4.03	3.84
PS	0.39	0.41	0.39
CL	3.85	4.05	3.86
Total	**100%**	**100%**	**100%**

a. Represents a 10% reduction in total protein from the p*I* 6.77 composition.
b. Represents a 50% reduction in Fis1 from the p*I* 6.77 composition, assuming Fis1 represents 1% of the total outer membrane protein.

References for Appendix B

1. The-Uniprot-Consortium, Reorganizing the protein space at the Universal Protein Resource (UniProt). *Nucleic Acids Research* **2012,** *40* (D1), D71-D75.
2. Hovius, R.; Lambrechts, H.; Nicolay, K.; Dekruijff, B., Improved methods to isolate and subfractionate rat-liver mitochondria. Lipid composition of the inner and outer membrane. *Biochim Biophys Acta* **1990,** *1021* (2), 217-226.
3. deKroon, A.; Dolis, D.; Mayer, A.; Lill, R.; deKruijff, B., Phospholipid composition of highly purified mitochondrial outer membranes of rat liver and Neurospora crassa. Is cardiolipin present in the mitochondrial outer membrane? *Biochimica Et Biophysica Acta-Biomembranes* **1997,** *1325* (1), 108-116.
4. Hovius, R.; Thijssen, J.; Vanderlinden, P.; Nicolay, K.; Dekruijff, B., Phospholipid asymmetry of the outer membrane of rat liver mitochondria: Evidence for the presence of cardiolipin on the outside of the outer membrane. *Febs Lett* **1993,** *330* (1), 71-76.
5. Liu, J. H.; Dai, Q.; Chen, J.; Durrant, D.; Freeman, A.; Liu, T.; Grossman, D.; Lee, R. M., Phospholipid scramblase 3 controls mitochondrial structure, function, and apoptotic response. *Mol Cancer Res* **2003,** *1* (12), 892-902.
6. Gebert, N.; Joshi, A. S.; Kutik, S.; Becker, T.; McKenzie, M.; Guan, X. L.; Mooga, V. P.; Stroud, D. A.; Kulkarni, G.; Wenk, M. R.; Rehling, P.; Meisinger, C.; Ryan, M. T.; Wiedemann, N.; Greenberg, M. L.; Pfanner, N., Mitochondrial cardiolipin involved in outer-membrane protein biogenesis: implications for Barth syndrome. *Curr Biol* **2009,** *19* (24), 2133-2139.
7. Smith, A. C.; Robinson, A. J., Mitominer, an integrated database for the storage and analysis of mitochondrial proteomics data. *Mol. Cell. Proteomics* **2009,** *8* (6), 1324-1337.

Appendix C

Supporting Information for Chapter 5

C.1. Photobleaching SH buffer

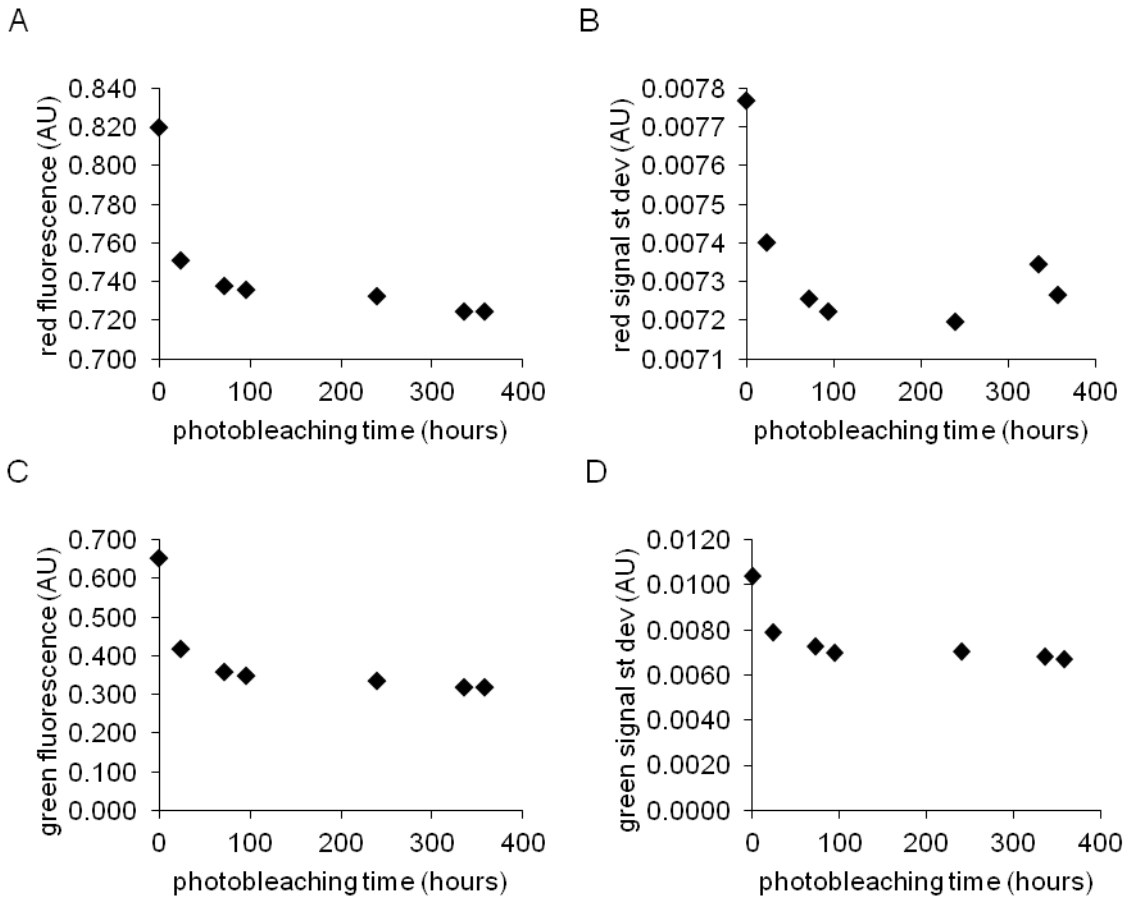

Figure C-1. Photobleaching SH buffer with 2.5 mM succinate. A device containing 120 blue LEDs (467 nm, 4.2×10^5 mcd intensity) was used to reduce the fluorescence background in the SH buffer containing 2.5 mM succinate. Samples were taken at different time points. Samples of buffer were flowed through the sheath flow cuvette, and the fluorescence and standard deviation of the signal was measured. The photobleaching device reduced the red fluorescence (A), red standard deviation (B), green fluorescence (C), and green standard deviation (D). Decreases were observed for the time period measured, although the largest difference is seen after a 24 hour treatment.

C.2. Unmodified Images

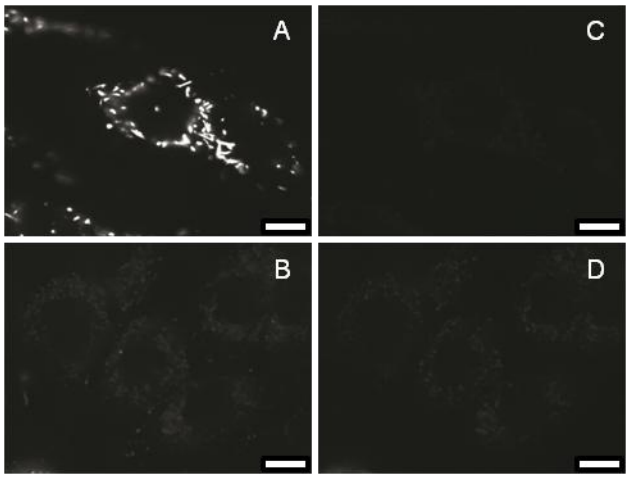

Figure C-2. Unmodified confocal fluorescence microscopy images of polarized (A and B) and depolarized (C and D) L6 rat myoblast cells labeled with 500 nM JC-1 for 30 minutes. Scale bars are 10 µm. Red channel (A and C): 2.0 s exposure time, gain of 100, λ_{ex} = 545 ± 10 nm, λ_{em} = 597.5 ± 27.5 nm, 565 nm dichroic, Olympus M-RFPHQ filter cube; green channel (B and D): 10.0 s exposure time, gain of 100, λ_{ex} = 470 ± 10 nm, λ_{em} = 517.5 ± 22.5 nm, 485 nm dichroic, Olympus U-MGFPHQ filter cube.

C.3. JC-1 Labeling Strategy for Isolated Mitochondria

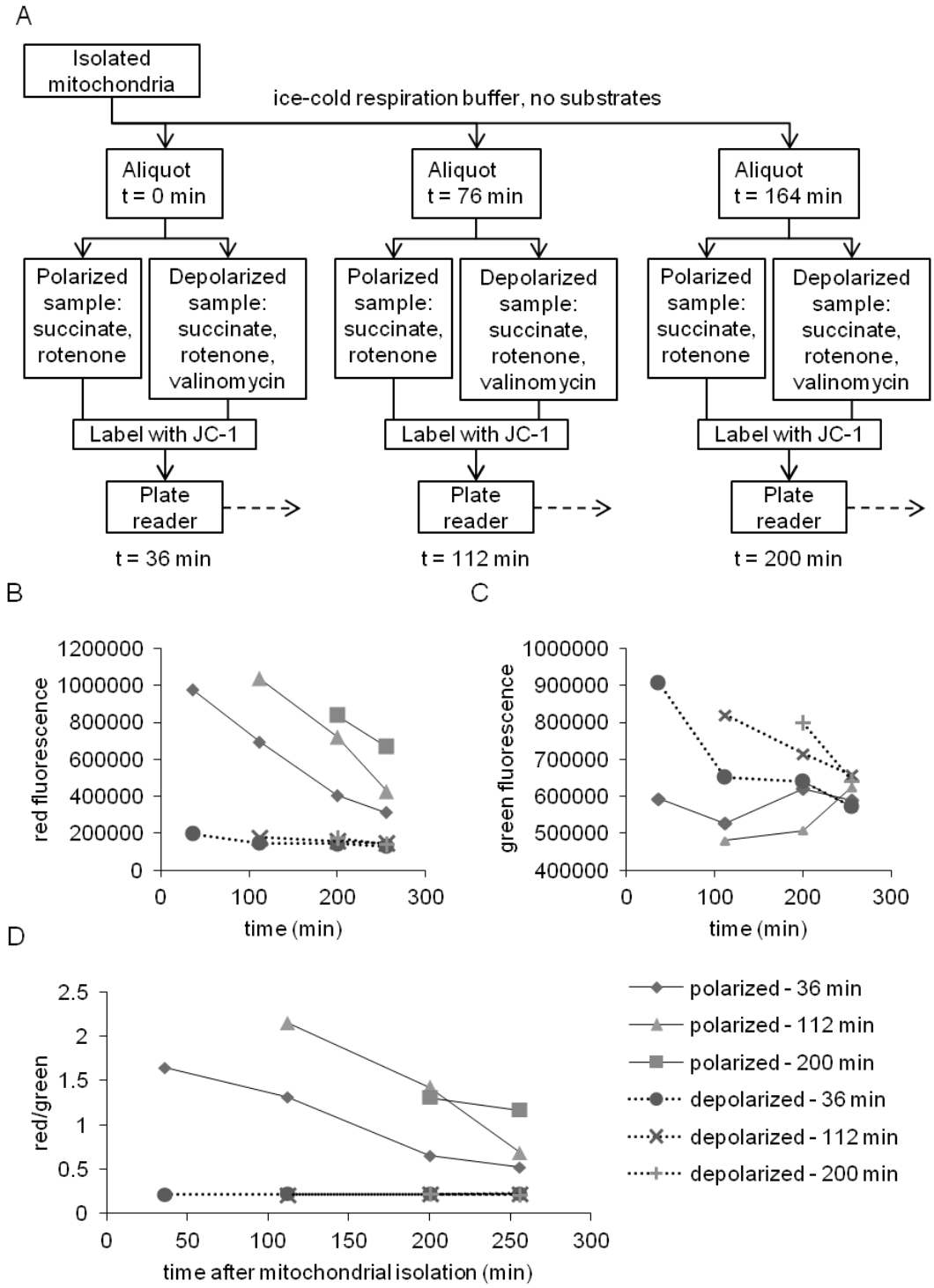

Figure C-3 (continued from previous page). JC-1 labeling strategy for isolated mitochondria. A) Mitochondria from C2C12 cells were isolated and kept on ice in buffer R with no succinate/rotenone or valinomycin. At different time points, aliquots were taken and succinate/rotenone was added (valinomycin was added to depolarized controls). Aliquots were labeled with JC-1 then added to a 96-well plate. Time points shown on the plot represent the time elapsed after mitochondrial isolation before the data was collected. Red (B) and green (C) fluorescence was measured in a plate reader. Red fluorescence and red/green ratio (D) decreases over time for polarized mitochondria. Additionally, aliquots labeled later in the experiment show higher red/green ratios than aliquots labeled earlier at the same point in time (e.g., the polarized sample labeled and measured at 112 minutes has higher red/green ratio than the polarized sample labeled and measured at 36 min, the polarized sample labeled and measured 200 min after isolation shows the highest red/green ratio at the final measurement, 256 min). Each data point is corrected for photobleaching caused by exposure to the excitation light in the plate reader according to the formula below, where photobleaching ($\Delta fluor_{photobleaching}$) was determined by reading the plate two additional times at the end of the experiment (data not shown). Plate reader settings as described in Figure 5-1, JC-1 labeling as described in Chapter 5, section 5.2.5.

$$fluor_{corrected} = n_{reads}(\Delta fluor_{photobleaching}) + fluor_{uncorrected}$$

C.4. Bulk Fluorescence from Isolated Mitochondria

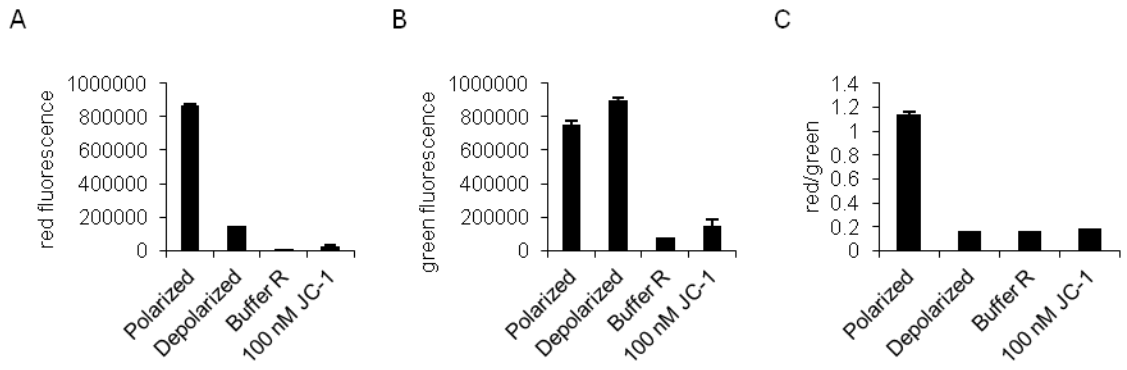

Figure C-4. Bulk fluorescence from isolated mitochondria. Buffer R and 100 nM JC-1 in buffer R are included as controls. A) Red fluorescence (λ_{ex} = 530 ± 12.5 nm, λ_{em} = 590 ± 17.5 nm). B) Green fluorescence (λ_{ex} = 485 ± 10 nm, λ_{em} = 528 ± 10 nm). C) Red/green ratio. Mitochondrial samples have higher red and green fluorescence compared to controls, showing an uptake of JC-1 into mitochondria. Polarized mitochondria have higher red fluorescence than depolarized mitochondria, showing JC-1 aggregate formation from the higher concentration. Error bars represent the standard deviation of measurements from three different wells containing the same sample.

C.5. CE-LIF Detector Alignment

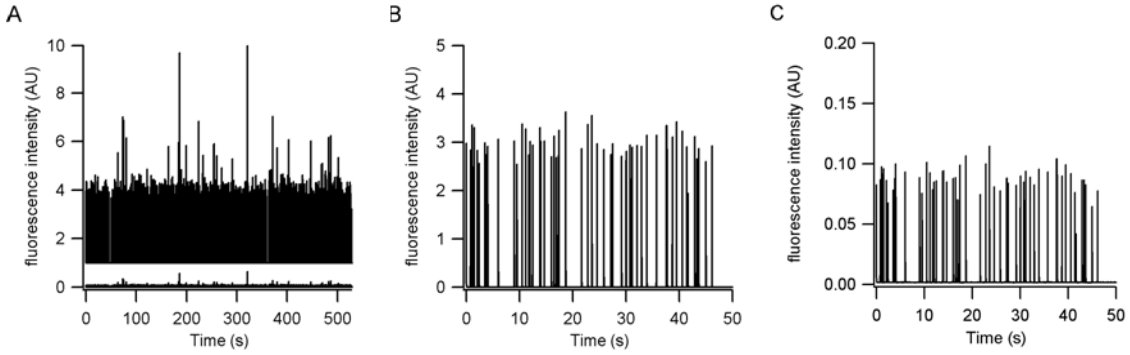

Figure C-5. Alignment of capillary using Alignflow flow cytometry beads. A) All data. Red channel is top, y offset = 1. n = 719 coincident events. Fluorescence intensity was much higher in the red channel than in the green channel (green channel is pictured but difficult to see on the same scale as red channel). B) Detail from 0 to 50 s, red channel. Y-axis shown with different scale than in A. Average event fluorescence intensity %RSD = 18%. C) Detail from 0 to 50 s, green channel. Y-axis shown with different scale than in A. Average event fluorescence intensity %RSD = 35%. Average event red/green %RSD = 14%. See section 5.2.9 in Chapter 5 for CE-LIF conditions.

C.6. False Positives

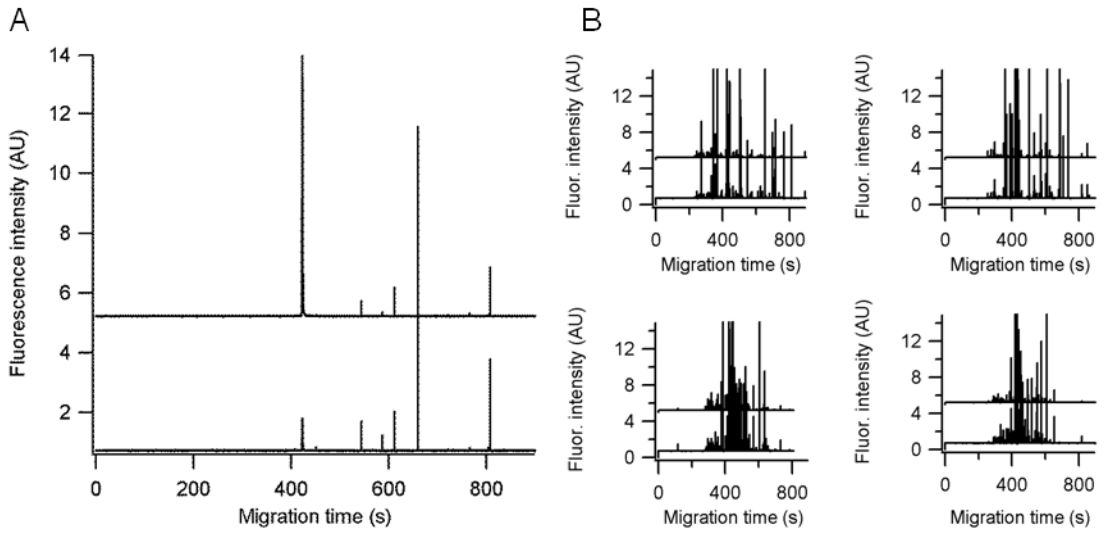

Figure C-6 Control for false positives in CE-LIF. A) Blank injection of 200 nM JC-1 with 5×10^{-10} M fluorescein (peak at 423 s). The concentration of JC-1 was chosen to match the concentration that is present in the mitochondrial samples after dilution with buffer SH for injection. After peak picks and coincidence analysis, 6 events were detected in this run. B) In four runs containing liver mitochondria (two polarized and two depolarized samples), there were 701 coincident events, for an average of 175 events per run. Since the CE-LIF run of the blank injection contained 6 events, this results in a false positive rate of 3.4%. All plots: green channel y-offset = 5. CE-LIF conditions as in Figure 5-2.

C.7. Peak Overlap

Table C-1. Peak overlap results for a CE-LIF experiment of mitochondria from cultured cells. For all runs below (except for two), the number of events in the most crowded bin is smaller than m at both $\beta_t = 0.85$ and $\beta_t = 0.90$, indicating that peak overlap is not a problem in these runs. For the two runs in which n is larger than m, this is only true for $\beta_t = 0.90$, and n exceeds m by only 3 and 5 events in each case. Results from other mitochondrial CE-LIF experiments are not shown, but peak overlap was determined not to be a problem in these experiments (i.e. the detected number of events in each run from these experiments is smaller than the detected number of events in the runs below).

CE-LIF run	1	2	3	4	5	6
p_{tot} (total events)	385	287	278	318	287	301
N (number of bins)	10	9	9	10	9	9
σ (event st dev, s)	0.009	0.009	0.009	0.009	0.009	0.009
X (bin width, s)	23.9	19.4	20.8	23.6	24.1	21.6
$s = \log(\sigma / X)_t$	-3.42	-3.33	-3.36	-3.41	-3.42	-3.37
n (events in most crowded bin)	90	61	76	91	83	74
$\beta_t = 0.85$						
m (threshold number of events)	105	92	96	104	105	99
is overlap a problem at $\beta_t = 0.85$?	No.	No.	No.	No.	No.	No.
$\beta_t = 0.90$						
m (threshold number of events)	87	77	80	86	88	82
is overlap a problem at $\beta_t = 0.90$?	Yes.	No.	No.	Yes.	No.	No.

C.8. Reproducibility of CE-LIF Runs

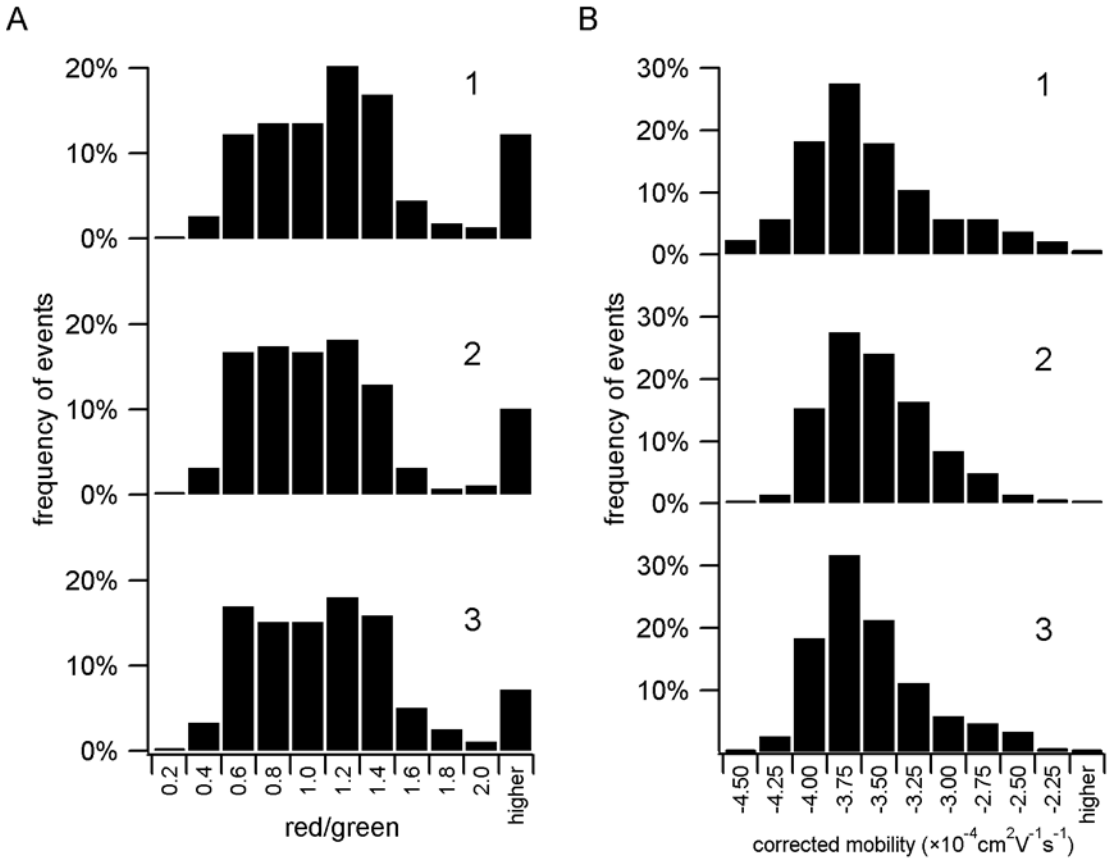

Figure C-7. Distributions of red/green ratios (A) and corrected electrophoretic mobility (B) from individual runs of polarized mitochondria isolated from C2C12 cells, n = 385, 287, and 278 detected events for runs 1, 2, and 3, respectively. See Figure 5-3 in the main text for combined distributions and Q-Q plots. CE-LIF conditions as described in Figure 5-2.

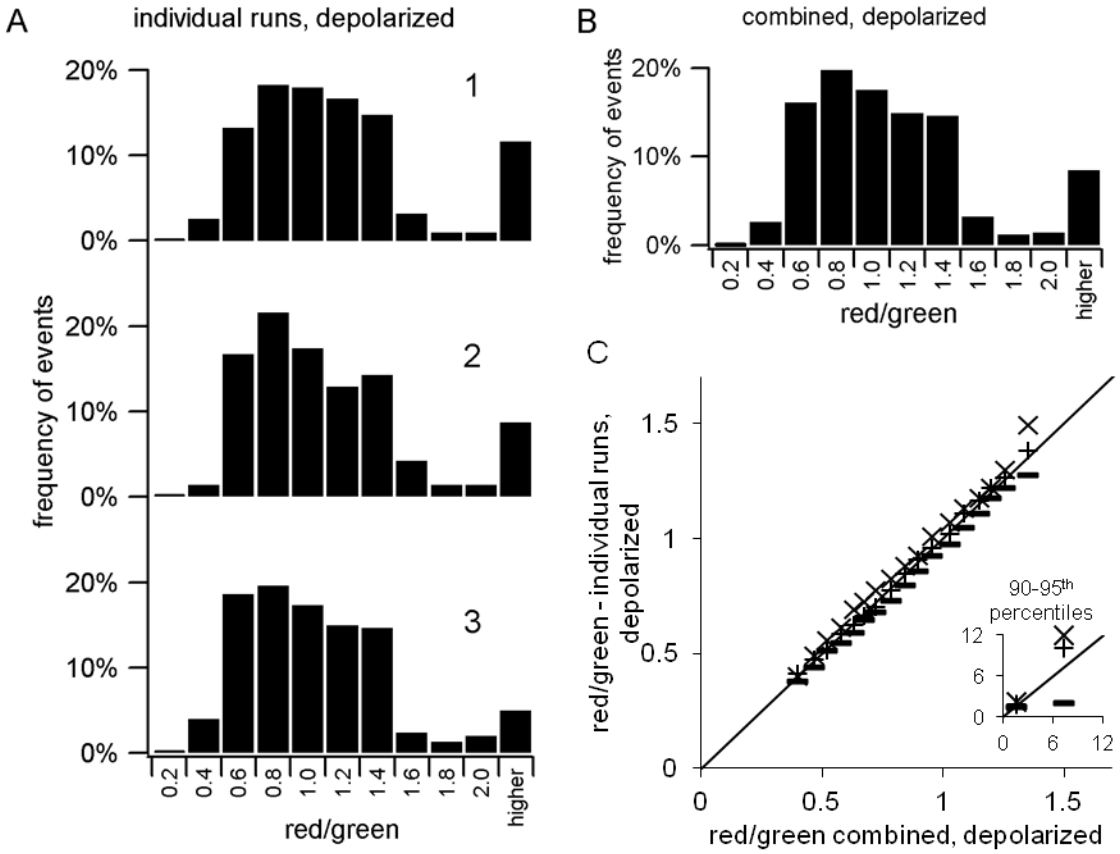

Figure C-8. Reproducibility of red/green ratios in multiple CE-LIF runs of depolarized mitochondria isolated from C2C12 cells. A) Distributions of red/green ratios in three replicate runs of depolarized mitochondria. n = 318, 287, and 301 detected events for runs 1, 2, and 3, respectively. B) Distribution of red/green ratios from the combined runs. C) Q-Q plot of individual runs vs. combined data. This plot is a qualitative indication that the distributions of red/green ratios are reproducible (i.e. data points closely follow the $y = x$ line shown on the plot). There is much more run-to-run variation in the 90-95th percentiles (inset in Q-Q plot in C, normalized ss_{res} = 509%, 291%, and 605% for runs 1, 2, and 3, respectively), but the 5-85th percentiles are reproducible (normalized ss_{res} = 23%, 6%, and 20% for runs 1, 2, and 3, respectively). CE-LIF conditions as described in Figure 5-2.

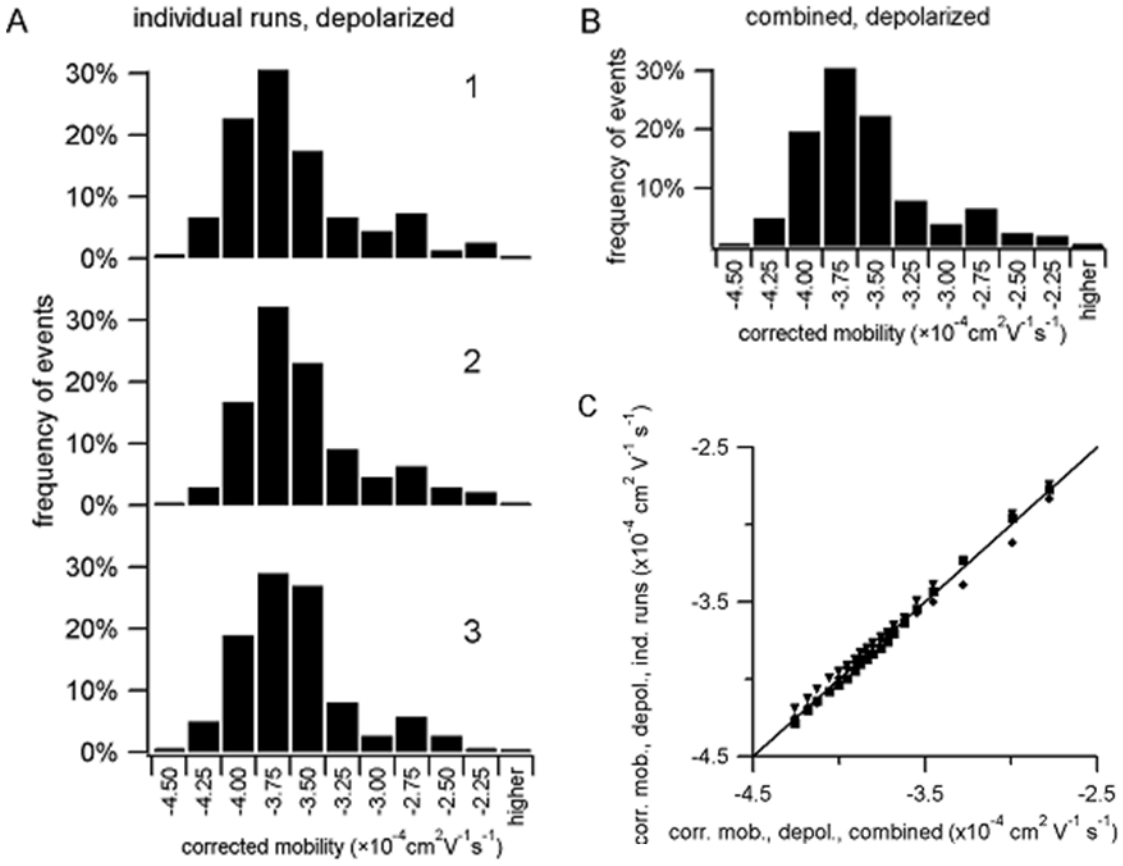

Figure C-9. Reproducibility of corrected electrophoretic mobility distributions in multiple CE-LIF runs of depolarized mitochondria isolated from C2C12 cells. A) Distributions of corrected mobility in three replicate runs of depolarized mitochondria. n = 318, 287, and 301 detected events for runs 1, 2, and 3, respectively. B) Distribution of corrected mobility from the combined runs. C) Q-Q plot of individual runs vs. combined data. This plot is a qualitative indication that the distributions of corrected mobility are reproducible (i.e. data points closely follow the $y = x$ line shown on the plot, normalized ss_{res} = 4%, 5%, and 5% for runs 1, 2, and 3, respectively). CE-LIF conditions as described in Figure 5-2.

C.9. Definition and Reproducibility of ROIs

Table C-2: Fits to red vs. green data using different models. Reduced chi-square (red. χ^2), sum of squares of residuals (ss_{res}), and adjusted coefficient of variance (adj. R^2) are shown to evaluate goodness of fit. Uncertainty values shown for each coefficient are standard error of the mean.

Fit		A	B	C	red. χ^2	ss_{res}	adj. R^2
linear $y = A + Bx$	cells	0.01 ± 0.02	1.31 ± 0.04		0.52	970	0.37
	muscle	0.08 ± 0.01	1.08 ± 0.01		0.15	149	0.89
	liver	0.03 ± 0.02	1.03 ± 0.01		0.22	154	0.89
polynomial $y = A + Bx + Cx^2$	cells	0.09 ± 0.02	0.90 ± 0.07	0.16 ± 0.02	0.51	948	0.38
	muscle	0.04 ± 0.01	1.28 ± 0.03	-0.03 ± 0.01	0.15	142	0.90
	liver	-0.05 ± 0.02	1.25 ± 0.03	-0.04 ± 0.01	0.21	144	0.90
exponential $y = A + Be^{Cx}$	cells	-4.8 ± 1.0	4.9 ± 1.0	0.20 ± 0.03	0.51	949	0.38
	muscle[a]	-9.9 ± 1.7	10.0 ± 1.6	0.08 ± 0.01	0.18	177	0.88
	liver	16 ± 2	-16 ± 2	-0.08 ± 0.01	0.21	145	0.90
power $y = x^A$	cells	1.27 ± 0.02			0.53	988	0.36
	muscle	1.04 ± 0.01			0.17	164	0.89
	liver	1.01 ± 0.01			0.23	157	0.89
logarithm $y = A - B\ln(x + C)$	cells[b]	-1000 ± 5000	-200 ± 900	100 ± 700	0.52	971	0.37
	muscle	-40 ± 10	-17 ± 3	13 ± 2	0.15	143	0.90
	liver	-32 ± 9	-14 ± 2	11 ± 2	0.21	145	0.90
sigmoidal $y = \frac{A}{1 + e^{-B(x-C)}}$	cells	7.0 ± 0.4	1.47 ± 0.06	2.27 ± 0.09	0.53	976	0.36
	muscle	6.38 ± 0.09	1.27 ± 0.03	2.52 ± 0.05	0.18	175	0.88
	liver	6.3 ± 0.1	1.07 ± 0.03	2.81 ± 0.06	0.26	177	0.87

a. To produce a fit which resulted in error smaller than the coefficients, lower and upper bounds of -10 and 10 were used for coefficients A and B.
b. Could not produce a fit in which error was smaller than the coefficients.

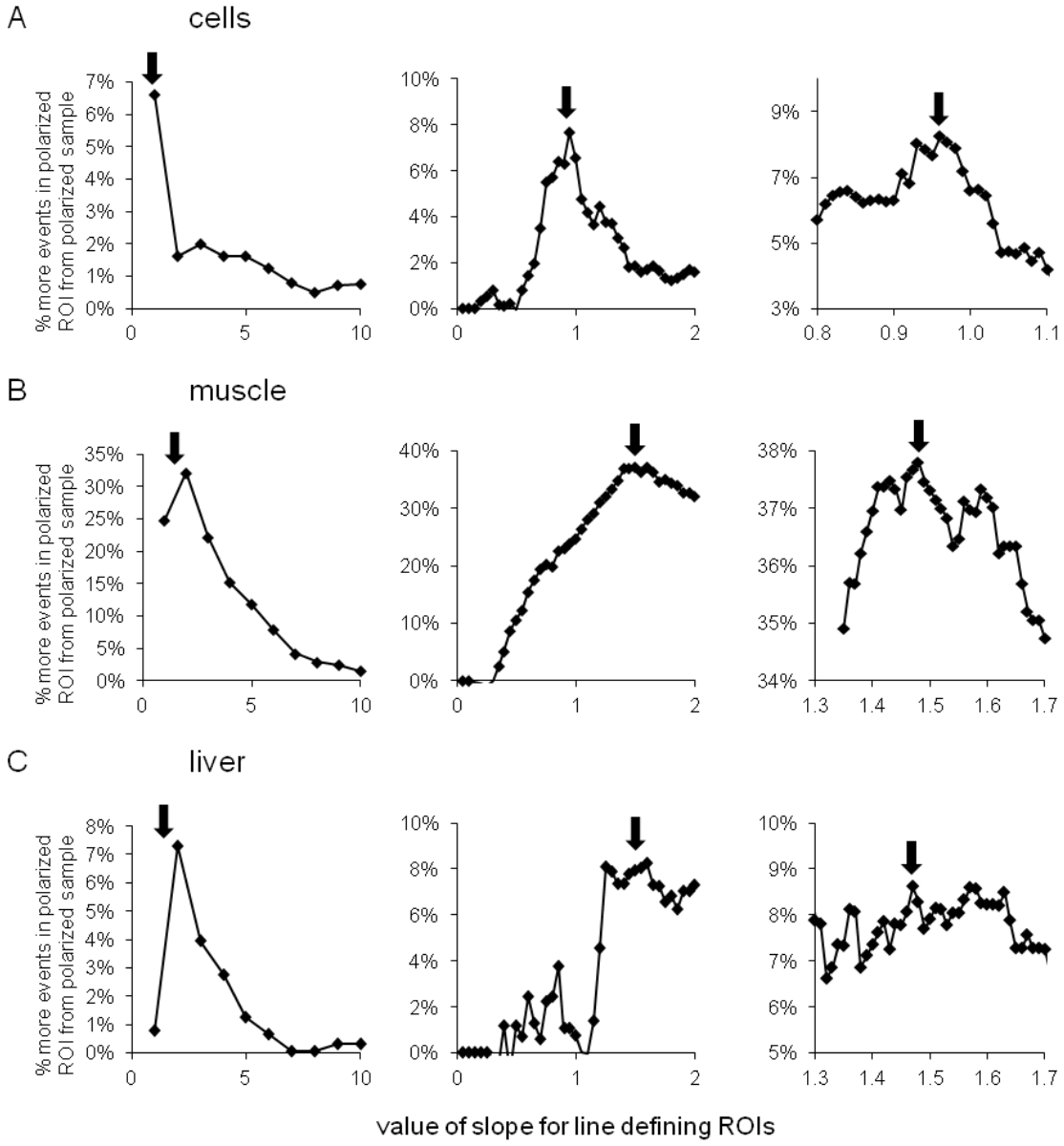

Figure C-10. Optimization of ROIs. The slope of a line defining the ROIs was varied and the difference in the number of events in the polarized ROI between the polarized and depolarized samples was maximized. A) Cells; optimal slope was 0.96 for 8.26% more events in the polarized ROI from the polarized sample than from the depolarized sample. B) Muscle; optimal slope was 1.48 for 37.80% more events in the polarized ROI from the polarized sample than from the depolarized sample. C) Liver; optimal slope was 1.47 for 8.80% more events in the polarized ROI from the polarized sample than from the depolarized sample. Slope used to define ROIs in both muscle and liver samples was 1.475. CE-LIF conditions as described in Figure 5-2.

Table C-3: Number of events in all runs and ROIs of each sample type. The percent difference in the number of events between ROIs from polarized and depolarized samples (i.e. percent in polarized ROI from polarized sample minus percent in polarized ROI from depolarized sample) was maximized to define the ROIs.

Sample	n	n, pol. ROI	%, pol. ROI	n, depol. ROI	%, depol. ROI	% difference in n between ROIs from pol. and depol. samples
cells, pol.	950	501	53%	449	47%	8.26%
cells, depol.	906	403	44%	503	56%	
muscle, pol.	622	306	49%	316	51%	37.52%
muscle, depol.	351	41	12%	310	88%	
liver, pol.	334	61	18%	273	82%	8.29%
liver, depol.	361	36	10%	325	90%	

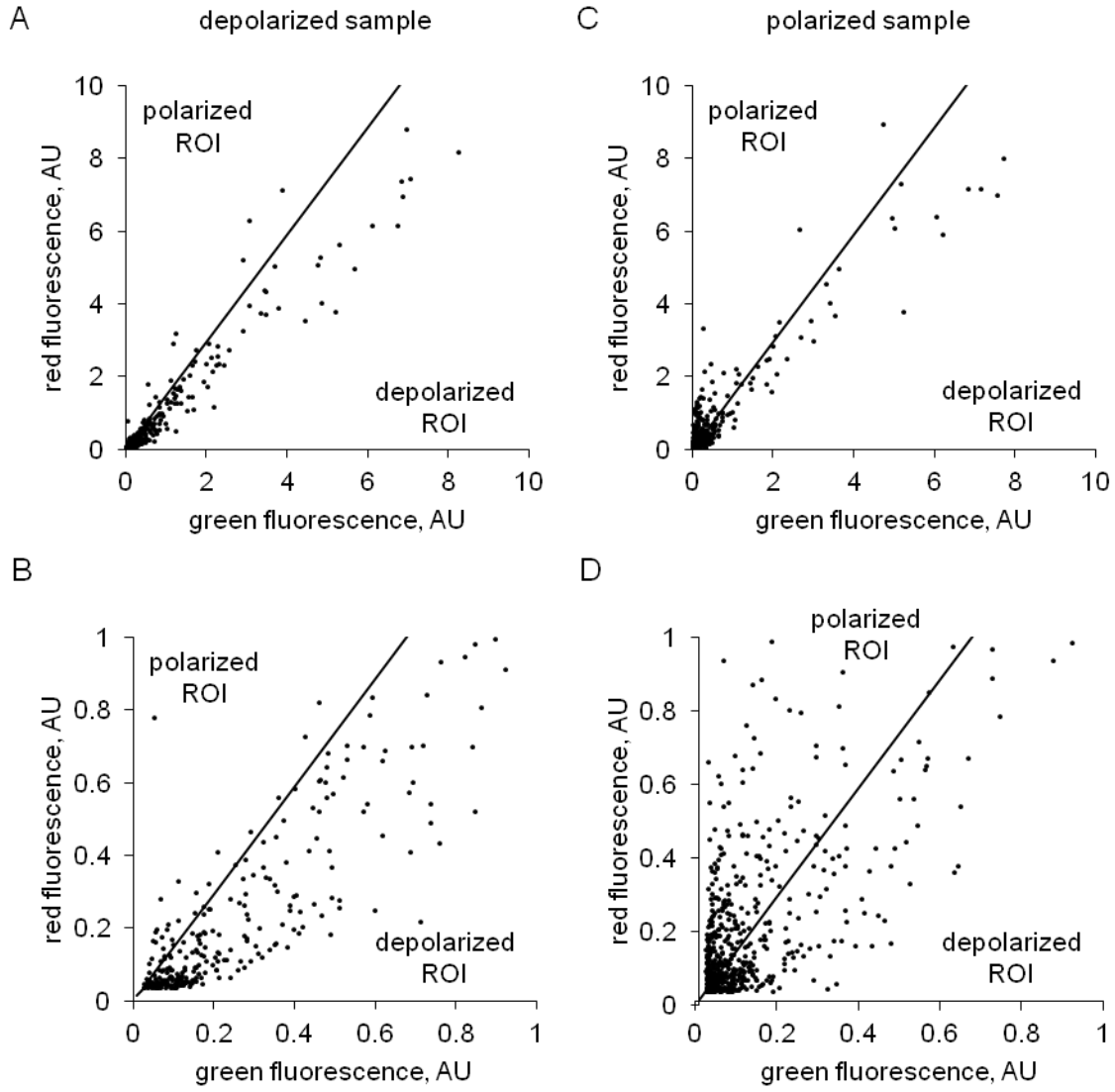

Figure C-11. Definition of ROIs. A) Mitochondrial events from depolarized muscle sample with ROIs shown. B) Detail of A. C) Mitochondrial events from polarized sample with ROIs shown. D) Detail of C. Data shown with logarithmic scale in Figure 5-4. CE-LIF conditions as described in Figure 5-2.

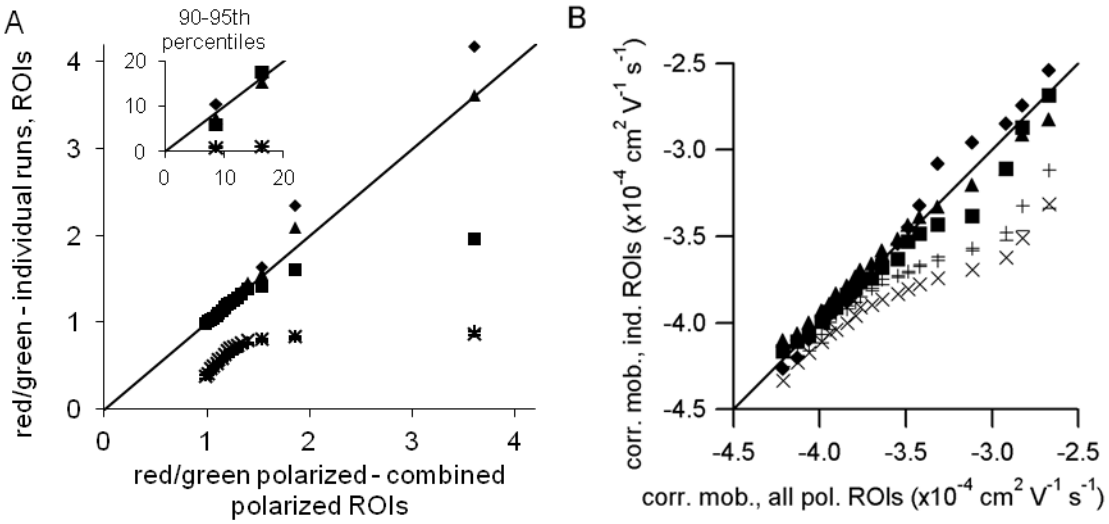

Figure C-12. Reproducibility in ROIs of multiple CE-LIF runs using mitochondria isolated from C2C12 cells. Shaded shapes (■,▲,♦) denote polarized runs and ×,–,+ denote depolarized runs. A) Red/green ratio distributions of polarized ROIs from individual runs of polarized samples and depolarized ROIs from individual runs of depolarized samples vs. combined data from polarized ROIs of polarized samples. Distributions of red/green ratios from depolarized ROIs from individual runs (data points close to x-axis) appear reproducible (overlapping data points indicate minimal scatter among three individual runs each of mitochondria in ROIs from polarized and depolarized samples). B) Corrected mobility distributions of polarized ROIs from individual runs of polarized samples and depolarized ROIs from individual runs of depolarized samples vs. combined data from polarized ROIs of polarized samples. The *y* = *x* line is shown on each plot for comparison purposes. See Table C-4 for normalized ss_{res} for each run. CE-LIF conditions as described in Figure 5-2.

C.10. Quantitative Representation of Q-Q Plots

Table C-4: Sum of squares of residuals (ss_{res}) and normalized ss_{res} from all Q-Q plots in Chapter 5 and Appendix C. The normalized ss_{res} is the square root of the ss_{res} divided by the median of the data from the *x*-axis, reported as a percentage:

$$\text{normalized } ss_{res} = \sqrt{ss_{res}}/median \times 100\%$$

Figure	Sample	Data	Comparison	Quantiles	ss_{res}	Norm. ss_{res}
5-3 B	cells	red/green	run 1 vs combined runs, pol.	all	12.2	353%
				5-85th	0.1	26%
				90-95th	12.1	352%
5-3 B	cells	red/green	run 2 vs combined runs, pol.	all	4.8	221%
				5-85th	0.03	18%
				90-95th	4.8	221%
5-3 B	cells	red/green	run 3 vs combined runs, pol.	all	13.5	371%
				5-85th	0.02	13%
				90-95th	13.4	370%
5-3 D	cells	mobility	run 1 vs combined runs, pol.	all	7.28×10^{-10}	7%
			run 2 vs combined runs, pol.	all	7.65×10^{-10}	7%
			run 3 vs combined runs, pol.	all	3.50×10^{-10}	5%
C-8 C	cells	red/green	run 1 vs combined runs, depol.	all	21.0	510%
				5-85th	0.04	23%
				90-95th	21.0	509%
C-8 C	cells	red/green	run 2 vs combined runs, depol.	all	6.9	291%
				5-85th	0.003	6%
				90-95th	6.8	291%
C-8 C	cells	red/green	run 3 vs combined runs, depol.	all	29.7	606%
				5-85th	0.03	20%
				90-95th	29.6	605%
C-9 C	cells	mobility	run 1 vs combined runs, depol.	all	2.16×10^{-10}	4%
			run 2 vs combined runs, depol.	all	3.33×10^{-10}	5%
			run 3 vs combined runs, depol.	all	4.29×10^{-10}	5%
5-6 C	cells	red/green	depol. vs pol.	all	4.3	210%
				5-85th	0.1	24%
				90-95th	4.3	208%
5-6 D	cells	red/green	depol. ROI vs pol. ROI	all	314.2	1444%
				5-85th	13.9	304%
				90-95th	300.2	1412%

continued on next page

continued from previous page

5-7 C	cells	mobility	depol. vs pol.	all	5.30×10^{-10}	6%
5-7 D	cells	mobility	depol. ROI vs pol. ROI	all	1.83×10^{-8}	37%
C-12 A	cells	red/green	pol. ROI from pol. run 1 vs combined pol. ROIs	all	3.7	156%
			pol. ROI from pol. run 2 vs combined pol. ROIs	all	3.3	148%
			pol. ROI from pol. run 3 vs combined pol. ROIs	all	12.4	287%
C-12 A	cells	red/green	depol. ROI from depol. run 1 vs combined pol. ROIs	all	314.3	1444%
			depol. ROI from depol. run 2 vs combined pol. ROIs	all	313.6	1443%
			depol. ROI from depol. run 3 vs combined pol. ROIs	all	314.7	1446%
C-12 B	cells	mobility	pol. ROI from pol. run 1 vs combined pol. ROIs	all	1.29×10^{-9}	10%
			pol. ROI from pol. run 2 vs combined pol. ROIs	all	1.29×10^{-9}	10%
			pol. ROI from pol. run 3 vs combined pol. ROIs	all	1.50×10^{-9}	10%
C-12 B	cells	mobility	depol. ROI from depol. run 1 vs combined pol. ROIs	all	2.48×10^{-8}	43%
			depol. ROI from depol. run 2 vs combined pol. ROIs	all	1.30×10^{-8}	31%
			depol. ROI from depol. run 3 vs combined pol. ROIs	all	1.80×10^{-8}	36%
5-8 C	muscle	red/green	depol. vs pol.	all	58.4	529%
			depol. ROI vs pol. ROI	all	203.5	501%
5-8 C	liver	red/green	depol. vs pol.	all	1.7	139%
			depol. ROI vs pol. ROI	all	70.1	447%
5-8 D	muscle	mobility	depol. vs pol.	all	1.07×10^{-8}	34%
			depol. ROI vs pol. ROI	all	2.14×10^{-8}	49%
5-8 D	liver	mobility	depol. vs pol.	all	1.50×10^{-8}	37%
			depol. ROI vs pol. ROI	all	1.78×10^{-8}	47%